μSR STUDIES OF THE METALLIC ALKALI FULLERIDES

By

W. Andrew MacFarlane

B. Sc. University of Victoria, 1990

M. Sc. University of British Columbia, 1992

A THESIS SUBMITTED IN PARTIAL FULFILLMENT OF

THE REQUIREMENTS FOR THE DEGREE OF

DOCTOR OF PHILOSOPHY

in

THE FACULTY OF GRADUATE STUDIES

DEPARTMENT OF PHYSICS AND ASTRONOMY

We accept this thesis as conforming

to the required standard

THE UNIVERSITY OF BRITISH COLUMBIA

November 1997

In presenting this thesis in partial fulfilment of the requirements for an advanced degree at the University of British Columbia, I agree that the Library shall make it freely available for reference and study. I further agree that permission for extensive copying of this thesis for scholarly purposes may be granted by the head of my department or by his or her representatives. It is understood that copying or publication of this thesis for financial gain shall not be allowed without my written permission.

Department of Physics and Astronomy

The University of British Columbia

6224 Agricultural Road

Vancouver, Canada

V6T 1W5

Date: Nov. 25 '97

Abstract

Results of muon spin rotation ($\mu S \mathcal{R}$) in the metallic intercalated C_{60} compounds ($A_n C_{60}$, where A_n are n alkali metal atoms) are presented. Except for the case of $K_1 C_{60}$, the metallic state of these systems is unstable at low temperature (to a superconducting transition in $A_3 C_{60}$ and a magnetic metal insulator transition in $A_1 C_{60}$).

In $A_3 C_{60}$, the properties of the metallic and superconducting states are investigated using i) diamagnetic muons to probe the distribution of internal magnetic field and ii) paramagnetic muonium (Mu) trapped within the C_{60} cage to probe the electronic excitations. Mu is found to exhibit strong T_1 relaxation due to its interaction with the conduction electrons. In the superconducting state this relaxation rate exhibits a small enhancement (Hebel–Slichter coherence peak) which possesses an anomalously strong magnetic field supression. Exponential temperature dependence of the relaxation rate at low reduced temperature is observed, and from this estimates of the superconducting energy gap are obtained. At very low reduced temperature, deviations from this behaviour are found. Estimates of the magnetic penetration depth from broadening of the diamagnetic precession signal in the vortex state are also presented and discussed.

In $A_1 C_{60}$ (A = Rb and Cs), the magnetic state is investigated with zero field $\mu S \mathcal{R}$. Observation of a small rapidly damped oscillation below 2K in $Cs_1 C_{60}$ is the first evidence from $\mu S \mathcal{R}$ of magnetic order in these materials. The relaxation at higher temperature indicates that the internal fields are static and possess a broad distribution, indicating a highly disordered static magnetic structure. From the magnitude of the zero field relaxation rates, estimates of the magnitude of the internal field are made.

Table of Contents

List of Tables

List of Figures

Acknowledgements

First, for their help with shifts and setting up the many experiments described in this thesis, I thank S. Dunsiger, J.E. Sonier, J. Chakhalian, K.H. Chow and J.W. Schneider. I would like to thank J.E. Fischer, T. Yildirim and the rest at the University of Pennsylvania, for supplying the samples on time, for the *onerous* glovebox work of mounting them, and for forgiving certain blunders. I would also like to express my great appreciation to my Research Supervisor, Rob Kiefl. Second, I would like to thank the TRIUMF $\mu S \mathcal{R}$ technicians Mel Good, Curtis Ballard and Keith Hoyle; the staff of the TRIUMF machine shop, particularly N. Mackenzie, M. Pankovic, P. Stewart and R. Roper; the staff of the TRIUMF scintillator shop; the rest of the staff of the TRIUMF $\mu S \mathcal{R}$ facility: S. Kreitzman, B. Hitti and D. Arsenau; and everyone at TRIUMF who contributed to keeping the muons trickling or flooding down the beampipe. For help with design of the cryogenic cells, I would like to thank D. Healey. For contributing the ^{3}He I acknowledge the late J. Pederson.

Last, but definitely not least, I thank my family: Karen, Amara and Luca; my parents: Bill and Lynda; and, for their invaluable childcare contributions, I thank Dewey Callhan, Marilyn Callahan and Anita Loudon.

Chapter 1

Introduction

This thesis presents muon spin rotation ($\mu\mathcal{SR}$) measurements of the low temperature electronic and magnetic properties of the known stoichiometric metallic alkali fullerides. The behaviour exhibited by these systems encompasses a wide variety of phenomena of contemporary interest in condensed matter physics. For example, the alkali fulleride superconductors are currently the highest temperature *isotropic* superconductors known. The only class of superconductor with higher critical temperatures (T_c) is the cuprates. Some alkali fulleride metals exhibit reversible solid–state polymerization. The polymeric phase may be a quasi 1–dimensional metal, which in some cases undergoes a low temperature magnetic metal–insulator transition. The specific materials studied are the superconducting alkali fulleride salts of the form A_3C_{60}, with A = Rb, K and $A_3 = Na_2Cs$ and the polymeric phases of the salts of the form A_1C_{60}, where A = K, Rb, Cs. The $\mu\mathcal{SR}$ technique, which is closely related to the widely known methods of nuclear magnetic resonance (NMR) and electron paramagnetic resonance (EPR or ESR), involves the use of the unstable positive muon as a sensitive local probe of magnetic and electronic structure.

Because of the great diversity of topics covered here, considerable reliance on major review articles is made, and a complete exposition of each topic has not been attempted.

Following an introduction to the field of fullerenes and the specific topic of the metallic alkali fullerides, the $\mu\mathcal{SR}$ technique is reviewed briefly in Chapter 2, and some specific details of the experiments are given. In Chapter 3, the theory of longitudinal field spin

relaxation of muonium via the mechanism of spin–exchange with conduction electrons is discussed, and the theory of the temperature dependence of this relaxation in super-conductors is reviewed. Chapter 4 includes the results (and discussion thereof) of $\mu\mathcal{SR}$ experiments on the alkali fulleride superconductors. Chapter 5 is a brief summary of the theory of spin relaxation in zero applied field, an unfamiliar situation for most magnetic resonance techniques. Chapter 6 includes the results (and discussion thereof) of $\mu\mathcal{SR}$ experiments on the A_1C_{60} alkali fullerides, and the conclusions are presented in Chapter 7.

1.1 Buckminsterfullerene!

In the seminal 1985 work [1], Kroto *et al.* correctly guessed that a particularly stable molecular cluster of carbon with a molecular weight of 60 carbon atomic masses took the form of a truncated icosahedron (Fig. 1.1). This insight, together with the explosion of research confirming the form of the molecule and exploring its properties in a wide variety of contexts, culminated in the award of the 1996 Nobel Prize for Chemistry to Curl, Kroto and Smalley (e.g. see [2]). The study of C_{60} in the solid–state, or indeed any study requiring macroscopic quantities of the material, had to wait, however, until 1990 when Krätchmer, Huffman and coworkers discovered[3] that C_{60} could be made easily by arc vapourization of carbon electrodes in a low pressure helium environment. From the remnant soot of such a process, C_{60} can be extracted by dissolution in an organic solvent such as toluene or decalin, and purified by liquid chromatography. To get very pure C_{60}, one can sublime previously purified C_{60} in vacuum at high temperatures ($\sim 500°C$).

The intriguing features of the C_{60} molecule which are also at the heart of many of its interesting properties are: its high symmetry[1], the curvature of its carbon surface, its

---

[1]The icosahedral point group I_h has 120 symmetry operations including 12 fivefold axes (through the pentagons), 20 threefold axes (through the hexagons), 30 twofold axes (through the centres of the
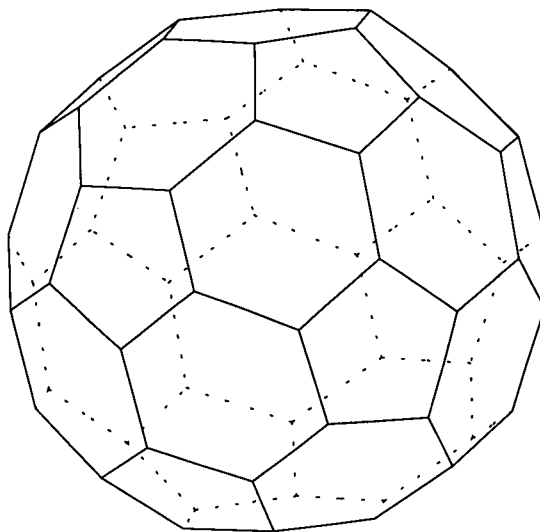
Figure 1.1: A truncated icosahedron: The geometric form has 60 vertices, 12 pentagonal faces, and 20 hexagonal faces. The C_{60} molecule contains a carbon at each vertex, C-C double bonds along the lines separating hexagons, C-C single bonds along the hexagon–pentagon boundaries, and has a diameter of roughly 7.1Å.

relatively large size (moment of inertia $\sim 10^{-43} \mathrm{kgm^2}$), and its hollow core.

There are 4×60 valence electrons in the C_{60} molecule, of which 3×60 are involved in typical covalent bonding between the atoms of the molecule. The remaining 60 electrons are mainly of atomic $2p_z$ character. The curvature of the C_{60} surface causes a hybridization of the atomic $2s$ and $2p$ levels into the π and σ orbitals which have hybridization between planar (sp^2) and tetrahedral (sp^3). The electrons in the σ orbitals participate in the C-C covalent bonding, while the π orbitals protrude from the C_{60} surface with asymmetric lobes outside and inside the carbon framework. This hybridization causes the extremely high electronegativity of C_{60}, i.e. the electron affinity is ~ 2.7 eV (see the review [5]). Another consequence of this hybridization is that the tendency for chemical

hexagon–hexagon boundaries), and inversion (see Chapter 4 of [4] for further details).

bonding differs for the inside and outside of the molecule. Like other aromatic hydro-carbons, such as benzene, these π orbitals interact to form highly delocalized molecular orbitals which make up the highest energy manifold of occupied molecular electronic states. The large number of such electrons suggests that the spectrum of these molecular orbitals could be very complex; however, the high degree of symmetry greatly simplifies the situation. The interesting electronic properties of an object are mainly derived from its highest filled and lowest unfilled levels. For a molecule, these are known as the Highest Occupied Molecular Orbital (HOMO) and the Lowest Unoccupied Molecular Orbital (LUMO). Using the appropriate π atomic orbital basis, the spectrum in the HOMO–LUMO region is well described by the Hückel theory of molecular orbitals, which is essentially a tight–binding model for the π electrons. From this theory, the HOMO is fivefold degenerate ($\times 2$ for the electron spin), the LUMO is threefold degenerate, and the HOMO–LUMO energy difference is on the order of 1 eV. The symmetries of the HOMO and LUMO may also be found in this theory. The HOMO has h_u symmetry while the LUMO has t_{1u} symmetry (which has 5 nodal lines on the molecule surface). For more details, see [4, 5, 6].

High symmetry also simplifies the molecular vibrational spectrum. Free C_{60} has $3 \times 60 - 6 = 174$ degrees of freedom[2], but there are only 46 distinct vibrational modes (10 Raman active, 4 IR active).

For the negatively charged C_{60}, with a partially filled LUMO, the situation above is complicated by the possibility of a Jahn–Teller distortion. In such a situation, the degeneracy of the t_{1u} level is lifted by a static distortion of the molecule, which amounts to a lowering of the symmetry from pure I_h. Such a distortion is driven by the gain in electronic energy which may outweigh the elastic energy cost of the distortion. For more

---

[2]There are 3×60 degrees of freedom for the atoms of the molecule, from which we subtract 6, 3 for overall rigid centre of mass motion and 3 for rigid rotations. In the solid, these 6 degrees of freedom correspond to the intermolecular vibrational modes and the rotational vibrational modes – see §1.2.

details, see §VI.B of the review [7] and references therein.

The hollow core of C_{60} allows the formation of endohedral fullerene complexes, in which an atom is trapped on the inside of the C_{60} cage. Such complexes are conventionally denoted by the (unsanctioned) notation $X@C_{60}$, where the "@" symbol pictographically represents the endohedral nature of the complex. Many different kinds of atoms and clusters have been encapsulated in fullerenes (C_{60} as well as other, less symmetric fullerenes). For example metallic atoms and clusters (Ca, U_2, etc.)[8], noble gas atoms (^{3}He, Ne, etc.)[9], atomic nitrogen[10], and, most importantly for this thesis, atomic muonium (μ^+e^-, essentially an unstable light isotope of hydrogen)[11].

1.2 Molecular Aspects of Solid C_{60} Compounds

Solid C_{60} and its alkali intercalated compounds are *molecular solids*, i.e. their solid state properties bear a strong relationship to the properties of their isolated molecular constituents. Therefore, this section begins with a discussion of some general features of the alkali fullerides which originate in their molecularity: i) their electronic band structures and ii) the structure of their phonon spectra.

The electronic band structure of pure C_{60}, within a few eV of the Fermi Energy (E_F), consists of bands composed of the π molecular orbitals discussed in the previous section. The bands are narrow because the intermolecular overlap is small. Due to the high electron affinity of C_{60}, doping with alkali metals results in essentially complete charge transfer (ionization of the alkali). In the alkali fullerides, bands in which the electron is associated with the alkali ion lie far above E_F. Thus the band structure near E_F is again determined by the C_{60} molecular orbitals. The simplest model of the band structure of the alkali–fullerides is the "rigid band" picture. In this model the intermolecular overlap is assumed to change little upon doping, and the bands are determined by those

of the undoped solid C_{60}. By changing the doping level, one simply alters the filling of the "conduction" band derived from the LUMO of C_{60}, so the filling can be tuned from empty to full as the alkali stoichiometry varies from 0 to 6 per C_{60}. C_{60} and alkali fulleride band structure calculations are reviewed in several places, e.g. [4, 6, 12]. There is also abundant experimental confirmation of the abovementioned general features of the band structures which are reviewed in, e.g. [4, 6, 13].

While this simplistic picture explains the semiconducting nature of pure solid C_{60}, the insulating nature of A_6C_{60}, and the metallic nature of A_3C_{60}, it does not account for the observed non–metallic behaviour of, e.g. K_4C_{60}[14], since 4 electrons per C_{60} should yield a partially filled conduction band and thus metallic behaviour. This brings us to another general aspect of the electronic structure of *metallic* molecular solids, that is, their tendency to undergo metal–insulator transitions which compete with the superconducting transition. An excellent discussion of this topic may be found in the article by Rosseinsky[15] which places the conducting alkali fullerides in the context of other molecular metals. The repulsive Coulomb interaction between electrons competes with their kinetic energy (e.g. [16]). When the kinetic term dominates, the band (or Fermi liquid theory) description of the conduction electrons is valid, but if the Coulomb repulsion is sufficiently strong, the electrons may become localized, and form a Mott–Hubbard insulator. Recent experimental work suggests that this is the case in A_4C_{60} [17]. Generally, the limited kinetic energy of narrow band metals allows any interaction that tends to localize the carriers (e.g. electron–electron, electron–phonon, electron–defect interactions) to have a better chance of doing so.

Another class of metal–insulator transitions is also important in *quasi 1–dimensional* molecular metals. In this case, nesting of the Fermi surface causes a feature (divergence in the ideal 1d case) in the electron susceptibility at a particular wavevector called the nesting wavevector, q_N (discussed below). The effect can occur in any dimension, but

is most pronounced in 1d. Transitions of this class are known as Peierls, Spin–Peierls, Charge Density Wave, and Spin Density Wave (SDW) (see, e.g. [18]). Such transitions are probably not important in the A_4C_{60} situation, but may be relevant to the metal-insulator transitions in Rb_1C_{60} and Cs_1C_{60} (see §1.2.2). For this reason, a brief description of the SDW state is included here.

In contrast to the localization of conduction electrons in a Mott–Hubbard insulator, in the SDW (and similar states), the conduction electrons remain delocalized, but their spectrum becomes gapped at E_F. The phenomenon was first suggested by Overhauser[19] in the context of the free electron gas. The Fermi surface is found to be unstable to perturbations at the wavevector q_N, and the Coulomb interaction (between electrons) has a component at this wavevector, since the (unscreened) q–space form of this interaction is

$$V(\mathbf{q}) = \frac{4\pi e^2}{q^2}.\tag{1.1}$$

Screening, however, eliminates the SDW instability in most metals (e.g., see footnote 27 on p684 of ref.[20]). The nesting wavevector is just a wavevector that maps one part of the Fermi Surface into another. For a spherical (3d free electron) Fermi Surface such a wavevector exists for any state; however, that wavevector only maps a single state into a state on the opposite side of the Fermi Surface. In this situation, the Fermi Surface is not nested. The nesting criterion is just that there exists a wavevector that maps one part of the Fermi Surface into another for *a significant fraction of the surface*. Nesting is said to be "perfect" in 1d, where $\mathbf{q_N} = 2\mathbf{k_F}$ maps the entirety of one branch of the Fermi surface into the other branch. In higher dimensions, nesting is never perfect, and the degree of nesting depends on the geometry of the Fermi Surface. The origin of the SDW instability is the degeneracy of states separated by $\mathbf{q_N}$, i.e. states at the Fermi Surface are all degenerate in energy, thus any perturbation with a Fourier component at $\mathbf{q_N}$ which

mixes these states will lead to an instability (as in degenerate perturbation theory).

SDWs have been found for example in such 3d systems as chromium and its alloys(e.g. [21, 22]) and 1d molecular metals such as the Bechgaard salt $(TMTSF)_2PF_6$, where TMTSF is tetramethyltetraselenafulvalene (e.g. [23]). In a SDW, the density of conduction electrons contains periodic spatial modulations at the nesting wavevector which are *not in phase for the two spin states*, the consequence is a continuously modulated net magnetic moment, which can be quite small, e.g. $10^{-2}\mu_B$. The SDW moment in Cr, though, is quite large ≈ 0.4–$0.6\mu_B$. A SDW is thus related to the antiferromagnetic state of local moments, in the sense that its ordering wavevector is away from the Brillouin zone centre. The SDW wavevector will not, in general, be commensurate with the underlying lattice.

The acoustic properties of solid C_{60} and its alkali salts also exhibit conspicuous molecular features. For pure C_{60}, the basis of the crystal lattice consists of (at least) the 60 carbon atoms, and, thus, there are at least 3×60 modes. For simple solids with a small basis, the phonon modes are conveniently categorized into Longitudinal/Transverse Optical/Acoustic modes. For a molecular solid, the appropriate classification scheme is to connect the *intramolecular* phonon branches to their molecular vibration counterparts. The remaining *intermolecular* modes are of two types: vibrational modes which are of the standard 1 atom per basis varieties (with the C_{60} molecule taking the role of a large atom), and the rotational modes (librons). One can make this molecular picture more concrete by considering the well discussed example of the diatomic linear chain (e.g. Chapter 4 of [24]). If we take the molecular limit, where the bonding is much stronger within a molecule than between molecules, 2 of the optical branches correspond to the intramolecular modes, and the characteristic frequency is near that of the vibrational modes of the free molecule. The 3 longitudinal modes and remaining optical mode correspond to the intermolecular and librational modes, respectively. The libronic mode is optical (e.g. [25])

and its frequency can be found from an effective orientational potential for the molecule in the solid.

1.3 Structure and Properties of Fullerite

In an analogous situation to the solid noble gases, pure solid C_{60} (fullerite) forms an FCC crystal (space group $Fm\bar{3}m$, Fig. 1.2) with relatively small van der Waals cohesive energy. Fullerite does not appear to melt, but rather sublimes at low pressure. In addition, the molecules in fullerite freely rotate for temperatures above a structural phase transition (e.g. [26]) at $T_s \approx 257K$. The low temperature structure is no longer FCC but is simple cubic (space group $Pa\bar{3}$). In this structure, molecules with different orientations make up a larger unit cell than the FCC cell: the corner and face–centre molecules become inequivalent, i.e. there are four C_{60} molecules in the crystal basis. However, the molecules in $Pa\bar{3}$ fullerite are not static. They continue to re–orient, but in a hindered way, jumping between minima of the orientational potential. These re-orientations gradually slow until the structure freezes (at about 90K) into an orientational glass whose *equilibrium* structure is the simple cubic $Pa\bar{3}$ orientationally ordered crystal. Pure fullerite is a semiconductor with a bandgap of about 1.6 eV, a value reasonably close to the HOMO–LUMO gap of the free molecule.

Another interesting feature of fullerite is its instability to polymerization of the C_{60} units. This polymerization can be caused by exposure to visible or UV light[27] or the application of hydrostatic pressure (e.g. [28]). The mechanism of polymerization is thought to be "2+2 cycloaddition", in which two double bonds on adjacent C_{60} molecules break and reform as a pair of intermolecular single bonds, leaving a pair of single bonds in place of the broken double ones (see Fig. 1.3). Polymerized C_{60} has very different properties than fullerite, e.g. it is very insoluble in toluene and has a very different

vibrational spectrum[27].
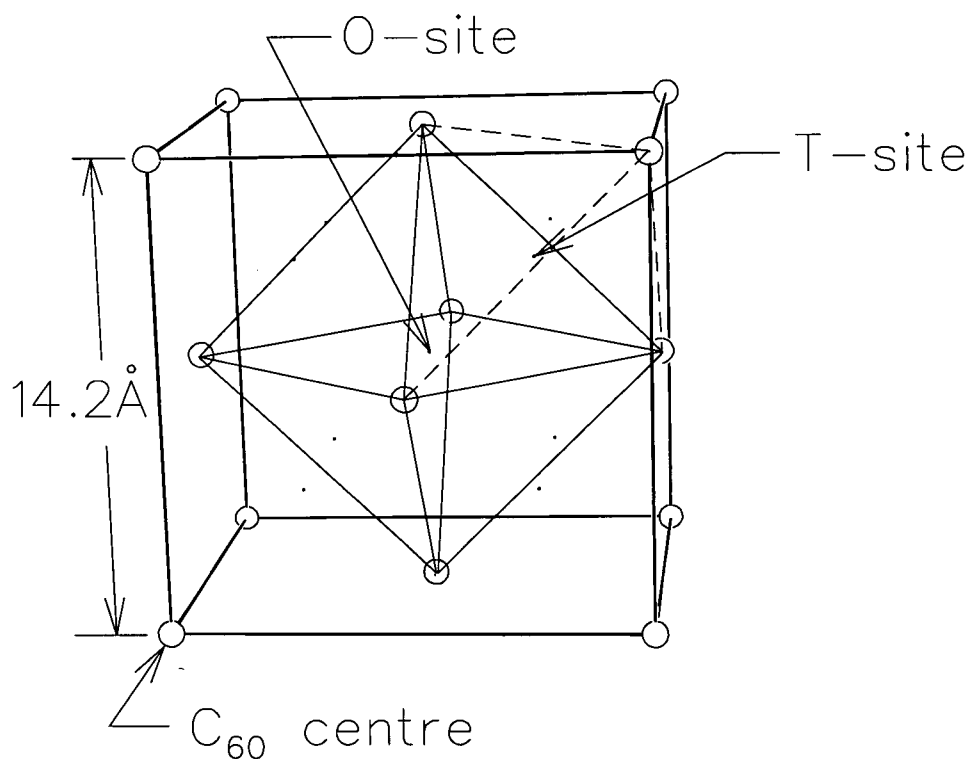
Figure 1.2: The FCC lattice. The lattice constant is approximately that of pure C_{60}, but, for clarity, only the centres of the 7.1Å diameter C_{60} molecules are shown. The small points indicate the high symmetry interstitial sites. An example octahedral (O) site, at the centre of the solid octahedron, is indicated by the arrow. An example tetrahedral (T) site, at the centre of the dashed tetrahedron, is indicated similarly. There are two T-sites and one O–site per C_{60}. These sites are the typical locations of intercalated alkali ions (larger than Na^+) in the alkali fullerides, A_nC_{60}, for $n \leq 3$.
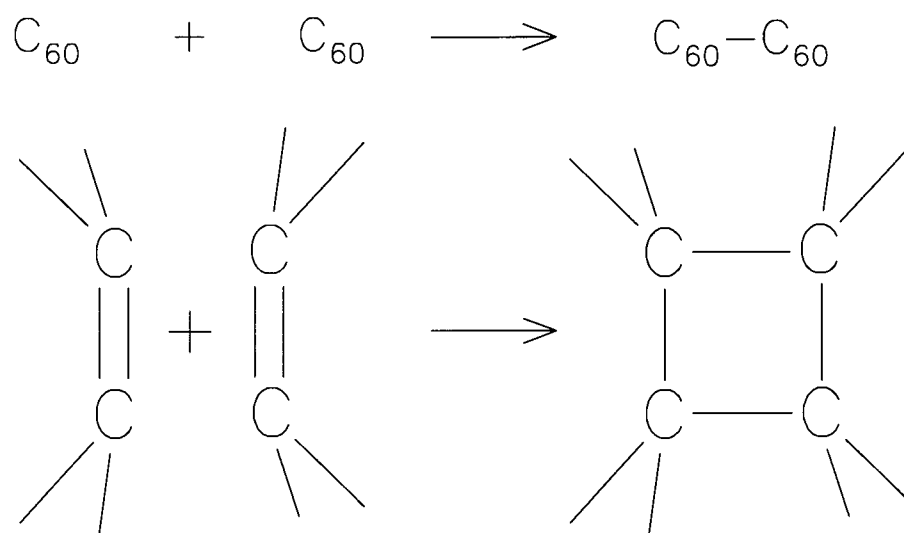
Figure 1.3: 2+2 cycloaddition bonding mechanism between two C_{60} molecules. When the double bonds of two C_{60} molecules are brought together, they break and reform into a pair of intermolecular single bonds. These intermolecular bonds are nearly sp^3, in contrast to the intermediate nature of the hybridization for the C atoms of an isolated molecule.

1.4 Structure and Properties of A_3C_{60}

Very soon after bulk quantities of crystalline C_{60} were available, attempts were made to intercalate them with electron donors (and other atoms) in order to vary their electronic properties. Haddon *et al.* [29] reported the first observation of metallic behaviour in intercalated C_{60}, and shortly afterwards Hebard *et al.* [30] observed superconductivity in K_3C_{60}. The properties of superconducting A_3C_{60} are summarized below without detailed references, but we begin with a list of relevant review articles to which the reader is referred for more detail and specific references. Some general reviews of experimentally determined properties of A_3C_{60} superconductors are those of Ramirez[31], Holczer and Whetten[32], Tanigaki and Zhou[33], and Haddon[5]. There are two recent reviews of the NMR in A_3C_{60}: that of Pennington and Stenger[102] and that of Zimmer[35]. A recent review that focuses on the magnetic properties of the superconducting state of A_3C_{60} is that of Buntar and Weber[36]. Theoretical aspects of these systems have been reviewed by Gelfand[6], Schlüter *et al.* [37], and recently by Gunnarsson[7].

There are two classes of A_3C_{60} superconductors, those containing only alkali ions larger than Na^+ and those containing Na^+. First we discuss the former.

1.4.1 Fm$\bar{3}$m A_3C_{60} Superconductors

When all three alkali ions are at least as large as K^+, the structure of A_3C_{60} is FCC (space group Fm$\bar{3}$m). The alkali ions occupy the O and T interstitial sites (see Fig. 1.2). The details of the site may be more complicated as the observation of three (instead of the expected two) ^{87}Rb NMR lines[38] indicates. The interstitial voids are large enough to accomodate K^+, Rb^+ and Cs^+ ions, but the FCC structure becomes unstable when the alkali filling reaches Cs_3C_{60}, which has the A15 structure and is only a superconductor under pressure (T_c = 40K under 12 kbar[41]). Similarly, a related compound with

electrically neutral spacer molecules in the interstices of the C_{60} lattice, $NH_3K_3C_{60}$, is orthorhombic, and becomes superconducting[39] ($T_c = 28K$) under pressure ($> 10kbar$). These two materials show that cubic symmetry is *not* required for superconductivity in the fullerides. The C_{60} molecules in these materials are orientationally disordered: specifically, they are merohedrally disordered, i.e. there are two distinct orientations of the 3 orthogonal 2–fold axes of the C_{60} along the cubic axes, and these orientations are equally populated. The C_{60} molecules in these phases are not measureably distorted from the isolated C_{60}. The alkali ions act as spacers for the C_{60}, so the average FCC lattice constant increases with the average alkali ionic radius. NMR experiments find that the C_{60} molecules in K_3C_{60} exhibit rotational dynamics down to about 200K (see the review [102] for a discussion).

The superconducting T_c in this class of A_3C_{60} materials is strongly correlated with the FCC lattice parameter. This can be understood qualitatively in the rigid band picture, as a consequence of the correlation of the conduction bandwidth with the intermolecular overlap which depends strongly on the C_{60}–C_{60} separation.. If the lattice is expanded (but not changed in symmetry), the bandwidth decreases, but the total number of states (determined by the number of unit cells in the sample) does not, so the density of states per unit energy at the Fermi Surface increases. Throughout this thesis, the electronic density of states is denoted by $g(E)$ with E measured relative to E_F, so the value at the Fermi surface is $g(0)$. The density of states is connected to the transition temperature, in the BCS theory[42] via

$$T_c = c\Theta_D \exp\left(-1/Vg(0)\right) \qquad (1.2)$$

where Θ_D is the Debye temperature, c is a constant of the order unity and V is some mean electron–phonon interaction energy. In the weak–coupling limit, $\lambda_e = Vg(0) \ll 1$, and using the BCS gap equation, it can be shown that the energy gap is approximately

3.52 times T_c, i.e.

$$2\Delta_0/kT_c \approx 3.52. \tag{1.3}$$

From Eq. (1.2), it can be seen that for a constant V, an increase in $g(0)$, will increase T_c exponentially. It is found that hydrostatic pressure as well a effective chemical "pressure" (tuning of the FCC lattice constant by alkali size) have the same effect on T_c. T_c varies for this class of A_3C_{60} over the range 8K (for K_3C_{60} under 2 GPa) through 19.5K (for ambient pressure K_3C_{60}) to 33K (for ambient pressure $RbCs_2C_{60}$).[3] The FCC lattice constant in the above sequence varies from 13.8Å (K_3C_{60}, 2GPa) to approximately 14.6Å ($RbCs_2C_{60}$, ambient pressure).

These materials are all extreme type–II superconductors with the magnetic penetration depth λ much larger than the superconducting coherence length ξ. In Table 1.1 these parameters as well as the reduced superconducting energy gap from a number of different techniques are tabulated for the best studied representative of the Fm3m class of A_3C_{60} superconductors: K_3C_{60} and Rb_3C_{60}. All experiments indicate that the Ginzburg–Landau paramter $\kappa_0 = \lambda_0/\xi_0$ is on the order of 100. The values of the superconducting energy gap range widely from weak–coupling (Eq. (1.3)) to strong ($2\Delta_0/kT_c > 3.52$, see §1.4.3).

The Fm3m A_3C_{60} materials also possess high low temperature residual resistivity, and therefore small electronic mean free path, l. Although resistivity measurements are complicated by sample granularity, optical techniques, which are not sensitive to this also find an extremely small value for l. The small size of l may be associated with molecular orientational disorder. Ranges for normal state electronic parameters are given in Table 1.2. The other parameters given are the $T \to 0$ value of the resistivity ρ_0, the carrier

---

[3]Due to the large size of the alkali ions in $RbCs_2C_{60}$, This material is found to spontaneously phase separate[40], and the superconducting structure is thus only metastable.

Parameter	K_3C_{60}	Rb_3C_{60}
T_c [K]	18.5–19.7	27.5–30
λ_0 [Å]	2400–8900	2200–8500
ξ_0 [Å]	20–45	20–30
$B_{c1}(0)$ [mT]	1.2–13.2	1.3–16.2
$B_{c2}(0)$ [T]	17–50	40–78
$2\Delta_0/kT_c$	3.0–5.3	3.45–5.3

Table 1.1: Ranges for the reported values of the most important parameters of super-conductivity. The ranges are broad because they include values from a wide variety of techniques on samples from different sources. These ranges are considerably narrower when only a subclass of the most "reliable" techniques on samples of the highest quality are considered. Detailed references can be found in the reviews: [31, 36].

density n, the Fermi Velocity v_F and the parameter r_s which is defined by $n^{-1} = \frac{4\pi}{3}r_s^3$ (see Chapter 1 of [20]).

Parameter	K_3C_{60}	Rb_3C_{60}
n [cm^{-3}]	4.2×10^{21}	4.1×10^{21}
ρ_0 [mΩcm]	0.12–2	0.23–0.8
l [Å]	3–70	3–70
v_F [cms^{-1}]	1.4×10^7	–
E_F [eV]	0.05–2.0	0.05–2.0
$g(0)$ [eV^{-1}]	11–16	19–24
r_s [a_0]	7.2	7.3

Table 1.2: Representative values and Ranges for the parameters of the normal metallic state of K_3C_{60} and Rb_3C_{60}. The electronic density of states is reported per molecule per spin, and a_0 is the Bohr radius.

As mentioned above, the acoustic structure of these materials is characteristic of a molecular solid. The broad frequency spectrum for the various phonon modes is shown in Figure 1.4. By measuring the phonon spectrum (via either Raman or neutron scattering) *as a function of alkali doping*, it is found that the high frequency intermolecular modes

are rather strongly coupled to the conduction electrons, with dimensionless coupling parameter λ_e = 0.2–0.64 (for details, see [31]). In addition it is found via inelastic neutron scattering, that the libron mode hardens as the charge of the C_{60} increases and that the electron–libron coupling is small $\lambda_e < 0.1$.

We now continue with a short description of the other class of A_3C_{60} superconductors, those containing Na^+.
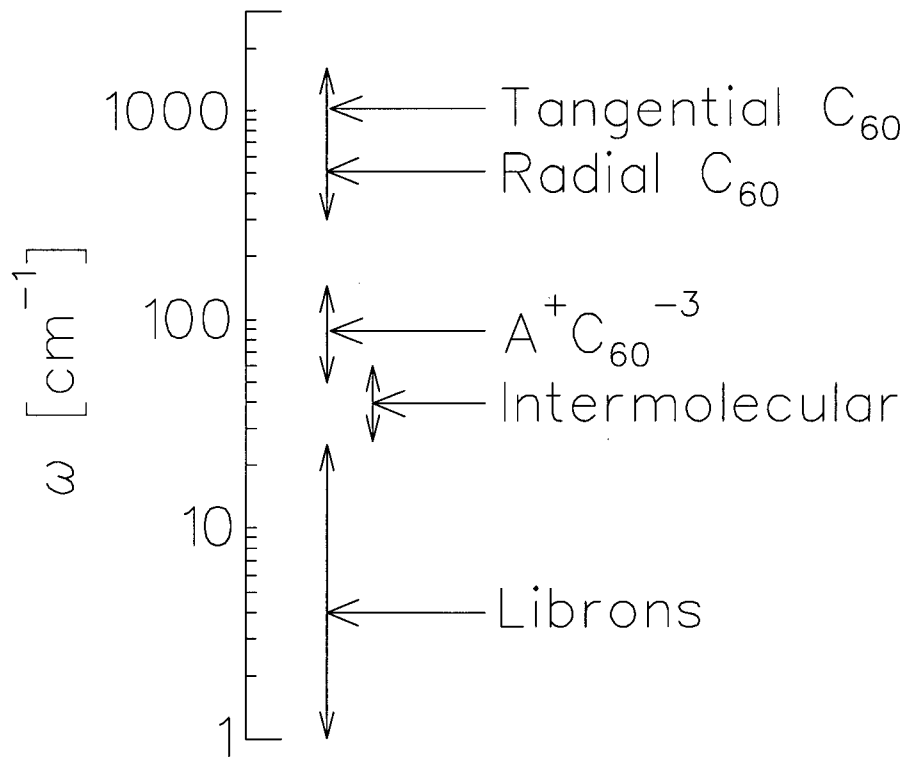
Figure 1.4: The range of phonon frequencies in A_3C_{60} with their characterizations. The high frequency range is characteristic of C_{60} molecular vibrations. The intermolecular modes, including those characteristic of vibrations of the ionic alkali fulleride bond exist at intermediate ranges. At low frequency, there are C_{60} rotational modes, i.e. librons.

1.4.2 Pa$\bar{3}$ A$_3$C$_{60}$ Superconductors

When the smaller Na$^+$ ion is intercalated into C$_{60}$, there are two main structural differences with the previous class of A$_3$C$_{60}$ structures[43]. First, the cubic lattice constants, a, are smaller, e.g. the largest of this class is Na$_2$CsC$_{60}$ with $a \approx 14.1$Å compared to the ambient pressure K$_3$C$_{60}$ $a \approx 14.2$Å. Second, again because of the small Na$^+$ ionic radius, the C$_{60}$ can rotate easily to adopt energetically optimal orientations, and the structure at low temperature is orientationally ordered (space group Pa$\bar{3}$), i.e. the rocksalt structure similar to fullerite. The Pa$\bar{3}$ materials have structural phase transitions, from this oriented phase to a high temperature FCC phase where the molecules are completely orientationally disordered. These first–order structural phase transitions occur close to room temperature[200] ($T_s \approx 300$K for Na$_2$CsC$_{60}$ and Na$_2$RbC$_{60}$). Recently, it has also been found that the C$_{60}^{-3}$ molecules in these structures polymerize (at ambient pressure for Na$_2$RbC$_{60}$ [45] and under modest pressure $P \leq 3$kbar for Na$_2$CsC$_{60}$ [92]). More recent studies of the pressure dependence are reported in [47]. The rocksalt structure below T_s is only metastable, but the polymerization is incomplete probably because it is limited kinetically. In close analogy with the polymeric A$_1$C$_{60}$ structure, polymerization on Pa$\bar{3}$ A$_3$C$_{60}$ involves an orthorhombic distortion of the cubic lattice, and the formation of chains of closely spaced covalently bonded C$_{60}^{-3}$ ions.

The superconducting transition temperatures in the Pa$\bar{3}$ systems are low, the highest known is Na$_2$CsC$_{60}$ with a $T_c = 12$K. T_c is even more strongly dependent on the cubic lattice constant. It was initially thought that this may have been the result of the higher degree of order, but with the new discovery of the polymeric phases has complicated this interpretation. Zhu has suggested that the polymer chains may in fact be the superconducting phase, but recent evidence from the case of Na$_2$RbC$_{60}$ suggests that this is not the case. If the polymeric chains are not superconducting, then the strong correlation

between T_c and lattice constant may be explained by a strong supression of T_c caused by partial polymerization in nominally Pa$\bar{3}$ samples.

In contrast to Rb_3C_{60} and K_3C_{60}, the superconducting properties of the Pa$\bar{3}$ systems have not been well characterized. This may be partially because of the difficulty in making samples with reproducible values of T_c, which could also be a consequence of the metastability of the superconducting Pa$\bar{3}$ structure. The role of orientational disorder has, however, been studied theoretically[6, 48]. The possibility that the electronic properties would be significantly different for the ordered Pa$\bar{3}$ structure (as predicted for instance by Mele and Erwin[48]) was the original motivation for our study of Na_2CsC_{60}. However, the influence of polymerization, discovered after the experiments presented here, has turned out to be more significant, see §4.3.2.

1.4.3 Strong–Coupling Theory of Superconductivity

As a preface to the discussion of the superconducting pairing mechanism in A_3C_{60}, a brief summary of the strong–coupling theory of superconductivity is included here.

The "strength" of the electron–electron attractive coupling is measured by the dimensionless coupling constant, λ_e. In the BCS theory $\lambda_e = Vg(0)$, and the boundary between the "weak" and "strong" coupling regimes is[49] about $\lambda_e = 0.25$ with the weak–coupling limit being $\lambda_e \to 0$ and the infinitely strong-coupling limit being $\lambda_e \to 1$.

The theory of Bardeen, Cooper and Schrieffer treated only the simplest form of attractive interaction between electrons, i.e. the interaction $V(E)$ was simply a constant (independent of energy, direction or temperature) for E within the Debye energy of the Fermi energy and zero outside of this range. A more realistic and general treatment of the electron–phonon interaction, which allows both for structure to the interaction and strong electron–phonon coupling was first accomplished by Eliashberg[50]. For general reviews of this topic the reader is referred to the works of Scalapino[49], McMillan and

Rowell [51], and the more recent review of Carbotte [124].

The general electron–phonon interaction Hamiltonian is

$$H_{ep} = \sum_{\mathbf{kk'}\lambda\sigma} M_{\mathbf{kk'}\lambda}[b_{\mathbf{q}\lambda} + b^{\dagger}_{-\mathbf{q}\lambda}]c^{\dagger}_{\mathbf{k'}\sigma'}c_{\mathbf{k}\sigma}, \tag{1.4}$$

where $b_{\mathbf{q}\lambda}$ is the annihilator for a phonon at wavevector $\mathbf{q}$ with branch index λ, $c_{\mathbf{k}\sigma}$ is the annihilator for an electron at wavevector $\mathbf{k}$ and spin σ, M is the interaction, and $\mathbf{q} = \mathbf{k'} - \mathbf{k}$. The phonon density of states is

$$F(E) = \sum_{\lambda} \int \frac{d^3\mathbf{q}}{(2\pi)^3} \delta(E - E_{\mathbf{q},\lambda}), \tag{1.5}$$

where $E_{\mathbf{q},\lambda}$ is the λ–branch phonon dispersion curve. In the Eliashberg theory, this interaction is included via a Fermi Surface (FS) average coupling–constant phonon density of states product:

$$\alpha^2 F(E) = A_{FS}^{-1} \int_{FS} d^2\mathbf{k} \int_{FS} \frac{d^2\mathbf{k'}}{(2\pi)^3} \sum_{\lambda} \frac{|\tilde{M}_{\mathbf{kk'}\lambda}|^2}{v_F} \delta(E - E_{\mathbf{k}-\mathbf{k'},\lambda}), \tag{1.6}$$

where A_{FS} is the area of the Fermi Surface and $\tilde{M}$ is the "dressed" electron–phonon interaction M which includes the effect of Coulomb renormalization (see p.481 of [49]). The function $\alpha^2 F(E)$ contains all the relevant information about the electron–phonon coupling giving rise to the effective attractive interaction between electrons which produces the superconductivity. However it turns out that in many cases the important information in this distribution is not in its details, but simply in two of its "moments": the mass enhancement parameter λ_m and the logarithmic moment, $E_{\log}$ which are defined by:

$$\lambda_m = 2 \int_0^{\infty} \frac{\alpha^2 F(E)}{E} dE \tag{1.7}$$

$$E_{\log} = \exp\left[\frac{2}{\lambda_m} \int_0^{\infty} \alpha^2 F(E) \frac{\ln(E)}{E} dE\right]. \tag{1.8}$$

The effective electron mass modified by the electron–phonon interaction is just $m^*/m = 1 + \lambda_m$.

The theory of superconductivity based on this general approach to the electron–phonon interaction is summarized in the Eliashberg equations, which are coupled non-linear self–consistent equations which take the place of the BCS gap equation and include the BCS gap equation as a special case. From these equations, McMillan (see e.g. [51] and references therein) developed an equation for T_c analogous to the BCS equation (Eq. (1.2)) which was subsequently improved by others (see [124]). It reads

$$kT_c = c' E_{\log} \exp\left(-\frac{1.04(1+\lambda_m)}{\lambda_m - \mu^*(1+0.62\lambda_m)}\right). \tag{1.9}$$

The as yet undefined parameter μ^* represents the electron–electron Coulomb interaction and is discussed further in §1.4.4. The parameterization of the dimensionless coupling λ_e in terms of V and $g(0)$ has evidently been replaced. In fact, correspondence with the BCS theory gives

$$\lambda_e = \frac{\lambda_m - \mu^*}{1 + \lambda_m}. \tag{1.10}$$

The argument of the exponential function in the McMillan equation (Eq. (1.9)) is not simply $-\lambda_e^{-1}$, as it was in the BCS theory. This is because the form e^{-1/λ_e} is only approximate. From Eq. (1.10), we see that for an infinite electron–phonon mass renormalization ($\lambda_m \to \infty$), the dimensionless coupling parameter $\lambda_e \to 1$, i.e. this is the infinitely strong–coupling limit. A representative range for λ_m in conventional superconductors is 0.4–3.0[124].

For the range of parameters found in real materials, the following approximate form for the important ratio of the energy gap to T_c (analogous to the BCS result Eq. (1.3)) has been found (see [124])

$$\frac{2\Delta_0}{kT_c} \approx 3.53 \left[1 - 12.5 \left(\frac{kT_c}{E_{\log}}\right)^2 \ln\left(2\frac{kT_c}{E_{\log}}\right)\right]. \tag{1.11}$$

For real superconductors this ratio is, for the weak–coupling limit, close to the BCS value of 3.52, and for stronger coupling materials it ranges up to about 5.1. Thus the

broad range of reported values (Table 1.1) encompasses both the weak–coupling and strong–coupling regimes.

1.4.4 Parametrization of the Electron Coulomb Interaction

The contribution of the electron–electron Coulomb repulsion to the overall electron–electron interaction in a metal is not well understood. The topic will not be reviewed in detail here, but a short introduction to the typical parametrization is given below following a mainly qualitative discussion of the interaction.

First, notice that the electron–electron Coulomb interaction (at least for independent electrons) is clearly repulsive, as their charges are of the same sign. This is in contrast to the electron–phonon interaction which can be effectively attractive. The electron–phonon interaction in metals (Eq. (1.4)) is a model for the electrostatic (screening) interaction between the system of ions and conduction electrons. In typical metals, the screening response of the lattice is much slower than the response of the electron system. This is just the Adiabatic Approximation which, according to Migdal's Theorem, applies in the limit where the Debye energy, E_D, is much smaller than the Fermi Energy. Typically this holds because the ion masses are much larger than the electronic mass. The "retarded" response of the lattice causes the electron interaction to acquire energy dependence. In particular, for electrons differing in energy by more than E_D, the interaction is negligible, and for electrons close in energy, the interaction can be strong and can become negative, i.e. attractive.

To make a complete model for the *net* interaction between electrons in a metal, one must also consider the effect of (self)screening of the electrons. The effect of the Coulomb repulsion is to introduce a halo of positive charge around an electron. Screening of this

kind modifies the Coulomb interaction from the unscreened form (Eq. 1.1) to

$$V(\mathbf{q}) = \frac{4\pi e^2}{q^2 \epsilon(\mathbf{q}, \omega)},\qquad(1.12)$$

where ϵ is the effective dynamic dielectric response function of the medium which we consider here to be just the conduction electrons. The effect of screening is always to limit the (infinite) range of the interaction. The co-ordinate space screened interaction will fall off exponentially with a characteristic screening length scale, e.g. the Thomas–Fermi length $r_{TF} = (4\pi e^2 g(0))^{-1}$ which is typically less than 1Å. The screening is complete for length scales large in comparison to r_{TF}, i.e. for wavevectors much smaller than $k_{TF} \sim r_{TF}^{-1}$. The limited range of the screened interaction leads naturally to simplified local models, such as the Hubbard model. In this kind of model the electron–electron repulsion is parametrized by a single number which is essentially the repulsive energy cost of bringing two electrons close together (i.e. onto the same site or separated by a distance less than the screening length). The magnitude of this energy, which is conventionally denoted U, depends on the full screened electron–electron interaction including both the electron–phonon and electron–electron terms. An upper bound for U can be estimated by simply calculating the unscreened Coulomb energy required to bring two electrons to some minimal distance. The effect of screening by the two media (the positive lattice and the negative electrons) is to reduce this energy. An appropriate dimensionless measure of U is

$$\mu = U g(0),\qquad(1.13)$$

where g(0) is the density of states per energy per spin. A simple treatment of screening (e.g. see [53]) leads to a renormalization of this energy to the conventional parameter known as the "Coulomb Pseudopotential", μ^* (e.g. Eq. (1.9)).

$$\mu^* = \frac{\mu}{1 + \mu \ln\left(E_F/E_D\right)}.\qquad(1.14)$$

Thus, in the limit where $E_F \gg E_D$, $\mu^* \approx [\ln(E_F/E_D)]^{-1}$, and thus for all typical metals $\mu^* \approx 0.1$. In the theory leading to this result, the electron–electron repulsion is only added after the electron–phonon interaction. Recently, there has been a theoretical attempt to treat these interactions on a more equal footing[54]. These authors find that at low electron density (such as in molecular metals), there are significant deviations from the McMillan equation (Eq. (1.9)) / $\mu^* \approx 0.1$ result.

1.4.5 Pairing Mechanism in the Fulleride Superconductors

The narrowness of the conduction bands in the A_3C_{60} materials and the large predicted values of the electron–electron Coulomb repulsion prompted exotic "all electronic" theoretical pairing models, e.g. [55]. In this model the electron screening is found under some conditions to reduce the electron–electron Coulomb repulsion to such a degree that it becomes effectively attractive in some energy range. However, nearly all the observations can be understood by a conventional electron–phonon pairing mechanism in which:

- The order parameter is s–wave.

- The attractive interaction leading to pairing is of the standard electron–phonon variety.

- The important phonons mediating the electron pairing are the high frequency intramolecular phonons. The dimensionless coupling to these phonons is $\lambda_e \approx 0.7$.

- The Coulomb Pseudopotential is reasonably small $\mu^* \approx 0.15$. This has been explained in various ways, for example as a result of compensation by a Jahn–Teller energy (particular to the trianionic C_{60}[56]). Another explanation for the small μ^*

uses the renormalization discussed previously, but with a much higher characteristic electron energy (replacing E_F in Eq. (1.14)). This is rationalized by appealing to the contribution of Coulomb scattering into higher bands[37].

The success of this conventional pairing scheme challenges our understanding of superconductivity more generally, because

- The conduction bandwidth is small and the phonon frequencies are high (i.e. the intramolecular modes shown in Fig. 1.4), so the applicability of Migdal's theorem, on which the Eliashberg theory (§1.4.3) rests, is questionable, e.g. see [51]. In particular, the Eliashberg theory is only correct in the limit where the phonon energy scale is much less than E_F.

- The electron–electron Coulomb interaction is expected to be large: U for two electrons on a sphere of radius 3.5Å is estimated to be 3 eV. Screening by molecular polarization may reduce this to about 1 eV, yielding an estimate of the Coulomb parameter $\mu \approx 10$. Because E_F is not much greater than the phonon energies, though, the screening renormalization of μ (Eq. (1.14)), should be ineffective in reducing μ^* to a value $\ll 1$.

- The molecular wavefunctions that make up the conduction band have spatial extent which is roughly an order of magnitude larger than that of typical ("atomic" rather than molecular) metals.

- These systems, at least for the Fm$\bar{3}$m case, are intrinsically disordered (in the molecular orientation).

In light of these considerations, perhaps the important question is why superconductivity in the fullerides can apparently be explained in the conventional picture of electron–phonon mediated pairing.

1.5   Structure and Properties of A_1C_{60}

Crystalline Phases

The A_1C_{60} phase has the single interstitial alkali ion (A = K, Rb or Cs) in the O–sites of the high temperature FCC phase of fullerite[57] (Fig. 1.2). This cubic phase, however, undergoes a structural phase transition to a slightly distorted orthorhombic phase. The critical temperature of this transition is about 350K, but there is a broad range of temperatures over which the two phases co-exist (250K – 350K for Cs and 295K – 350K for Rb[58]). Extensive Reitveld analysis of x–ray diffraction profiles indicates[59] that the orthorhombic phase (o–A_1C_{60}) has chains of C_{60}, that are spaced much more closely than in the corresponding FCC phase. The direction of these chains is along a face diagonal of the FCC structure (e.g. $\langle 1,-1,0 \rangle$ with respect to the FCC lattice). It is now well accepted that in this phase the C_{60} units are polymerized within the chains by the same "2+2 cycloaddition" mechanism suggested for the fullerite polymer (§1.2.1). The model proposed to explain the x–ray diffraction has, along the polymer axis, a short C_{60}–C_{60} spacing of about 9.1Å. It also involves a stretching distortion of the C_{60} molecule along the chain axis, yielding a nearest C–C distance of about 1.4Å which is typical of carbon bond lengths. The distortion of the C_{60} molecule has been corroborated recently by magic angle spinning NMR, which resolves the broadened ^{13}C resonance into several lines corresponding to inequivalent carbon atoms[60]. The array of chains in a plane containing the nearest neighbour chains (e.g. $\langle 1,1,-1 \rangle$) is shown in Figure 1.5. In addition, there is a metastable structural phase that exists if an A_1C_{60} material is quenched rapidly from the FCC phase. This phase involves C_{60} dimers. No experiments on the dimer phase of A_1C_{60} are reported in this thesis, so it will not be discussed further. The interested reader is directed to reference [61].
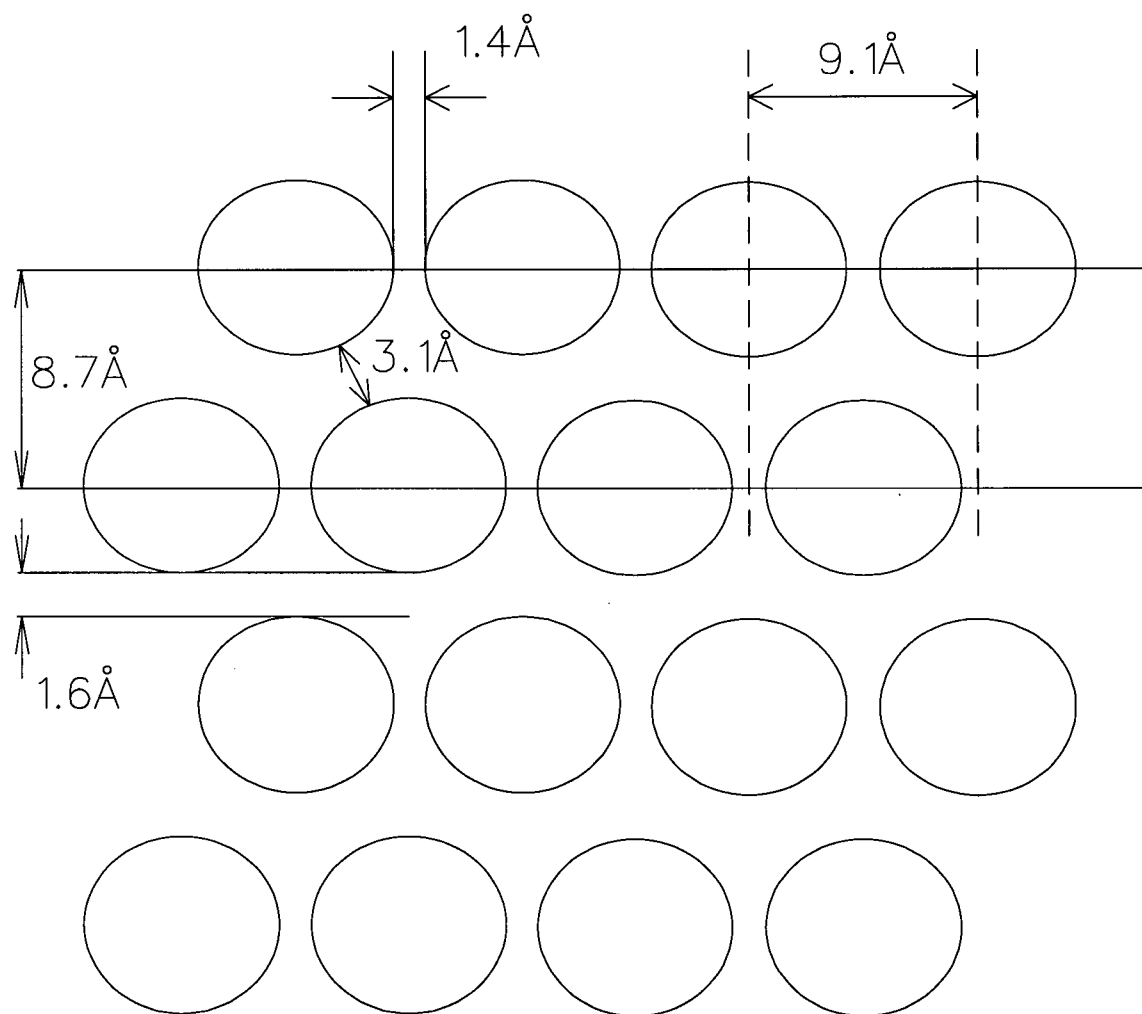
Figure 1.5: The C_{60} chains in o–A_1C_{60} shown in a plane which includes the nearest neighbour chains. The distances are for A = Rb, and come from the results reported in [59].

1.5.1 Properties of Polymeric o-A_1C_{60}

We now consider the o-A_1C_{60} phase in more detail. As would be expected from the simplistic rigid band model, in which the t_{1u} band is 1/6 full, o-A_1C_{60}, as well as the high temperature cubic fcc -A_1C_{60}, are metallic, as shown, for example by optical measurements[62, 63]. However, NMR and ESR experiments indicate that the conduction electrons *may* be behaving in a quasi 1–dimensional fashion, i.e. the NMR T_1 relaxation rate is temperature independent[64] above about 100K [4] and the ESR spin suscpetibility is *large* (6×10^{-4} emu/mole) and temperature independent[66]. At low temperatures, a magnetic metal–insulator transition has been observed[66] as a rapid drop of the ESR spin susceptibility below about 50K (for A = Rb or Cs). Interestingly, this transition does not appear for A = K. It was originally suggested[66] that the magnetic phase is of the SDW type (see discussion above), although no conclusive evidence was provided. We note that high temperature NMR measurements[58] on the cubic phase of A_1C_{60} (for A = Rb and Cs) exhibit a Curie–like temperature dependence in the frequency shift, in contrast to the temperature independent Pauli shift expected for a normal metal. This temperature dependence has been interpreted as an indication that the conduction electrons are close to localization even above the structural transition. It is the structure of the low temperature magnetic phase that will be the main focus of the results on A_1C_{60} presented in this thesis.

Subsequent to the initial ESR measurements, neutron scattering experiments have been mounted by several groups but have shown no magnetic features[67]. The lack of magnetic neutron scattering indicates one or a combination of the following: i) the magnetic structure is highly disordered (such that even short–range magnetic correlations are not apparent in the neutron spectra), ii) the ordered moments are too small to resolve

---

[4]Temperature independent T_1 can arise from 1 dimensional magnetic fluctuations, see [65].

with neutrons (this is apparently the case for the SDW ordering in the TMTSF salts[23]), or iii) the ordering wavevector is in some unexpected direction. Progress in characterizing the nature of the magnetic state was made by NMR[64]. There are several key conclusions in this work:

- The T_1 relaxation rate above the magnetic transition is nearly temperature independent for all 3 nuclei (^{13}C, ^{87}Rb or ^{133}Cs), and the ratio of the values of $T_1 T$ for the ^{13}C and ^{133}Cs in Cs_1 is consistent with the different locations in the unit cell.

- In the magnetic state of $Cs_1 C_{60}$, the ^{13}C line breaks into 2 components, one narrow as in the non–magnetic o–$Cs_1 C_{60}$ phase and one very broad. The ^{133}Cs line, however, broadens as a whole with no remnant narrow line. This indicates that the magnetic state of the sample is *homogeneous*, but for some unexplained reason, there are two kinds of carbon atoms: one which senses only small fields, and one which senses large fields.

- Using knowledge of the size of the isotropic hyperfine couplings, it is concluded that the broadening of the ^{133}Cs line is too large to be explained, unless it is due mainly to dipolar fields of moments which are aligned in a *direction correlated with the applied field*.

- Considering some models of the broadening, they conclude that the magnetic state is a spin–flop[5] antiferromagnet with a relatively large magnetic moment ($0.5\mu_B$) which is ordered in the chains but not between them.

---

[5]A spin–flop transition occurs in an antiferromagnet when the Zeeman interaction of the magnetic moments exceeds the anisotropy energy that selects the antiferromagnetic (easy) axis, stabilizing a different antiferromagnetic phase. In an applied field less than the spin–flop field, the average moment direction in an antiferromagnet is canted continuously by the applied field, but at the spin–flop field, the moment direction changes discontinuously. For more details see [68, 69].

More recently, Antiferromagnetic Resonance (AFMR) has been observed in Rb_1C_{60} and Cs_1C_{60}[70]. From measurement of the field and temperature dependence of this resonance, it is concluded[70] that: The magnetic state is well-ordered and is consistent with a spin–flop antiferromagnetic state (which they conclude is probably a 3d ordering of 1d SDWs). Furthermore, magnetic fluctuations are observed in the broad range 35K – 50K.

At this point we note that there is an analogous transition to the spin–flop of a local moment antiferromagnet for the SDW state. This transition is known as the spin–flip transition and has been observed in Cr, for example[21]. The transition in this case is from a longitudinal to transverse SDW. It differs from the spin–flop transition though in the fact that the phase boundary in the $H–T$ plane intersects the $H = 0$ axis.

Discussion of the several reported $\mu\mathcal{SR}$ measurements on the magnetic A_1C_{60} phase will be deferred to Chapter 6 where they will be included with the discussion of the results presented in this thesis.

1.5.2 Electronic Structure of o–A_1C_{60}

The degree of one dimensionality of the electronic structure of polymeric o–A_1C_{60} is not clear at the present time. As mentioned above the NMR and ESR are suggestive of 1d behaviour, but calculations based on the accurate polymer structure[71] suggest that interchain couplings are probably important. This is because electronic motion along the C_{60} chains is *impeded* by the nearly sp^3 orbitals of the carbon atoms at the C_{60}–C_{60} bonds. Other band structure calculations of polymeric C_{60} chains have also been performed[72]. It is clear that the molecular distortion in the polymeric o–A_1C_{60} makes the rigid band picture based on the I_h symmetry of the undistorted C_{60} highly suspect. The distortion lifts the I_h symmetry, and splits the t_{1u} LUMO. If this splitting is greater

than the bandwidth, it may be that the A_1 conduction band is formed from a non-degenerate molecular level and is hence half–full. NMR measurements on Rb_1C_{60} under pressure support the three dimensional nature of electronic structure[73]. Moreover, the low temperature magnetic phase is found to be eliminated under pressures exceeding about 6kbar.

Potential magnetic structures for o–A_1C_{60} have been considered theoretically[74]. By including a short range repulsive electron–electron interaction together with the band structure of [71], it is found that a complex 3d magnetic state is stable. These authors also note that for certain regions of the antiferromagnetic couplings, the magnetic ordering is geometrically frustrated.

Chapter 2

Description of the Experiments

The measurements described in this thesis were made using standard muon spin rotation/relaxation ($\mu S\mathcal{R}$) techniques with minor modifications. In the first section of this chapter, the general technique will be reviewed briefly, with reference to the many more detailed technical reviews. In the next subsection, the practical problems posed by these air–sensitive powdered materials (i.e. sample mounting, handling and storage) and their resolutions will be discussed. The final section is a brief account of the synthesis of alkali intercalated fullerides.

2.1 $\mu S\mathcal{R}$ Techniques

For detailed accounts of the technique, the reader is referred to the following references: the book of Schenck[75], the review article of Cox[76], and the recent review of Brewer[77]. The recently published book of Schatz and Weidinger[78] also has some elementary discussion of $\mu S\mathcal{R}$. One should be aware that description of $\mu S\mathcal{R}$ in the recent book *Science of Fullerenes and Carbon Nanotubes*[4] is incorrect. Excellent discussions of specific technical aspects of $\mu S\mathcal{R}$ can be found in the following theses: for transverse field, the thesis of Riseman[189]; for general technical details those of Chow[80] and Luke[81]; and for a thorough discussion of the statistical details of $\mu S\mathcal{R}$ and of possible distortions in $\mu S\mathcal{R}$ spectra, that of Garner[82]

31

2.1.1 Properties of μ^+

For later reference, a brief summary of the properties of the muon is included at this point.

The positive muon (μ^+) is a lepton, the heavier analogue of the positron. It is unstable, and decays via the weak interaction with lifetime τ_μ into a positron and two neutrinos:

$$\mu^+ \xrightarrow{\tau_\mu} e^+ + \nu_e + \bar{\nu}_\mu. \tag{2.1}$$

The branching ratios to other decay channels are less than 2%. Some properties of μ^+ are given in Table 2.3.

	μ^+	e^-	p^+	^{13}C
Lifetime	2.19703(4) μs	$> 4.3 \times 10^{23}$y	$> 1.6 \times 10^{25}$y	stable
Type	lepton	lepton	baryon	nucleus
Mass [MeV/c²]	105.65839(4)	0.5109991(2)	938.2723(3)	12100
Mass [m_e]	207	1	1836	23700
Mass [u]	0.113	5.5×10^{-4}	1.007	13.0
Charge [e]	+1	-1	+1	+6
Spin [$\hbar$]	1/2	1/2	1/2	1/2
μ [μ_B]	4.8419710×10^{-3}	1.001165923(8)	1.521×10^{-3}	0.3824×10^{-3}
μ [μ_N]	9.021	1838	2.79284739(6)	0.702199
μ [MeV/T]	28.44×10^{-14}	5.795×10^{-11}	8.804×10^{-14}	2.214×10^{-14}
μ/k [mK/T]	3.3	672	1.0	0.26
$\gamma/2\pi$ [MHz/kG]	13.554	2802	4.25759	1.07054

Table 2.3: Selected properties of μ^+ and other particles which are important in various magnetic resonance techniques.

Because of the parity violation of the weak interaction, the positron emitted in a μ^+ decay is correlated with the direction of the muon spin at the instant it decays. In detail, the average rate (probability per time) that a positron of energy within $d\epsilon$ of ϵ is emitted

within $d\theta$ of θ, the angle with respect to the μ^+ spin at the time of decay, is

$$dW = \tau_\mu^{-1}\left[1 + \frac{2\epsilon - 1}{3 - 2\epsilon}\cos\left(\theta\right)\right]\epsilon^2(3 - 2\epsilon)d\epsilon d\cos\left(\theta\right), \qquad (2.2)$$

where ϵ is the positron energy relative to the maximum positron energy of 52.8 MeV. It is this correlation that allows the direction of the spin to be monitored in a $\mu S R$ experiment by angle–resolved (often crude) observation of their decay positrons. Typically, no energy resolved measurements are done. All decay positrons (down to some low energy threshold) are treated equally in the data acquisition, effectively causing an average over the range of emitted positron energies (ϵ =0–1).

The technique of $\mu S R$ was born with the discovery of the parity violation in muon decay by Garwin, Ledermann, and Weinrich[83]. The discovery of this parity violation has recently been recounted in [84].

2.1.2 Production of Spin Polarized Muons and $\mu S R$

In conventional magnetic resonance experiment spin polarization is achieved by a combination of high field and low temperature, kT can be made on the order of or less than the relevant magnetic level splitting, and thermal equilibrium will ensure some spin–polarization (though the polarization is typically very small $< 10^{-3}$). Other methods for polarizing spins include nuclear reactions, tilted foil methods, and optical excitation. In $\mu S R$, the parity violating decay of the pion is the process by which the muon spin is polarized. The two features of π^+ decay that yield the spin–polarization of the product μ^+ are i) it is 2 body final state ii) it is a weak decay.

$$\pi^+ \xrightarrow{\tau_\pi = 26\text{ns}} \mu^+ + \nu_\mu. \qquad (2.3)$$

The pion is a boson with zero angular momentum; hence the total final angular momentum of the products must also be zero. Because the neutrino is always produced in a

helicity (spin·momentum) state of -1, and, in the rest frame of the pion, the muon and neutrino are emitted "back–to–back", the muon must also be in a -1 helicity eigenstate, i.e. it is spin–polarized.

This scheme is used in practice in the following way:

- A beam of intermediate energy ($\sim$500 MeV) protons is trained on a production target of some light nucleus material such as carbon or beryllium.

- Nuclear reactions occur in the production target which produce positive pions. Some pions remain in the target, and some are emitted with net kinetic energy.

- The pions quickly decay, emitting muons via Eq. (2.3) The muons have a distribution of momenta some with high momentum from high energy pions decaying in flight, and some with low momentum muons that are produced by pions deep within the production target.

- Muons emitted in a particular direction are guided down a beamline to a Wein velocity filter where crossed electric and magnetic fields select a particular momentum. The momentum used corresponds to muons *from pions which decay at rest near the surface of the production target.* These so called "surface muons" have a well-defined kinetic energy of 4.1 MeV. Other muons (and positrons from muons that have already decayed) with different momenta are thus bent out of the beam direction, and play no role in the experiment.

- At low fields, the Wein filter (or "separator") can be used simply as a momentum selector, but at high fields, it also rotates the muon's spin. Typically two settings of the separator are used, one that rotates the spin very little, and one that rotates it by 90°.

- After filtering the beam is focused electromagnetically on the target material of interest.

Once a beam of spin–polarized muons is produced in the above manner, it can be used in a $\mu\mathcal{SR}$ experiment. Such experiments are described in the following section.

2.1.3 $\mu\mathcal{SR}$ Experimental Setup and Data

The experiments described in this thesis were conducted on the M13, M15 and M20 beamlines at TRIUMF, which provide high intensity beams of ~100% spin polarized positive surface muons. The kinetic energy of surface muons (~4.1 MeV) gives them a mean stopping range of 140 mg/cm^2; consequently, $\mu\mathcal{SR}$ is essentially a bulk probe.

One can follow the spin-polarization of an ensemble of implanted muons via detection of their high energy decay positrons which, due to the asymmetry of the weak decay of the muon, are emitted preferentially along the direction of the parent muon's spin. The muon and its decay positron are detected in fast plastic scintillation detectors. The muon detector is thin enough ($\approx$0.25mm) that muons will pass through it. Typically there is an array of between 1 and 4 positron detectors in well defined directions relative to the magnetic field at the sample position. The histogram of the time differences between muon implantation and decay positron detection in counter i is of the form:

$$N_i(t) = N_{i0}e^{-t/\tau_\mu}[1 + A_i\mathbf{P}_\mu(t)\cdot\hat{\imath}] + B_i, \tag{2.4}$$

where N_{i0} is an overall normalization, B_i is a time–independent background, A_i is the experimental asymmetry typically in the range 0.2–0.3, $\hat{\imath}$ is a unit vector along the direction joining the centre of the sample to the centre of the solid angle subtended by the counter i, $\tau_\mu \approx 2.2\mu$s is the muon lifetime which sets the practical upper limit for the timescale of observable variations in $\mathbf{P}_\mu(t)$, the muon polarization. Through a variety of methods, one extracts $A_i\mathbf{P}_\mu(t)\cdot\hat{\imath}$ and fits the time dependence to an appropriate model.

Practically, the histogramming is accomplished with a Time–to–Digital Convertor (TDC). A good start event is defined logically by $S = M \cdot \bar{P}$, where M indicates that the muon counter has triggered, and $\bar{P}$ indicates that there isn't already a muon in the sample. The condition $\bar{P}$ ensures that subsequent positron detection can be associated unambiguously with the muon that starts the TDC. A good stop event is defined by $E = \Pi \cdot \bar{P}$, where Π indicates that a positron detector has been triggered. In addition, the time range which is measured is always limited by a data gate of arbitrary length, but typically it is set at about $5\tau_\mu$. The time between the S and E is measured by the TDC (LeCroy, model 4204), and the result is routed to the section of a histogramming memory unit corresponding to the particular positron counter.

There is a known flaw in the LeCroy 4204 TDC. The unit has an internal OR gate which takes as inputs the stop pulses from the various positron counters. The output of this internal OR is contaminated by a high frequency clock signal (usually above 300MHz), so using the output of the internal OR as the input to the TDC stop yields a sharp high frequency in the data (e.g. see Fig. 4.13b). The solution to this problem is straightforward. One simply uses a reliable high speed OR gate in place of the internal OR. The output of such an OR gate can be timed so that the stop pulses from it arrive at the stop input of the TDC at the same time they would have in using the internal OR. The clock signal contamination exists in some of the data of chapter 6, but for all recent data, we use the above "fix" to avoid the problem.

Another technique that is used in some of the data reported in this thesis is the newly developed "Separate Spectra Method"[100]. In this method a second thin muon counter is placed in the cryostat immediately in front of the sample. A high purity silver mask is placed in front of this muon counter, so that muons passing through the mask only stop in the sample. The standard outer muon counter is used for the starts, but the inner muon counter routes the stop events to one of two histograms for each counter, i.e. it

separates events from muons that stop in the sample from those from muons stopped in the mask. Thus, a calibration experiment is done *in situ*, under the same conditions of field and temperature. In addition, the amplitude of the sample signal is maximized by eliminating contribution due to background. Furthermore, it is found that the peak at the zero time of the histograms is eliminated in the sample spectra. The "t_0" peak is due to straigt–through events, mainly of positron contamination in the beam. The coincidence counting of the two muon counters eliminates the peak, since the positrons have little probability of triggering the thin muon counter (because they deposit little energy), and the probability for a positron triggering both muon counters is negligibly small.[1] Practically the routing in the Separate Spectra Technique is accomplished by initiating a data gate D for the inner muon counter, i.e. start D when $M_1 \cdot M_2 \cdot \bar{P}$, where M_i are the muon counter pulses. The stop condition is modified for the routing by demanding, for the sample spectra a coincidence with the gate D, and, for the reference spectra, coincidence with $\bar{D}$.

Such time–differential μSR measurements (in which $\mathbf{P}_\mu(t)$ rather than its integral is measured) fall into three geometric categories: longitudinal (LF), transverse (TF), and zero (ZF) field, depending on the direction of the applied magnetic field relative to the direction of the initial muon spin polarization (Fig. 2.6).

In the LF situation, the left (L) and right (R) counters play no role. The muons enter from the left, pass through the thin muon (TM) detector and, via the aperture in the "backward" (B) positron counter, pass into the sample. The initial muon spin polarization $\mathbf{P}_\mu(0)$ points backwards, and consequently, if the detection characteristics of the two symmetric counters are otherwise balanced, the B counter will initially detect

---

[1] One should be ware, however, that running the inner muon counter as a coincidence counter, i.e. with triggering level "in the noise" is somewhat dangerous, since decay positrons from muons in the sample may trigger the inner muon counter. This can lead to problems using this technique in LF mode where the B and F counters are separated by the inner muon counter.

more positrons on average than its "forward" (F) counterpart. After implantation, if the muon spin depolarizes in times shorter than $\sim 50\tau_\mu$, then the asymmetry in the count rates will decay with time. Often, $\mathbf{P}_\mu(t)$ simply decays exponentially , and the LF relaxation rate is exactly analogous to T_1^{-1} in NMR. In ZF, both T_1 processes and inhomogeneous static internal fields (for example, nuclear dipolar fields) contribute to the relaxation of $\mathbf{P}_\mu(t)$; whereas, in longitudinal fields exceeding the magnitude of any static internal fields, $\mathbf{P}_\mu(t)$ relaxes only by T_1. ZF $\mu S\mathcal{R}$ is thus a very sensitive site–based probe of static magnetism. In the TF geometry, $\mathbf{P}_\mu(0)$ is perpendicular to $\mathbf{H}$, and $\mathbf{P}_\mu(t)$ exhibits oscillations at the Larmor frequency determined by the value of the magnetic field at the muon and the gyromagnetic ratio, $\gamma_\mu = 135.54$ MHz/T. The TF experiment is analogous to the free induction decay of NMR with the TF relaxation rate being identified with T_2^{-1}. An example of the time histogram of a single counter in a TF experiment (following Eq. (2.4)) is given in Fig. 2.7a.

A schematic diagram (approximately to scale) of the typical setup is shown in Fig. 2.8. The four side counters were used in the TF measurements, and the cup shaped F counter and annular B counters were used in the LF and ZF measurements. In the original experiment[85], the sample was suspended on a thin sheet of mylar, and the vessel had windows on both sides of the sample. The apparatus could then be used in a low background mode[86] with the F cup playing the role of a veto counter. In this situation, the definition of a good start is modified to start only if the muon has landed in the sample, i.e. $S = M \cdot \bar{P} \cdot \bar{V}$, where V indicates that the veto counter has triggered (i.e. the muon has gone straight through and stopped in the cup shaped counter. In the TF situation, one can also use the veto counter to "shade" the side positron counters by defining a good stop as $S = \Pi \cdot \bar{P} \cdot \bar{V}$. This relies on the shape of the cup and the relative geometry of the cup and the side counters. With the availability of larger quantities of material this mode of operation was no longer necessary. The sample cell, F counter, and sample

thermometers were mounted on the end of a lucite lightguide sample rod in the He space of a helium gas–flow cryostat. For the standard sample cell, a high purity annular silver mask was placed immediately in front of the cell so that muons that did not enter the sample cavity would stop in the silver and contribute only a benign temperature independent background. Between the beamline vacuum and the sample, the muons passed through 4 Kapton windows, the muon counter, a small air–gap, a thin aluminized mylar heat shield, and a small gap in cold helium gas. The total stopping density that these intervening obstacles presented to the muons was about 63 mg/cm^2. Precautions were taken to keep this density as small and constant as possible by preventing condensation on the outer cryostat window and limiting the pressure of the He gas at low temperature. At high fields, the helical positron paths have curvature on the scale of the detectors, and the effective solid angles of the counters consequently change. For example, the count rate in the B counters shown in the figure fall off significantly above about 2T. Subsequent improvements to the B counters reduced this problem. The initial[85] data on R_3C_{60} and some of the data presented here used only the F counter, while some of the data used both F and B.

2.2   Sample Handling

The alkali fullerides are generally air–sensitive (although it has been reported that some of the A_1 materials are air–stable[87]). Consequently precautions must be taken to keep them in an inert environment. In addition, the samples are usually finely powered and difficult to press into pellet form, so thermal contact at cryogenic temperatures is maintained by the surrounding thermal exchange gas. Thus, in order to access a wide range of temperature, some fraction of the exchange gas must be Helium. Furthermore, the rather small range of surface μ^+ necessitates thin window(s) in any kind of sample

vessel. Practically for cryogenic temperatures, thin (2 or 3 thousandths of an inch thick) windows made of the polyamide film known as Kapton (from duPont) are used. For high temperatures, thin metal foil windows can be used, but the stopping density of such windows is usually considerably higher than for the Kapton. For example the 1 thou. (0.001") Ag foil window used in the high temperature cell up to 450K had a stopping density of ~ 26 mg/cm^2; whereas 2 thou. Kapton has only 7.2 mg/cm^2. Details of the sample vessels are given in Appendix B.

For the early measurements, mounting the samples in vessels was carried out at the Laboratory for Research on the Structure of Matter at the University of Pennsylvania. More recently, though, an inert atmosphere handling facility at the University of British Columbia has been refurbished and was used for sample mounting. This facility consists of a Vacuum Atmospheres Dri–Lab glovebox and associated equipment. The glovebox atmosphere is typically Ar with a fraction of He added prior to sample mounting.

2.3   Alkali Intercalation and Sample Characterization

The samples for all of the experiments desribed in this thesis were synthesized at The University of Pennsylvania by J.E. Fischer and coworkers, except the K_1C_{60} sample which was made at Ohio State University by H. Guerrero and R.L. Cappelletti. The process by which the alkali fulleride salts are made is high temperature solid state intercalation. Such processes are familiar in the synthesis of intercalated graphite compounds, such as KC_8 (a $T_c = 140$mK superconductor [90]). Stoichiometric quantities of high–purity oxygen–free C_{60} and alkali metal are weighed and sealed in a vessel, e.g. quartz tube or oxygen–free copper cell. Then the cell is subjected to a baking and annealing process (at modest temperatures $\sim 150°C$) over the course of weeks (e.g. [4]). For mixed compounds, this sometimes involves interrupting the baking process to mix or grind the material.

The alkali vapour diffuses slowly into the lattice of C_{60} molecules, and the result is a fine black powder. Other intercalation strategies have also been developed, such as reaction of (highly explosive) alkali azide compounds with C_{60} or a previously intercalated C_{60} compound[91], and dilution of higher stoichiometric alkali fullerides with pure C_{60} (e.g. [92]).

Samples were typically characterized by standard techniques such as x–ray diffraction and magnetization. The grain size of the powders was $\sim 10^4$Å, but the x-ray powder pattern linewidths give a crystalline coherence length, ξ_{XTL} of 500–1000Å. Such measurements also put limits on the presence of impurity phases (e.g. Rb_4C_{60} in Rb_3C_{60}). Typically such limits were $\leq 5\%$. From magnetization measurements in the superconducting state, the shielding fraction was typically 60%, and the Meissner fraction 10% (for a loose powder). The superconducting transition was found to be quite sharp, with a transition width of less than 0.25K, for example, see [93].

For the experiments described here, typically a few hundred milligrams of the powder was sealed under 1 atmosphere of 90% Ar/10% He. Synthesis of large single crystals of C_{60} intercalation compounds has proven quite difficult, but recently, a crystal with mass in the order of 100mg has been made.[94]
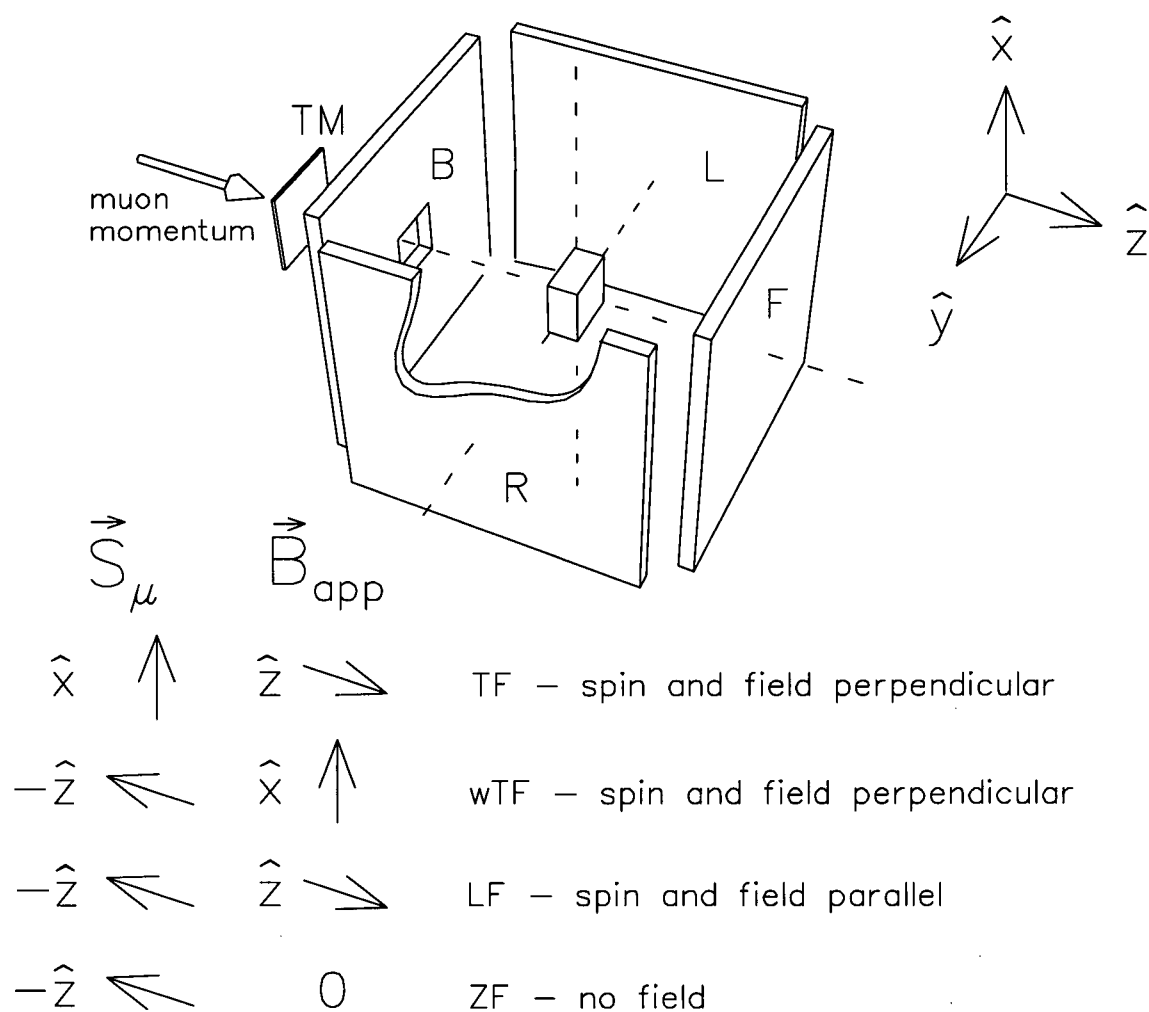
Figure 2.6: General counter arrangement for a $\mu\mathcal{SR}$ experiment.
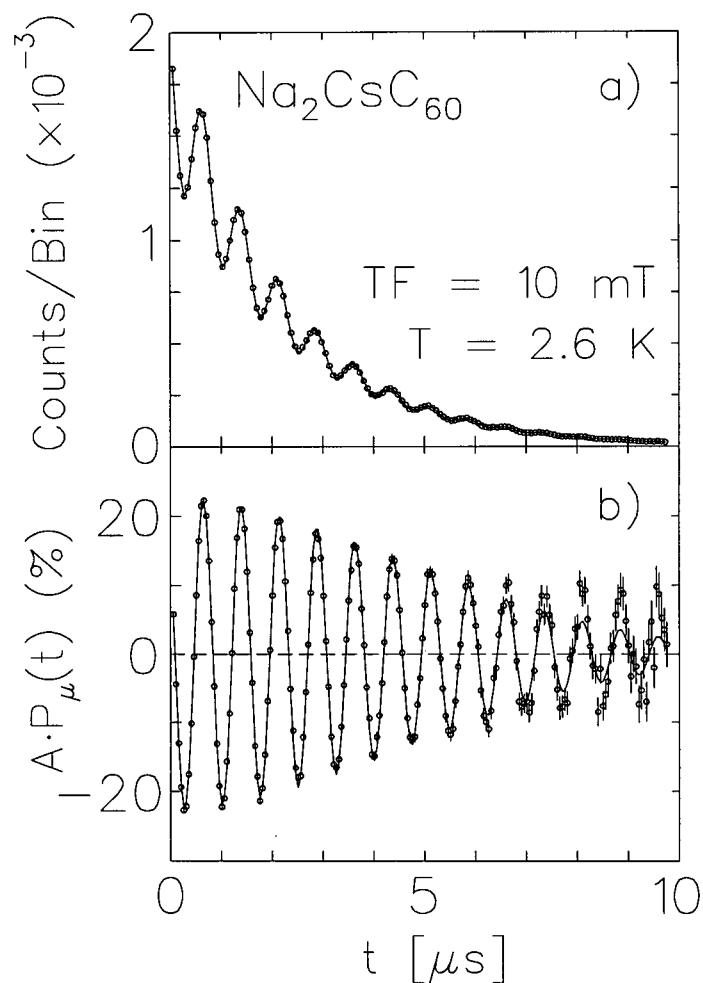
Figure 2.7: *a)* The time histogram of muon–positron decays detected in a single counter in Na_2CsC_{60} in 10 mT transverse field (see Eq. (2.4)). *b)* The same data combined with another histogram to remove the muon lifetime. A small non-relaxing signal, due to muons not stopping in the sample, is evident at late times. The relaxation is discussed in §4.2.
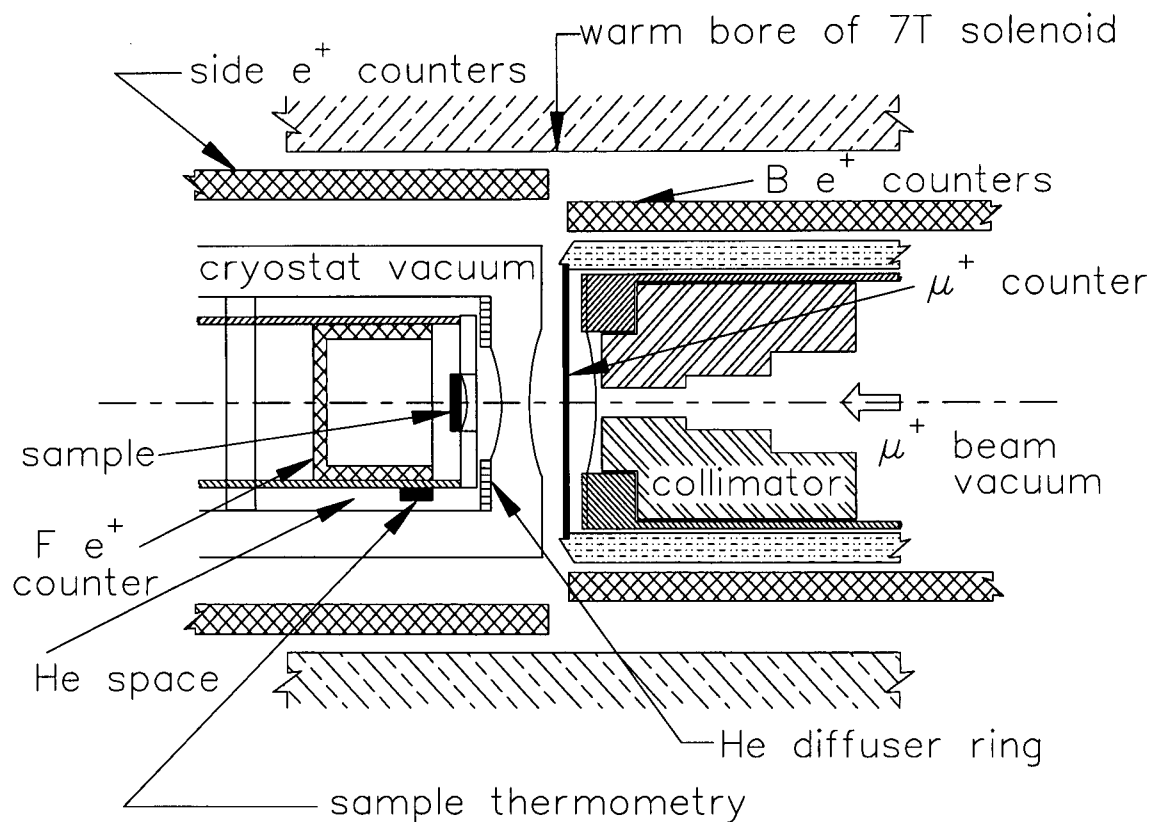
Figure 2.8: Sketch of the apparatus. The superconducting solenoid bore is 6" in diameter and 24" in length.

Chapter 3

LF (T_1) Relaxation and Superconductivity

3.1 Spin Exchange Relaxation of Muonium

In this section, we include a brief description of muonium (the bound hydrogenic atom $\mu^+ e^-$) and its T_1 spin relaxation due to collisions with free electrons. A comparison with analogous nuclear spin relaxation is also made.

The hyperfine spin hamiltonian for an isolated isotropic Mu is:

$$H/h = \gamma_e \mathbf{S}_e \cdot \mathbf{B} + \gamma_\mu \mathbf{S}_\mu \cdot \mathbf{B} + A_\mu \mathbf{S}_e \cdot \mathbf{S}_\mu \tag{3.1}$$

where γ_i are the gyromagnetic ratios, A_μ is the Mu hyperfine parameter, $\mathbf{S}_i$ are the spins and $\mathbf{B}$ is the applied magnetic induction. This hamiltonian can be diagonalized analytically to give the field–dependent hyperfine energy levels which are plotted in a Breit–Rabi diagram, e.g. Fig. 3.9. The transition frequencies are conventionally[75] labelled $\nu_{ij} = (E_i - E_j)/h$, with E_i numbered according to Fig. 3.9. More detailed accounts of Mu (including anisotropic coupling) can be found elsewhere[75, 96].

In metals, the predominant mechanism for T_1 relaxation of *nuclear* magnetization is via interaction with the conduction electrons within kT of the Fermi surface[97, 98]. The interaction is usually modelled[98, 99] by a direct hyperfine contact hamiltonian:

$$H^i = A_n \mathbf{I} \cdot \mathbf{S_e}, \tag{3.2}$$

where $\mathbf{I}$ is the nuclear spin, and the coupling A_n depends on the square modulus of the band electron wavefunction at the nucleus. The analogous coupling for a bare muon in
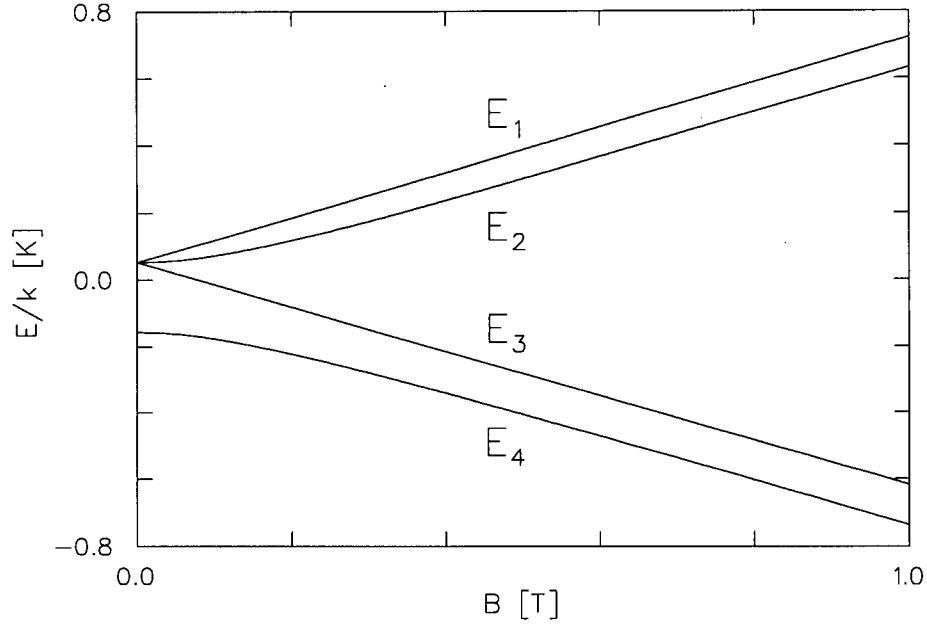
Figure 3.9: Breit–Rabi Diagram: The field dependence of the hyperfine energy levels (in Kelvin) of an isotropic muonium atom. The hyperfine coupling parameter here is the value for free Mu, $A_\mu = 4.463302$ GHz.

conventional metals causes relaxation which is always too slow to observe on the muon timescale (i.e. $T_1 \gg 10\mu s$) (see §3.2.4 of Cox[76]). However, T_1 can become short enough to observe in semi–metals such as graphite[100] and antimony[101] where the presence of a local electronic moment at the muon is permitted by weaker screening of the muon's coulomb potential. The actual coupling mechanism relevant for NMR T_1 in A_3C_{60} has, in addition to Eq. (3.2), an important anisotropic contribution originating from the full electron–nucleus magnetic dipolar interaction, as discussed in detail elsewhere[102, 103].

For endohedral muonium in A_3C_{60}, we are in the unusual situation of having a strongly bound paramagnetic muonium centre in a metallic environment. The interaction between a paramagnetic centre and the conduction electrons is more complicated than Eq. (3.2) because of the extra degrees of freedom of the bound electron. Nevertheless, we can

model the interaction in a similar way: first, we neglect scattering into higher orbital states because such processes require orbital energies which are not available at low temperature; second, we can neglect the direct muon–conduction electron coupling as mentioned above. The spin–independent Coulomb interaction together with the Pauli principle, can then be modeled by the simple spin–exchange hamiltonian:

$$H^i = J(r)\mathbf{S}_e \cdot \mathbf{S}_e^{Mu} \tag{3.3}$$

where r is the separation of the scattering electron and the Mu atom, $J(r)$ is a short–range scattering potential[104], and the Muonium electron spin is distinguished from the conduction electron spin by the superscript. The effect of this interaction is to randomly flip the muonium electron spin (Fig. 3.10), consequently producing a random modulation in the local field at the muon and causing the muon's spin to relax.

The theory of such spin relaxation has been worked out in several contexts using various methods[105]. For the case of isotropic Mu hyperfine coupling A_μ, the behaviour of the LF (T_1) muon spin–relaxation rate due to spin–exchange is divided into two regimes by a crossover when the rate of spin–exchange events (ν_{SE}) equals the "2–4" muonium hyperfine frequency (ν_{24}), which at high fields ($B \gg A_\mu/\gamma_e$) is approximately the electron Zeeman frequency. In the fast region ($\nu_{SE} \gg \nu_{24}$), the relaxation rate is approximately field independent, and in the slow regime the relaxation rate is governed by:

$$T_1^{-1} \approx \frac{A_\mu^2 \nu_{SE}}{2[A_\mu^2 + ((\gamma_e + \gamma_\mu)B)^2]}. \tag{3.4}$$

As Chow discovered[106], the relaxation rate in the case where the muonium hyperfine interaction is anisotropic can be dramatically different. There is a peak in $T_1^{-1}(B)$ at a field determined by the hyperfine parameters which is the result of the geometry of the effective local field at the muon. While this peak has only been observed in doped crystalline semiconductors, it is expected to survive, in perhaps a very broadened form,

an orientational powder average. From the high symmetry of the site at the centre of the C_{60} cage, we expect Mu@C_{60} to have an essentially isotropic hyperfine interaction. Although *a priori* one might expect that Mu inside the cage could bond to a single carbon, forming a highly anisotropic endohedral radical, calculations[173] suggest that such a state is not stable. In pure and insulating alkali–doped C_{60} phases[14, 107], this conclusion is confirmed by observation of very narrow coherent spin precession lines from Mu@C_{60}. In contrast, the *anisotropic* exohedral radical in pure C_{60} exhibits a much broader signal at low temperature (see Fig. 4.13). For nearly isotropic muonium with a large hyperfine interaction, the deviation from Eq. (3.4) will occur only at extremely high fields where the *muon* Zeeman interaction is comparable to the hyperfine interaction.

In analysis of the temperature dependence of the relaxation rate, it is of interest to consider the degree of inelasticity of the direct and spin–exchange scattering processes. In the case of the direct interaction Eq. (3.2), the nuclear spin and conduction electron spin flip–flop (Fig. 3.10), requiring an energy $\alpha_m = |(\mu_B - \mu_{nuc})B|$; whereas, in the muonium spin–exchange reaction Eq. (3.3), the electron Zeeman energies balance and the energy required is

$$\alpha_m = A_\mu/2, \tag{3.5}$$

independent of magnetic field. For the case of vacuum muonium α_m corresponds to a temperature of about 0.1K compared to an $\alpha_m(B = 10T)$ of 13.4K for Korringa relaxation of nuclear spins.

3.2 Spin Relaxation in Superconductors

3.2.1 General

The effective interactions Eqs. (3.2,3.3) between the conduction electrons of a metal and a nuclear or muonium electron spin may be treated as first order scattering problems[98].

According to Fermi's golden rule, the rate of transitions between spin states is determined by

$$W_{ab} = \frac{2\pi}{\hbar} \sum_{\mathbf{k},\sigma,\mathbf{k}',\sigma'} |\langle a\mathbf{k}\sigma|H^i|b\mathbf{k}'\sigma'\rangle|^2 \delta(E_{\mathbf{k}} - E_{\mathbf{k}'} + \alpha_m) f_{\mathbf{k},\sigma}[1 - f_{\mathbf{k}',\sigma'}], \qquad (3.6)$$

where $\mathbf{k}$ and σ label the conduction electron momentum and spin states; $E_{\mathbf{k}}$ is the corresponding kinetic energy and $f_{\mathbf{k},\sigma}$ the occupation probability; a and b label the nuclear or muonium spin states; and $\alpha_m(\sigma_i)$ is the change in magnetic energy. The sum in Eq. (3.6) can be converted to an integral over energy in the usual way, using the (normal state) electronic density of states (DOS), $g_N(E)$, where E is measured relative to E_F. Assuming that $g_N(E)$ doesn't vary much for E within a few kT of the Fermi energy, one can neglect the small inelasticity of the collisions, and use $g_N(E) \approx g_N(E') \approx g_N(0)$. Doing so, one obtains the Korringa law:

$$R_N \equiv (T_1^{-1})_N \propto g_N^2(0)kT \qquad (3.7)$$

In the superconducting state, the expression for the nuclear transition probability Eq. (3.6) is formally the same, but the scattering is accomplished by the bogolons (quasi–particle excitations of the superconducting state), which differ in two important respects from conduction electrons of the normal state: i) there are phase correlations between states of opposite momentum and spin which necessitate combination of pairs of matrix elements *before* squaring (see, e.g. §3.9 of Tinkham[108]) and give rise to the "coherence factors"; and ii) the excitation spectrum near E_F is strongly modified: the DOS is gapped and the gap is flanked on either side by singular peaks. The DOS, predicted by BCS[42], (see Fig. 3.11a) is:

$$g_S(E) = g_N(E)\Re\left\{ \frac{|E|}{\sqrt{E^2 - \Delta^2}} \right\} \qquad (3.8)$$

where $\Re$ is the real part,[1] E is the energy measured from E_F, and $\Delta(T)$ is the order

---

[1] The real part is here simply a convenient way to define g_S so that $g_S = 0$ for $|E| < \Delta$.

parameter, which for the moment we consider to be real, isotropic and homogeneous. Applying these modifications, we get the following integral for the T_1 relaxation rate in the superconducting state (normalized to the rate in the normal state)[109]

$$\frac{R_S}{R_N} = 2\beta \int_0^\infty \Re\left\{\sqrt{\frac{(EE'+\Delta^2)}{(E^2-\Delta^2)}}\right\} \Re\left\{\sqrt{\frac{(EE'+\Delta^2)}{(E'^2-\Delta^2)}}\right\} f(E)(1-f(E'))dE, \quad (3.9)$$

where $\beta = (kT)^{-1}$, f is the Fermi-Dirac distribution function, and $E' - E = \alpha_m$. Neglecting any spin–polarization of the quasiparticles, the exothermic and endothermic scattering events will be equally probable, and we take the ratio R_S/R_N to be the simple average of the integrals Eq. (3.9) with α_m both positive and negative. If the inelasticity of the collisions is neglected ($\alpha_m = 0$), the two singularities in the integrand coalesce, and the integral becomes logarithmically divergent; however, the singularity is not a practical problem because α_m is finite, and, more importantly, the peak in the DOS is broadened from the BCS result Eq. (3.8), as will be discussed in detail in §3.2.3. As a function of decreasing temperature, Eq. (3.9) exhibits a peak just below T_c, due to the peaked DOS factors, and at lower temperatures, falls off exponentially. For $\alpha_m \approx 0.002\Delta(0)$ (appropriate to the case of Mu in Rb$_3$C$_{60}$, if it is a BCS superconductor), and assuming the BCS temperature dependence $\Delta(T)$, the maximum of R_S/R_N is about 4 (see Fig. 3.11b).

3.2.2 Low Temperature Behaviour

Typically, the low temperature behaviour of Eq. (3.9) is approximated by an Arrhenius law (e.g. [165]),

$$R_S/R_N \sim \exp(-\Delta_0/kT) \quad (3.10)$$

while this certainly accounts for the majority of the low T dependence, it is not the complete dependence. Perfect Arrhenius behaviour is only rigorously found if the integrand of Eq. (3.9) is gapped but otherwise featureless in energy. The strongest energy

dependence one might expect in the integrand (for a gapped density of states) is that of BCS Eq. (3.8). Allowing for finite α_m, the singular behaviour of the square of the BCS density of states is avoided, and the integral can be expanded at low T in terms of modified Bessel functions, giving a temperature dependent prefactor to the Arrhenius dependence of $T^{-1/2}$. This is analogous to the temperature dependence of the penetration depth[108, 111, 112]. $T^{-1/2}$ is a weak function of temperature compared to Eq. (3.10), but it does lead to a significant bias in the energy gap extracted using Eq. (3.10). For example, if one fits Eq. (3.10) to data that varies as $T^{-1/2} \exp\left(-1.76 T_c/T\right)$, over a range of reduced temperature $t = T/T_c$ of 0.25–0.5 (typical for many NMR studies), one finds $\Delta_0 = 1.56 k T_c$, and the Arrhenius plot doesn't deviate noticeably from linear. While the specific $T^{-1/2}$ dependence is highly idealized, this example illustrates the dangers of using a simple model such as Eq. (3.10) especially over a restricted range in temperature. The low temperature behaviour in cases less ideal than Eq. (3.8) will be determined by balancing the contributions of both the peak in $g(E)$ at Δ (if it is present), and any finite $g(E)$ within the "gap", with the latter always dominating at the lowest temperature because of the exponential weighting of the Fermi factor. We will consider more realistic models for $g(E)$ in the next section.

3.2.3 Extensions

The temperature dependence of Eq. (3.9) discussed above can be modified through several mechanisms which we will consider in turn: anisotropy of Δ, finite lifetime of quasi-particle excitations, and magnetic effects.

The consequences of anisotropy on the ratio R_S/R_N are found by including an angular integral in Eq. (3.9), and they can be most easily explained by a comparison between the

angular average DOS, $g_A(E)$, and $g_S(E)$ of Eq. (3.8).

$$g_A(E) = g_N(E)\Re \left\{ \int_{a1}^{a2} \frac{E}{\sqrt{E^2 - \Delta_G^2(1 + a^2)}} P(a)da \right\}, \qquad (3.11)$$

where $P(a)$ is the distribution of the anisotropy a of the gap around the Fermi surface. Even a small anisotropy, such as that for aluminum[109], transforms the BCS singularity in $g_S(E)$ into a mild van Hove singularity at some average Δ_P, and g_A is still perfectly gapped with $g_A(E) = 0$ for $|E| \leq \Delta_G$ (see Fig. 3.11a). The effect of anisotropy is thus to reduce the size of the coherence peak in R_S/R_N and to modify the Arrhenius slope relative to the isotropic case. Extreme anisotropy, such as that for non–zero angular momentum pairing states, is similar except that g_A is no longer gapped as there are nodes in Δ. For example, for a d–wave order parameter[113], $g_A(E) \propto E$ as $E \to 0$. Although g_A is still peaked in this situation, the coherence peak in R_S/R_N may be completely eliminated[114], and the exponential temperature dependence is replaced by a power law $R_S/R_N \propto T^p$, where $p = 2$ for d–wave, and other values of p are obtained[115] for different nodal structures of Δ. This kind of behaviour has been observed[116, 117] in $YBa_2Cu_3O_{6.95}$, for which there is strong evidence of a d–wave Δ. A p–wave Δ may be the source of similar temperature dependence in some Heavy Fermion superconductors[118, 119], while one dimensionality may cause it in some organic superconductors[120].

Finite lifetime (τ) of the quasiparticle excitations of a superconductor due, for example, to electron–phonon, electron–electron or impurity scattering can also modify R_S/R_N. This possibility was suggested by Hebel and Slichter in their original work[99] to explain the small size of the coherence peak they observed in Al. They calculated a DOS which was a version of Eq. (3.8) smeared by convolution with a gate function of width τ^{-1}. A detailed analysis of the temperature dependence of R_S/R_N resulting from this approximation is given by Hebel[121]. A different Ansatz for the DOS was used by Dynes *et al.*

[122] to describe tunneling measurements:

$$g_D(E) = g_N(E)\Re\left\{ \frac{E + i\Gamma}{\sqrt{(E + i\Gamma)^2 - \Delta^2}} \right\}, \tag{3.12}$$

where $\Gamma \sim \tau^{-1}$. However, Allen and Rainer[123] point out that for a lifetime due to *electron–phonon* scattering, one must resort to the Eliashberg theory of strongly coupled superconductors (see §1.4.3) in which the order parameter becomes complex, and the DOS is[126]

$$g_{SC}(E) = g_N(E)\Re\left\{ \frac{E}{\sqrt{E^2 - (\Delta_1 + i\Delta_2)^2}} \right\}, \tag{3.13}$$

where[127] $\Delta_2 = \Im\Delta \sim \tau^{-1}$ ($\Im$ is the imaginary part), and $\Delta = \Delta(E,T)$ is determined by the Eliashberg theory and the coupling constant–phonon spectrum product $\alpha^2 F(E)$ for the particular material. Fibich[128] first treated the problem of calculating R_S/R_N using Eq. (3.13) by neglecting the energy dependence of Δ, and simply using Δ evaluated at the energy which is most important for the integral Eq. (3.9), i.e. $\Delta(E = \Delta_1(T), T)$. The temperature dependence for the imaginary part $\Delta_2(T)$ due to phonon scattering[128, 129] and scattering from other quasiparticles[127, 130] has been calculated in the low temperature limit. For the temperature dependence of the real part $\Delta_1(T)$ (and for the parameter Δ in either of the preceding models) it is reasonable[124] to assume that the temperature dependence of the real part of the order parameter is approximately that of the BCS Δ. Recently, it has become feasible[131, 123] to calculate R_S/R_N using the full strong–coupling $\Delta(E, T)$, thus avoiding these approximations. As input to such a calculation, one would ideally first obtain a reasonable form for $\alpha^2 F(E)$. However, according to Akis[131], the details of $\alpha^2 F(E)$ are not important, and the most significant information in determining $R_S/R_N(T)$ is summarized in the ratio $T_c/E_{\log}$, where $E_{\log}$ is the logarithmic moment of $\alpha^2 F(E)$ (Eq. (1.8)). Note that the effect of impurities in the Eliashberg theory has recently been revisited[132]. These authors find that "vertex

corrections" from impurity scattering can *increase* the size of the coherence peak as the mean free path is reduced.

Magnetism may also influence $R_S/R_N(T)$, for instance, in the classical example[133] of gaplessness in a superconductor due to the presence of magnetic impurities, the coherence peak can be reduced or eliminated and the exponential fall–off strongly modified[134, 135]. Superconductors that are intrinsically magnetic exhibit similar strong deviations[118, 136]. In regard to high-T_c superconductors, antiferromagnetic correlations between quasiparticles have also been shown[114, 131] to damp the coherence peak. However, it should be noted that no anomalous behaviour connected with magnetism has been reported yet in A_3C_{60}. Recently[137], the closely related $NH_3K_3C_{60}$ material which is superconducting under high pressure has been found to exhibit a metal–insulator transition to a magnetic state[138] at about 40K. The small bandwidth and large coulomb interactions between electrons also cause important correlation effects, for example the magnetism in o–A_1C_{60}. The proximity to a similar magnetic phase may be enhanced by the analogous polymerization[139] of the C_{60} anions in the Pa$\bar{3}$ materials.

3.2.4 Influence of the Vortex State

Measurements of T_1 in type–II superconductors ($\lambda > \sqrt{2}\xi$) are typically done with the applied field above the lower critical field, H_{c1}, i.e. in the vortex state. The magnetic field interacts with the electronic system in two ways: i) via the Lorentz force embodied in the canonical momentum $\mathbf{p} + q\mathbf{A}$ and ii) via the Zeeman interaction of the electronic spins $\boldsymbol{\mu} \cdot \mathbf{B}$, consequently modifying the quasiparticle excitation spectrum and hence the temperature dependence of R_S/R_N relative to Eq. (3.9).

The Lorentz force, together with the magnetic field energy, yields the vortex structure of the mixed state wherein the field and the order parameter are *inhomogeneous*, for example, the Abrikosov flux lattice (see the review [140]) or more disordered phases [141].

Near H_{c2}, where the order parameter is small, the effect of the inhomogeneity $\Delta(\mathbf{r})$ has been treated theoretically in the dirty[142] and clean[143] limits and, subsequently, for arbitrary[144] mean free path l. In the dirty limit the effect of the DOS[142] is, in close analogy with the Abrikosov–Gor'kov theory of gapless superconductivity[145, 146] in the presence of magnetic impurities,

$$g(E, \mathbf{r}) \approx g_N(E) \left\{ 1 + \frac{|\Delta(\mathbf{r})|^2}{2} \frac{E^2 - \eta^2}{(E^2 + \eta^2)^2} \right\}, \qquad (3.14)$$

where η is the pair–breaking perturbation parameter[145, 142], $\eta \propto \tau B$, where τ is the collision time. The DOS exhibits no gap. In the clean limit[143] the DOS is highly anisotropic with singular BCS (Eq. (3.8)) behaviour along the magnetic field and gapless behaviour perpendicular to the field. The latter property has been confirmed and exploited in measurements of de Haas–van Alphen oscillations in the mixed state at high fields[147]. The effect of finite mean free path in this case is to wash out the anisotropy (and with it the BCS singularity) and to make the density of states a rigorously local property[142].

Away from H_{c2}, the expansions assuming small Δ are not applicable. The more general theories are very complex, but some approximate results have been obtained. There are two main approaches used to calculate properties of the vortex state in the regime $H_{c1} \ll H \ll H_{c2}$: the Green's function approach of Gor'kov[148] and the effective Hamiltonian approach of Bogoliubov and deGennes[142]. Using the second approach, the presence of bound, nearly gapless excitations in the vortex cores was predicted[149]. Far from the vortex cores, the excitation spectrum is modified only by the "Doppler shift" of the quasiparticle energies due to the circulating supercurrents. Neglecting the core states, Cyrot[150] calculated an explicitly field dependent DOS. These calculations show that the peaks of the zero field DOS are broadened significantly as the vortex spacing decreases below about 10ξ. Motivated by STM measurments of the detailed

spatial structure of the vortex state, this method has been revisited recently, e.g. see references[151, 152]. In contrast to the local nature of the dirty–limit, where the core contributions can be modelled simply as normal electrons, in the clean–limit, the interplay between the core states and the surrounding superconductor may be very important[152]. The Green's Function approach has been employed generally using a linearized version of Gor'kov's equations. For the dirty limit, the field–dependent local and spatially averaged DOS has been calculated numerically[153]. The spatially averaged DOS peaks in this calculation also exhibit field–dependent broadening. Clean–limit calculations have also been performed[154]. Recent use of this technique[156, 155] has concentrated on the structure of the vortex core.

It has long been recognized[157] that the Zeeman interaction acts to break the Cooper pairs of a conventional superconductor because it acts in the opposite sense on each member of the pair. The magnetic field at which the Zeeman interaction will destroy superconductivity can be approximated by equating the gain in energy in going to the (spin–polarized) normal state with the condensation energy of the superconductor, thus defining[158] the Pauli limiting field B_P:

$$B_P(t) = \frac{B_c(t)}{\sqrt{(1 + \chi_N)^2 - (1 + \chi_S(t))^2}}, \qquad (3.15)$$

where $B_c(t)$ is the thermodynamic critical field and χ_i is the spin susceptibility in each of the phases. The modification of the upper critical field H_{c2} due to these considerations has been calculated[159, 158], and its effect on the spectrum of excitations has been predicted to be negligible[145] unless there is some mechanism for mixing quasiparticle states of opposite spin, e.g. spin–orbit scattering. In the case of strong spin–orbit scattering, the quasiparticle spectrum is again of the form Eq. (3.14) with the pair–breaking parameter $\eta \propto \tau_{so}B^2$, where τ_{so} is the time between spin–orbit scattering events[145].

Despite these complications in the vortex state, many of the general features of the

zero–field (Meissner state) behaviour of R_S/R_N as discussed in §3.2.1 are observed experimentally. Fig. 3.12 shows the phase diagram of the vortex state, for an extreme (H_{c1} coincides with the horizontal axis on this scale) type–II superconductor showing regimes of different behaviour for T_1 in the most conventional case. To the lower right is the region of the Hebel–Slichter coherence peak. To the left is the "Arrhenius region" where the relaxation rate falls exponentially. Above about $0.7 H_{c2}$, the theories based on the gaplessness due to a small inhomogeneous order parameter $\Delta(\mathbf{r})$ are applicable. In particular $R_S/R_N(T, l \to 0)$ has been calculated[160] with the result, that the peak is reduced but still present in region (ii), and completely eliminated in region (i). The high field damping and elimination of the coherence peak predicted by this theory has been clearly verified experimentally[161] in the A15 superconductor V_3Sn. The calculation of $R_S/R_N(T, l)$ can be found elsewhere[162].

Departures from the exponential fall–off of the relaxation rate with temperature are typically seen at low temperature (region 2C). In this region, the much more weakly temperature dependent relaxation from the electronic excitations in the vortex cores can be significant[163]. One can model the relaxation of (muon or nuclear) spin polarization in such an inhomogeneous case using a local relaxation rate. The average relaxation function is

$$P_z(t) = \int_0^\infty dR e^{-Rt} P(R), \tag{3.16}$$

where the inhomogeneous T_1 rate $R(B(\mathbf{r}), \Delta(\mathbf{r}), T)$ is distributed as $P(R)$, and z indicates LF (T_1) relaxation. For $B \ll B_{c2}$, the vortices may be treated (in the dirty limit) approximately[149] as cylinders of normal state material of radius ξ. The distribution $P(R)$ in this approximation is bimodal with peaks at R_N and R_S. The relaxation $P_Z(t)$ will not be single exponential, but the average relaxation rate is[165]

$$\langle R_S/R_N \rangle = f_N + (1 - f_N) R_S/R_N, \tag{3.17}$$

where, for ($B \ll B_{c2}$), $f_N \sim \xi^2(B/\Phi_0)$, i.e. the weight in the distribution $P(R)$ at R_N scales linearly with field (Φ_0 is the magnetic flux quantum). This linear field dependence allows the deviation from exponential temperature dependence of the relaxation rate due to the vortex cores to be distinguished from the other mechanisms, such as impurity scattering, (region O) which at low temperature, and especially in low field, may limit the electronic relaxation. From the field dependence, one can thus use this model to extract a rough estimate[164, 165] of ξ deep in the superconducting state. Such estimates could be refined by including a more sophisticated local DOS[156, 151] in the model for $P(R)$, but dynamic effects might also require consideration. Motion of the vortices on the timescale T_1 would smear the distribution $P(R)$, effacing the bimodal structure of the static vortex state; however, vortex dynamics usually occur on timescales much shorter than a typical T_1[166], though exceptions have been proposed.[167] Another type of dynamics that has been considered in this context is that of spin–diffusion of the nuclear magnetization to the quickly relaxing regions of the cores which effectively allows the relaxation to "leak" out of the vortex cores into the surrounding superfluid. This mechanism, though, may be thermodynamically quenched in the inhomogeneous vortex state.[168] Furthermore, such a mechanism is not important in the experiments described here because we are always dealing with a single muon in the sample at any time, and Mu@C_{60} is static (at least on the length scales of the vortex lattice and on the timescale of the muon).

Deviations from the behaviour summarized in Fig. 3.12 are expected and observed in many cases: Reduction of the peak region (towards (t,h) = (1,0)) may be the result of any of the mechanisms discussed in the previous section. More detailed reviews of NMR in type–II superconductors can be found elsewhere.[109, 169, 170]
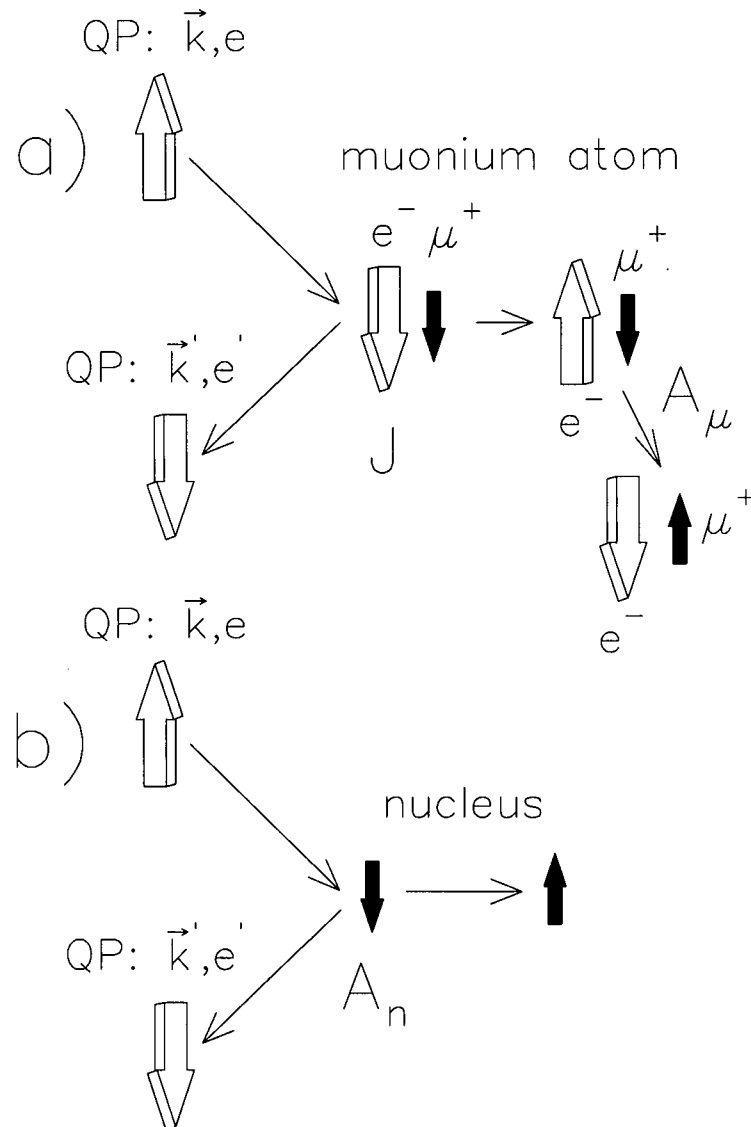
Figure 3.10: In each case a quasiparticle (QP) at the Fermi Surface with initial momentum **k** and energy e scatters magnetically from the local moment. *a)* Spin exchange of a muonium atom (with subsequent evolution due to the muon–electron hyperfine interaction A_μ) vs. *b)* Electron–Nuclear spin–flip. In the spin exchange with the paramagnetic muonium, the electron Zeeman energies cancel; whereas in the latter, the nuclear and electron Zeeman energies do not.
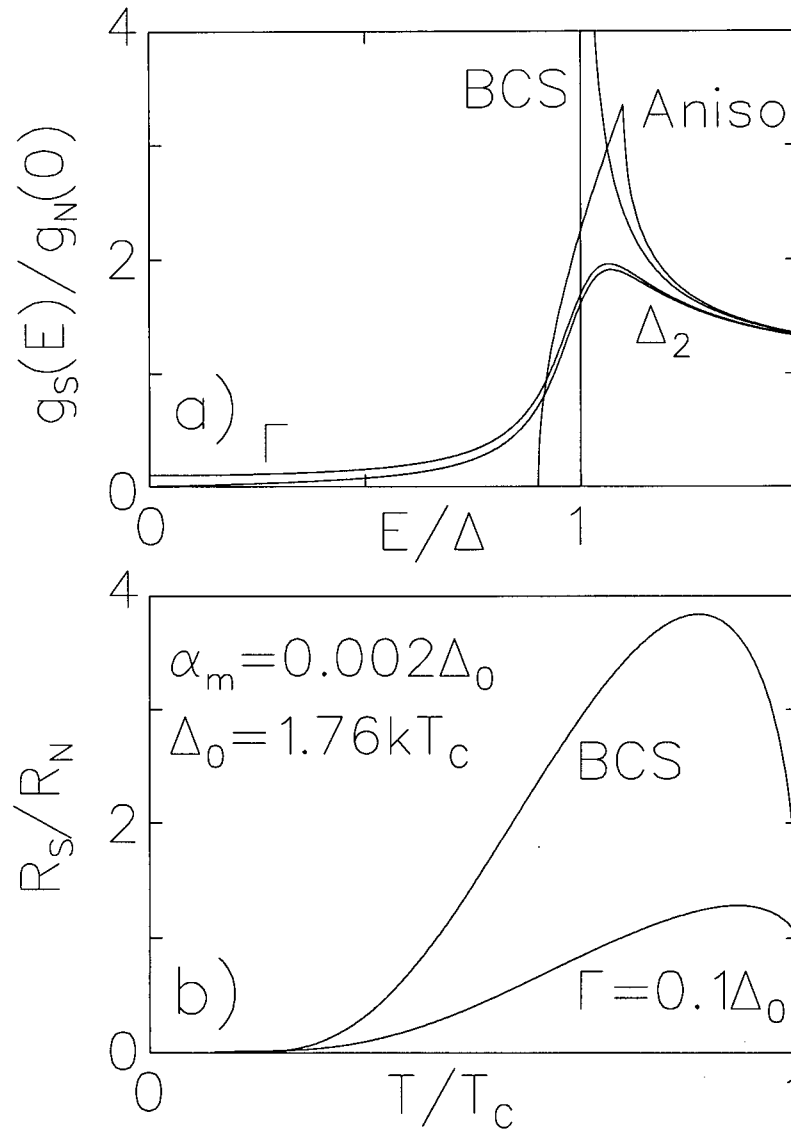
Figure 3.11: *a)* Models of the superconducting DOS: BCS is g_S of Eq. (3.8), Aniso is g_A (Eq. (3.11)) with a gate function distribution $P(a)$ of width 0.1Δ, Γ is g_D (Eq. (3.12)) with $\Gamma = 0.1\Delta$, and Δ_2 is g_{SC} (Eq. (3.13)) with $\Delta_2 = 0.1\Delta$. *b)* The value of the Hebel–Slichter integral for the BCS and lifetime (Eq. (3.12)) broadened $g_S(E)$. The magnetic inelasticity parameter (α_m) is appropriate for Mu@C$_{60}$ in Rb$_3$C$_{60}$. The BCS temperature dependence $\Delta(T)$ was used.
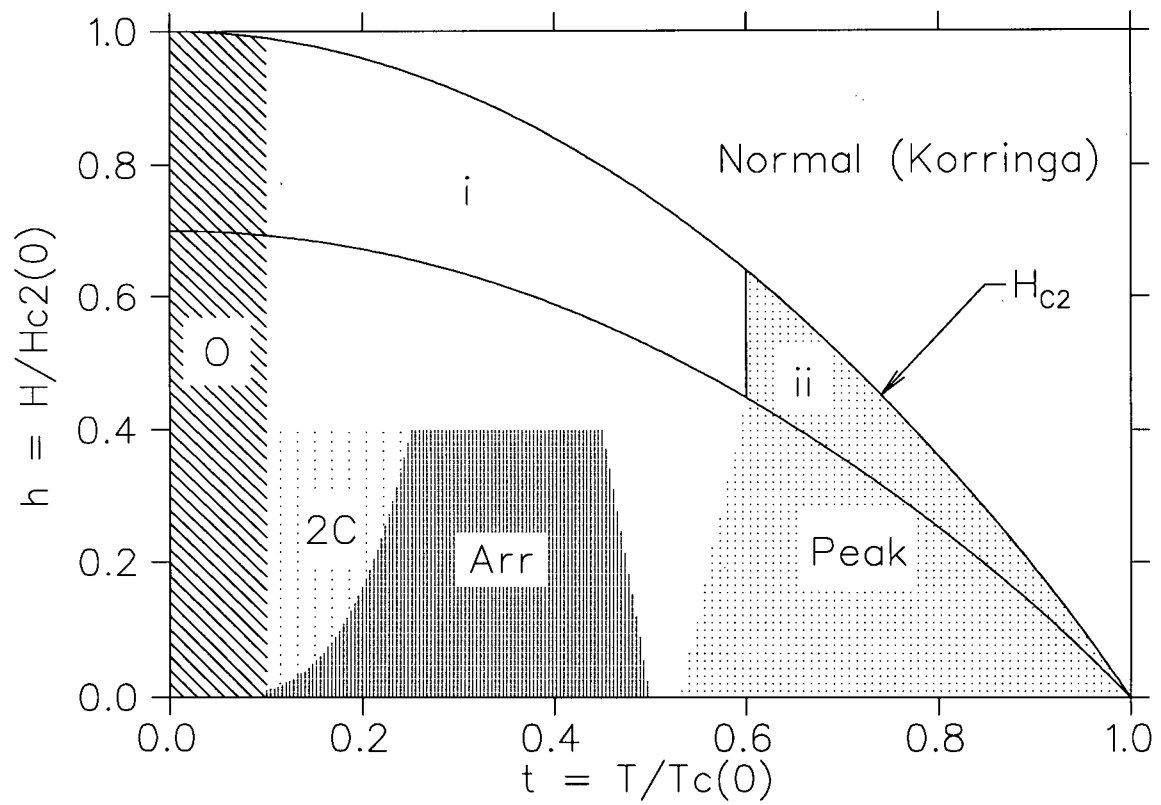
Figure 3.12: A generic phase diagram for the behaviour of $(T_1 T)^{-1}$ in a conventional type–II superconductor as described in the text.

Chapter 4

$\mu\mathcal{SR}$ in A_3C_{60}

4.1 μ^+ Sites in A_3C_{60}

When muons stop in typical metals, they occupy one or a few well–defined crys-
tallographic sites, usually interstitial, and remain diamagnetic; futhermore, they may in
exceptional cases diffuse between adjacent equivalent or inequivalent sites, often, because
of their small mass, exhibiting interesting quantum effects in their motion.[171] In insula-
tors and semiconductors, μ^+ often captures an electron to form paramagnetic muonium
which also occupies a specific interstitial site; however, the paramagnetic states almost
never occur in metallic environments either because the spin–flip rate due to collisions
with the conduction electrons is sufficiently fast to average the muon–bound electron
interaction to zero or because screening of the electrostatic potential precludes a bound
state entirely. Although the details of the particular sites adopted by the muon are not
critical to the analysis we report in the following sections, a brief discussion is included
here for completeness.

In C_{60} based solids, the available interstitial voids are much larger than in conventional
metals, and there are many potential sites for the muon, though some are occupied by
alkali ions in the alkali fullerides, i.e. the octahedral (O) and tetrahedral (T) interstitial
sites. In pure C_{60}, $\sim 80\%$ of the implanted muons form an exohedrally bonded muonium
radical ($C_{60}Mu$) which has been studied extensively.[107, 172, 173] In the ionic insulat-
ing fullerides K_4C_{60} and K_6C_{60}[14], and the conductors Rb_1C_{60}[174] and Rb_3C_{60}[85], a

similar fraction of the muons exhibit diamagnetic behaviour. Thus in both metallic and insulating environments, the exohedral C_{60}Mu radical does not survive the charging of the C_{60}. The large fraction of diamagnetic muons in FCC $A_3 C_{60}$ are certainly interstitial in the lattice of C_{60}^{-3} ions, but their precise positions are currently a matter of speculation. There are, however, some likely candidates which we will now discuss briefly. In the simplest scenario, the muon remains positive in the metal and its site(s) are determined essentially by the minimum electrostatic potential due to the surrounding ions. In such a situation, the muon would adopt a highly symmetric site, of which there are three obvious candidates: midway between two neighbouring O–sites; between T–sites; between an O and a T–site. Of course, polaronic lattice relaxation may complicate this scenario somewhat. Another possibility is that, due to its high electron affinity, the muon forms a complex with one of the interstitial alkali ions analogous to an alkali–hydride molecule. Which of these scenarios is realized will depend delicately on the energies involved. One would expect, if the nuclear dipolar fields were responsible for the room temperature TF linewidths in the alkali fullerides, that these widths might scale between systems with the average nuclear moment (possibly weighted by the inverse cube of the alkali–halide bond–length, e.g. Table A.1). We have, at present, no evidence for such a systematic variation either within the $A_3 C_{60}$ superconductors or between different phases. However, the small room temperature linewidths in some cases may have background contributions which could mask such variation. Measurements on single crystals, which have not yet been available in sufficient size for μSR, might be able to determine the muon site(s).[76, 75]

In both pure C_{60} and the insulating alkali fullerides, a small fraction of implanted muons ($\sim$10–20%) form a muonium atom characterized by a large isotropic hyperfine parameter which has been interpreted[175, 107, 14] to be trapped endohedral muonium (Mu@C_{60} pictured in Fig. 4.17a). Fig. 4.13 shows the clear signature for this state,

i.e. TF precession at frequencies determined by the hyperfine levels of Fig. 3.9. In
the metallic systems, however, these precession signals are expected to be unobservable
due to relaxation broadening either via the Korringa mechanism or by inhomogeneous
broadening in the vortex state of the superconductor or in the low temperature magnetic
phases of the A_1 metals. One possibility for observation of the oscillation, however, is at
the lowest temperature in zero field in the Meissner state of an A_3C_{60} superconductor,
where a high frequency oscillation (at the singlet–triplet splitting, $\approx$ 4.463 GHz) might
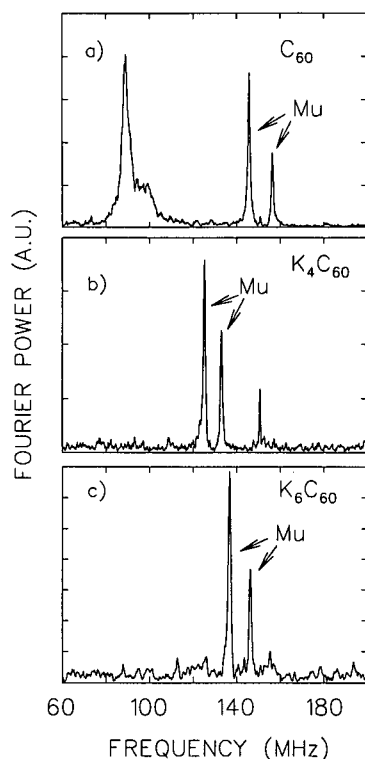
Figure 4.13: The TF precession signals of endohedral muonium in *a)* C_{60} at 10.7 mT, *b)*
K_4C_{60} at 9.6 mT and *c)* K_6C_{60} at 10.0 mT (from Kiefl[14]). The broad line in C_{60} is due
to the $C_{60}Mu$ molecular radical, and the narrow line at 150 MHz in the K_4C_{60} spectrum
is an instrumental effect. The frequencies and their field dependences correspond to
vacuum–like Mu with A_μ = 4341(24), 4342(66) and 4230(63) MHz respectively.

be observed because the Korringa and inhomogeneity broadening mechanisms will be negligible. Such high frequency measurements are technically quite difficult[176] and have not yet been attempted.

Even in the absence of measurable precession the presence of Mu@C$_{60}$ can be confirmed in LF experiments. Specifically, provided the T_1 relaxation of the μ^+ in the Mu@C$_{60}$ atom is in the muon time–range, the relaxation rate will have the characteristic magnetic field dependence of Eq. (3.4). We have observed this relaxation in the A$_3$C$_{60}$ superconductors and measured its field dependence at T=35K (well into the normal state). The relaxation is single exponential, and the rates as a function of field are plotted in Fig. 4.14a. The fits shown are to Eq. (3.4) with a small additional field–independent rate, R_0. Because the parameters A_μ and ν_{SE} are strongly correlated, they could not be determined independently, and we fixed $A_\mu = 4340$ MHz from the precession measurements in the insulators (Fig.4.13). This value is also consistent with measurements of A_μ in Rb$_3$C$_{60}$ discussed below. The resulting parameters are given in Table 4.4 along with the ratios

$$\rho_{35K}^x = \sqrt{\frac{\nu_{SE}^x(35K)}{\nu_{SE}^{Rb3}(35K)}}. \tag{4.1}$$

From the Korringa Law (Eq. (3.7)), this ratio is a measure of the ratio of the density of states at the Fermi Surface $g_N(0)$ relative to its value in Rb$_3$C$_{60}$. It is reasonable to assume A_μ is not strongly temperature dependent at low temperature, as is evidenced by Korringa temperature dependence of the relaxation rate in the normal state which is entirely the temperature dependence of ν_{SE}. Hence we can also fit the more accurately determined average value of $(T_1 T)^{-1}$ in the normal state to Eq. (3.4). These average values over several temperatures above T_c are shown in Fig. 4.14b. Fitting the Rb$_3$C$_{60}$ results to Eq. (3.4) with $A_\mu = 4340$MHz yields $\nu_{SE}/T = 20.2(4)$ MHz/K with $R_0/T = 4.4(7) \cdot 10^{-3} \mu s^{-1}$/K. Using this fit and the points for K$_3$C$_{60}$ and Na$_2$CsC$_{60}$, we calculate

the ratios,

$$\rho^x = \sqrt{\frac{(T_1 T)_N^{Rb3}}{(T_1 T)_N^x}}, \qquad (4.2)$$

which are also given in Table 4.4.

	$\nu_{SE}(35K)$[MHz]	R_0 [μs^{-1}]	ρ_{35K}^x	ρ^x
Rb_3C_{60}	587(47)	0.217(70)	1	1
K_3C_{60}	572(63)	0.215(50)	0.987(94)	0.950(31)
Na_2CsC_{60}	132(4)	0.0000(2)	0.474(25)	0.506(20)

Table 4.4: Parameters of the fits of $T_1^{-1}(B)$ at 35K to Eq. (3.4) with $A_\mu = 4340$MHz. As well as the ratios defined (relative to Rb_3C_{60}) in the text.

The low values of ν_{SE} (relative to A_μ) confirm that the slow spin–exchange limit form Eq. (3.4) is justified at this temperature and below (for all fields). In fact, ν_{SE} is remarkably slow compared to spin–exchange rates of Mu in semiconductors such as Si. In that case the spin exchange rate is usually[96] modelled as

$$\nu_{SE} = \sigma n(T)v(T), \qquad (4.3)$$

where one has extracted the majority of the temperature dependence of the Golden Rule expression (Eq. (3.6)) into the carrier concentration, n, and the mean thermal velocity v, leaving the nearly temperature independent sum over matrix elements in the appropriately defined cross–section σ. For interstitial Mu in Si, the observed ν_{SE} implies that σ is of the order of a typical atomic cross–section (10^{-15} cm^2). In the metallic case the situation is different since Pauli exclusion prevents all but the electrons within kT of the Fermi surface from participating in the spin exchange collisions. Thus $v \approx v_F$, the Fermi velocity and is nearly T independent, and $n \approx n_0 kT/E_F$. Using values[31] for Rb_3C_{60} ($v_F \approx 10^{-7}$cm/s, $E_F \approx 0.5$ eV, $n_0 \approx 4 \times 10^{21}$ cm^{-3}), σ for Mu@C$_{60}$ is 10^{-18}–10^{-19}

cm^2 at 35K. The small size of σ is attributed to the combination of two factors. First, the conduction band states are made up of C_{60} molecular orbitals in which the electrons are confined near the hollow carbon cage. The spatial distribution of the conduction electrons is thus quite inhomogeneous on the scale of the unit cell, and Mu@C_{60} is located in a site of low conduction electron density. Second, possibly for geometric reasons, there is very little hybridization of Mu@C_{60} with the surrounding C_{60} orbitals. The sp^2 carbon orbitals are distorted by curvature of the C_{60}, so that the inner lobes are smaller than the outer ones. Consequently, the tendency for bonding is significantly greater in the exohedral case.[173] The evidence for this is the large vacuum–like isotropic Mu hyperfine interaction. This is also consistent with the apparently very small ^{13}C–Mu nuclear hyperfine interaction[14] in pure C_{60}. In contrast, in semiconductors, the hyperfine parameters of muonium are much lower than the vacuum–value.[96] We thus conclude that for Mu@C_{60} the spin exchange interaction (J in Eq. (3.3)) in A_3C_{60} is small and the perturbation approach (Eq. (3.6)) is valid.

Knowledge of how $g_N(0)$, the density of states at the Fermi surface, varies as a function of the lattice constant a, can be used to compare the observed dependence of $T_c(a)$ with the result from the McMillan equation (Eq. (1.9)). Such tests of the McMillan equation are important in establishing, for example, the nature of the superconducting pairing mechanism. Furthermore, there is considerable interest in the the role of orientational disorder in determining electronic properties such as $g_N(0)$.[177, 178] In the normal state, both ν_{SE} and $(T_1T)^{-1}$ are proportional to the squared density of states at the Fermi surface $g_N^2(0)$ (e.g. Eq. (3.7)), so the ratios defined above provide a measure of $g_N(0)$ relative to its value in Rb$_3$C$_{60}$. For comparison, similar ratios from NMR[180, 181, 103, 182] yield $\rho^x > 0.75$ for both x = K$_3$C$_{60}$ and Na$_2$CsC$_{60}$. The low value of our ratios for Na$_2$CsC$_{60}$ *may* indicate that the proportionality constants (hyperfine couplings) between ν_{SE} (or $(T_1T)^{-1}$) and $g_N^2(0)$ may vary with structure. This is not unreasonable, since

the couplings depend on the detailed structure of the electronic orbitals constituting the conduction band, such as the degree of sp hybridization. It is known that the C-C bond lengths of C_{60}^{-3} in cubic Na_2CsC_{60} differ slightly[43] from those of the neutral C_{60}, but similar measurments on the orientationally disordered systems have not been reported. The exchange coupling for Mu@C_{60} (J in Eq. (3.3)) may be more sensitive to such differences than those of ^{13}C NMR because they are determined by the tails of the carbon orbitals protruding into the ball; whereas, the NMR constants are determined by the behaviour of the orbitals at or near the ^{13}C nucleus. While the electron–phonon enhancement of g_N (which may differ between the Pa$\bar{3}$ and Fm$\bar{3}$m structures) does not[179] affect T_1, electron–electron interactions can[102], via for example, Stoner enhancement[1] of $g_N(0)$. If there are short–wavelength electronic correlations, it is possible that $T_1(T)$ might vary within the unit cell, causing the Mu@C_{60} and ^{13}C to vary differently. The similarity of the temperature dependence of $(T_1T)^{-1}$ for alkali and ^{13}C NMR, though, suggests that any electronic correlation contribution to T_1 does not vary significantly with position in the unit cell in either Fm$\bar{3}$m[180] and Pa$\bar{3}$[181] materials. Even if the hyperfine couplings and $g_N(0)$ were identical, it is possible[183] that different levels of disorder could lead to different values of T_1. Thus we conclude that simple comparison of the magnitudes of T_1 (from μSR or NMR) between non–isostructural A_3C_{60} superconductors may not represent a comparison of $g_N(0)$. The possibility that C_{60} polymerization is the source of suppression of the normal state $(T_1T)^{-1}$ in Na_2CsC_{60} is discussed in §4.3.

If the T_1 relaxation is *too slow* to be observed, the amplitude of the signal due to Mu, which is field dependent below $\sim 0.5T$, can still be used to identify Mu. The field

---

[1]Stoner enhancement of the electronic density of states is due to ferromagnetic correlations. In the Stoner theory, the enhanced density of states is $\bar{g}_N(0) = g_N(0)/(1 - Ig_N(0))$, where I is an exchange energy, see §4.2.2 of reference [69] for further details.

dependence follows:

$$A_{Mu}(B) = A \frac{1 + 2x^2}{2(1 + x^2)}, \tag{4.4}$$

where x is the reduced field B/B_{hyp}, and B_{hyp} is defined as $A_\mu/(\gamma_e + \gamma_\mu)$ (see §7.3.1 of Schenck[75]). Measurement of this field dependence, when the Mu asymmetry is non–relaxing, requires careful accounting of the systematic field dependent shifts of the LF–μSR baseline. This method has the advantage that it admits the possibility of measuring the hyperfine parameter (although not as accurately as precession would) which determines, for example, the inflection point of the decoupling curve (Eq. (4.4)). We have made two measurements of the LF muonium decoupling curve in two different samples of $Rb_3 C_{60}$. In the first measurement, we acquired pairs of spectra at 35K and 4K at each field in the separate spectra apparatus (see §2.1.3) which allowed collection of a reference spectrum in high purity silver in the same conditions of field and temperature *simultaneously*. Systematic shifts in the baseline could thus be at least partially compensated using the reference data. In the second experiment, we took data in various fields at 2 (or more) temperatures, one where the relaxation was quite fast, and one where it was slow in order to determine the relaxing amplitude, i.e. the muonium asymmetry A_{Mu} (see Fig. 4.15). The results of this second method are roughly consistent with the first measurement but less scattered. The decoupling in the data is apparently sharper than expected (fit curve). In this data, we did *not* field cool, but the consequent additional inhomogeneity of the field would not affect the decoupling significantly. Any correlation of the amplitude and relaxation rate, due for example to a non–exponential relaxation, could bias the extracted asymmetry and account for the sharper feature. From the fit to Eq. (4.4), we get $A_\mu = 4300(400)$MHz. We turn now to briefly discuss the stability of $Mu@C_{60}$ in $Rb_3 C_{60}$.

In semiconductors, Mu centres may undergo spin–exchange with thermally excited

free carriers. Furthermore, at sufficiently high temperature, Mu can also undergo a series of charge cycling transitions, such as

$$Mu^0 \leftrightarrow Mu^+ + e^-, \quad \text{or} \tag{4.5}$$

$$Mu^0 + e^- \leftrightarrow Mu^-. \tag{4.6}$$
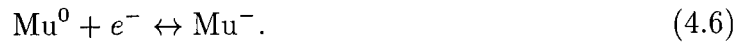
Spin–exchange and ionization cycling lead to very similar spin relaxation behaviour of the muon. In particular, as the temperature is raised, and ionization begins to occur, there is a rapid increase in the LF relaxation rate. We have observed such an increase of the T_1 relaxation rate of $Mu@C_{60}$ in Rb_3C_{60} at 4.2T (see Fig. 4.16) which we attribute to charge exchange cycling of Mu. From the temperature dependence, the activation energy is on the order of 600K. The apparent stability of paramagnetic $Mu@C_{60}$ in Rb_3C_{60} at low temperature is strong evidence that the Mu impurity level lies in the band gap (see Fig. 4.17), and that the ionized Mu^- state lies above the Fermi level. This is reasonable considering the Coulomb repulsion between the two local electrons on the Mu^- confined in the C_{60} cage. If this picture is correct, it suggests that the 600K energy scale represents the energy of the Mu^- state above the Fermi level. Thus the Mu^- may be a short–lived resonant state which dissociates quickly into Mu^0 and an electron which is released into the conduction band.

In conclusion we note that the important features of the muon sites in the A_3C_{60} superconductors to the analysis included in the following sections are simply that the muons stop randomly on the relevant length scales of the vortex state: the penetration depth λ and the vortex spacing; most of the muons remain diamagnetic and sample the field distribution of the vortex state randomly; and a small fraction of the muons form a paramagnetic muonium centre inside the C_{60} cage which is only very weakly coupled to the conduction electrons.
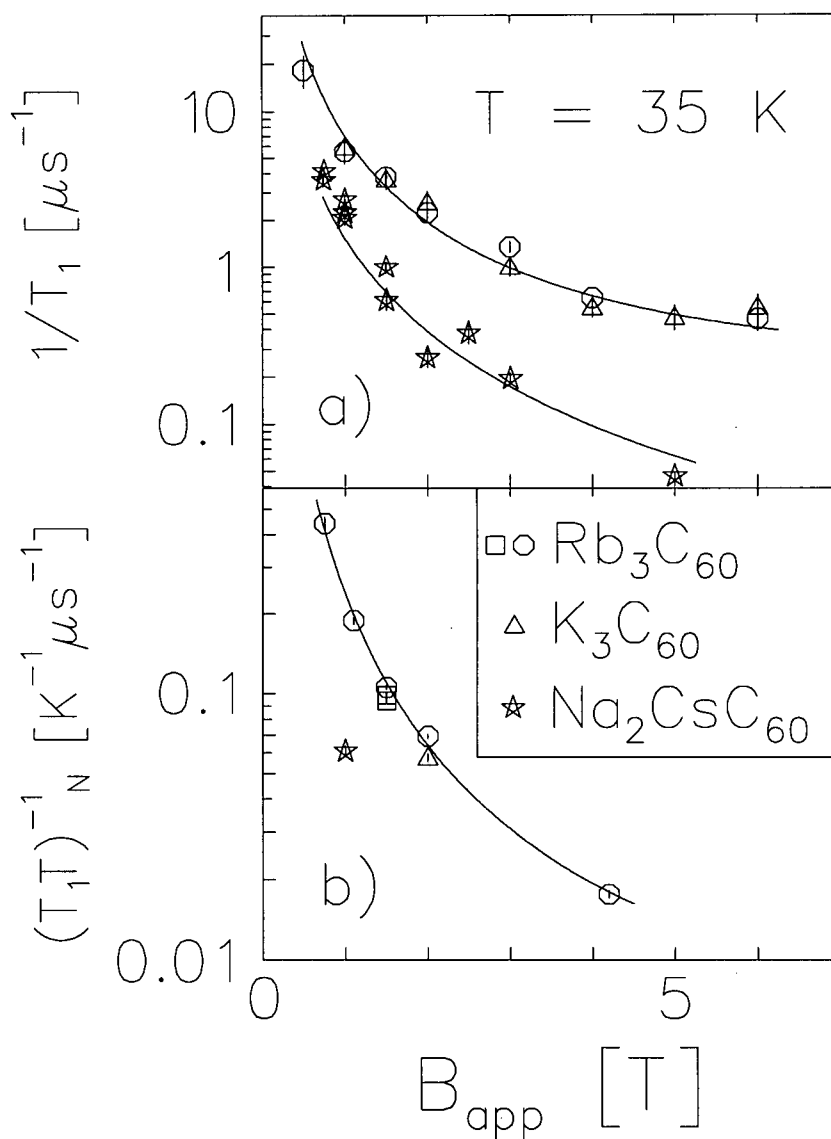
Figure 4.14: *a)* The field dependence of the LF relaxation rates at 35K. The fits to the spin–exchange model are discussed in the text. *b)* The field dependence of the normal state value of $(T_1T)^{-1}$ fit to a similar model.
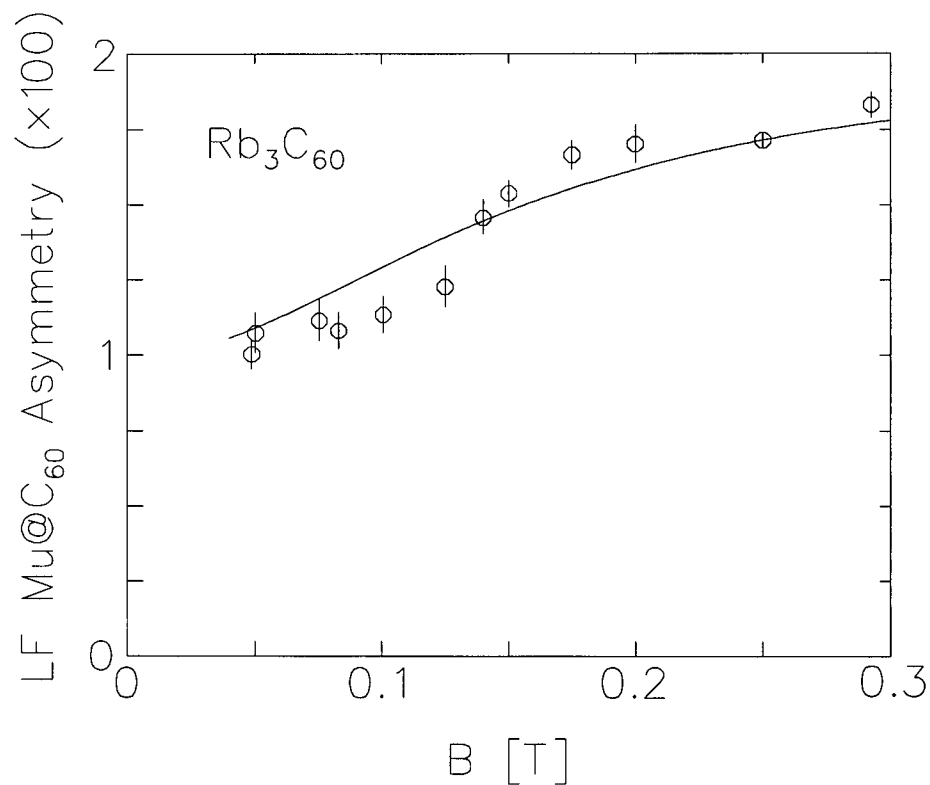
Figure 4.15: The LF dependence of the $Mu@C_{60}$ asymmetry (decoupling curve). The field at the inflection point indicates that the Mu hyperfine parameter is large (near its vacuum value). Each point is determined from a common fit to at least 2 different temperatures, ranging from 2.5 to 15 K (e.g. Fig.4.22).
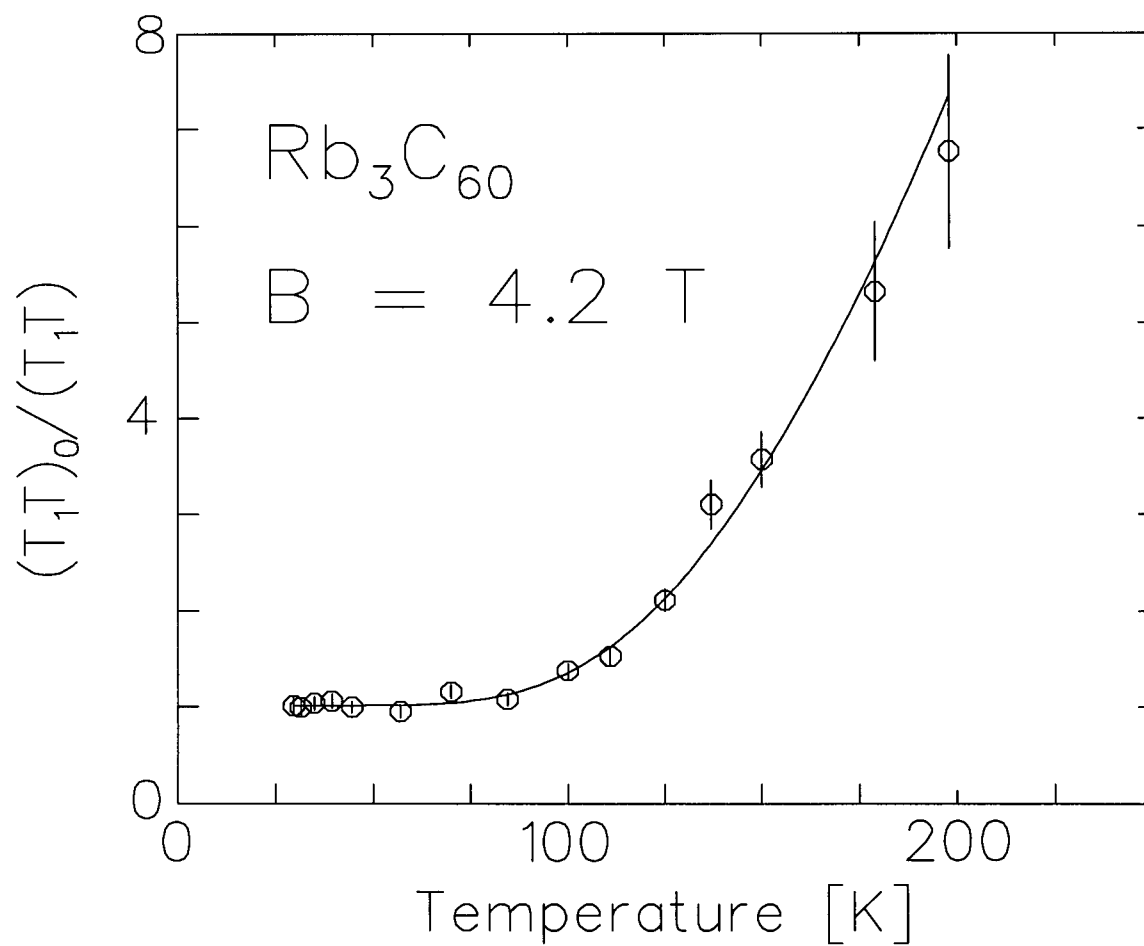
Figure 4.16: Activated increase in $(T_1T)^{-1}$ relative to its value at low temperature likely due to Mu@C_{60} ionizing to endohedral Mu$^-$. The fit curve is $(1.01(3) + 123(35)\exp\left(-588(40)K/T\right))$.
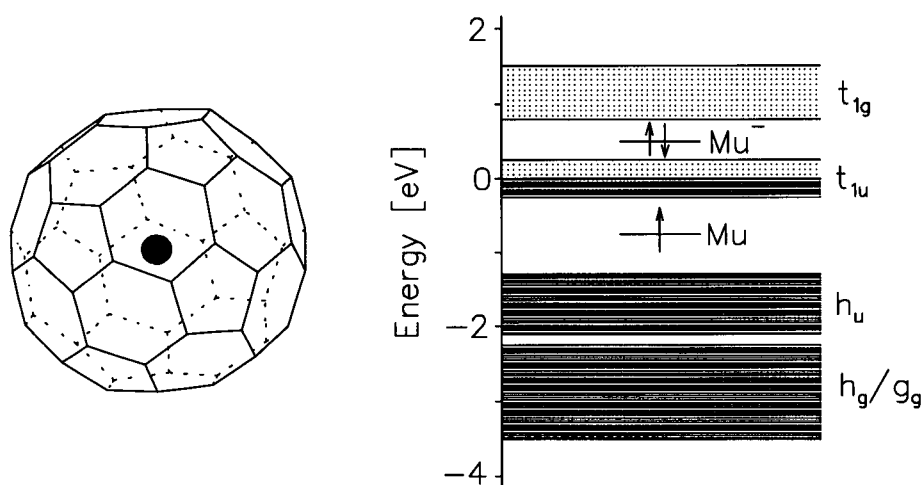
Figure 4.17: Proposed structure of Mu@C_{60}. The Mu atom is in the $1s$ ground state in the centre of the C_{60} cage. A large Coulomb energy is required to bind another electron to form Mu$^-$, so the Mu$^-$ level may lie above the conduction band.

4.2 Transverse Field: The Vortex State Field Distribution

In TF experiments in A_3C_{60} superconductors, it is found[184, 185, 186] that a large fraction of the injected muons remain diamagnetic, and their precession signal is broadened below T_c by the inhomogeneous magnetic field distribution of the vortex state.

The lineshape due to the field distribution of a triangular flux line lattice (FLL) with additional effects due to flux–lattice disorder and anisotropy have been studied in detail in the context of high–T_c superconductors.[187, 188, 189, 190] The characteristic features of this lineshape can be related to the spatial distribution of fields of the triangular FLL: there is a sharp low–field cutoff of the lineshape due to the minimum field that occurs in the centre of the triangle defined by three neighbouring vortices; at slightly higher field, there is a sharp peak due to the highly weighted field corresponding to the saddle point midway between two vortices; and there is a sharp high–field cutoff due to the maximum field occurring in the vortex cores. For an ordered triangular FLL, it is found that the second moment of the field distribution is related to the London penetration depth at intermediate fields by[187]

$$\lambda \approx [3.71 \cdot 10^{-3} \frac{\Phi_0^2}{(\Delta B)^2}]^{1/4}, \tag{4.7}$$

where $\Delta B = \sigma_S(0)/2\pi\gamma_\mu$ is the RMS deviation of the field distribution.

To accurately determine λ for a perfect triangular FLL, involves more detailed modelling of the field distribution. One such model relies on an approximate low–field solution of the Ginzburg–Landau theory[191], which, more recently, has been extended to higher fields[192] and further simplified.[193] This theory results in a field dependent relationship (for $B \ll B_{c2}$),

$$\lambda \approx [3.71 \cdot 10^{-3} \frac{\Phi_0^2 f_v^2(B/B_{c2})}{(\Delta B)^2}]^{1/4}, \tag{4.8}$$

where f_v is a universal function of order unity (but sharply field dependent) at low reduced

fields. λ estimated from Eq. (4.8), for $B/B_{c2} \approx 0.02$, will be $\sim 15\%$ smaller than that of Eq. (4.7). Estimates of λ can be improved by fitting a model of the asymmetric field distribution, rather than just using the second moment.[194, 190] If the fractional volume of the FLL corresponding to the vortex cores is large enough, the high–field cutoff will be observable, and the superconducting coherence length ξ can be measured.[195, 196]

It would be surprising to find the flux adopting a perfect triangular FLL in powdered superconductors, such as these[2] , where both the vortex separation and λ are on the same scale as ξ_{XTL}, the coherence length of crystalline order. One would instead expect that the flux lines would exhibit no long–range order.[141] Furthermore, if the crystallite size is such that the volume fraction of the sample that is within a penetration depth of the surface is significant, the field distribution will differ from that of an infinite (ordered or disordered) FLL.[3] A disordered FLL would possess a field distribution smeared relative to the perfect FLL. Such smearing would make a significant contribution to the second moment of the field distribution, e.g. see[189], making the applicability of the above theories questionable. This is just the situation we find in A_3C_{60} (see, for example, Fig. 4.18a). The line is much broader than in the normal state but exhibits only a slight asymmetry. It is unreasonable to attempt to fit such a smeared lineshape to the full theoretical shape, but Fig. 4.18b shows two simulated lineshapes for comparison. We note that the fluxoid distribution is *not* melted and only weakly pinned at 3K and 1T, because, for example, shifting the applied field at this temperature causes the line to shift in frequency, but broaden significantly (Fig. 4.20). This is in contrast to crystalline $YBa_2Cu_3O_{6.95}$, where[194] shifting the field shifts only the background signal as the FLL is strongly pinned, and to the vortex liquid state, where the (symmetric) line simply shifts without altering shape.

---

[2]Characterization of these samples from other techniques can be found in §2.3.

[3]Note that the crystallite size and ξ_{XTL} are different. ξ_{XTL} is (roughly) the distance between defects of the crystal, such as dislocations, while the crystallite size is the distance between free surfaces.

Clearly, the 1100Å value of the penetration depth deduced from magnetization measurements is inconsistent with the observed lineshape, since no amount of disorder will narrow the line, and estimates of the correlation time for motion of the vortices from NMR[197] strongly suggest that, at low temperatures, there should be no dynamical narrowing of the μSR line. The high–field cutoff in the FLL field distribution will move down towards the average field as *either* λ or ξ increases. Because of this correlation, the absence of a long high–frequency tail in the observed lineshape (fig 4.18a) constrains only the pairs (λ,ξ), i.e. along the line ($\lambda,$30Å) the observed lineshape is consistent with λ larger than $\approx$ 3000Å with the condition that larger values of λ will require a greater degree of disorder to match the observed linewidth. Such an inconsistency between the magnetization and μSR results is not surprising, since the procedure for obtaining λ from the magnetization is fraught with difficulties[31, 36] of which only some are reduced or eliminated through use of a single crystal instead of powder. We note that other results using NMR[182] and optical[198] methods find λ consistent with the above lower limit.

We extract the second moment from the TF data by fitting the time dependent envelope of the precession signal to a gaussian of the form $A\exp(-(\sigma t/\sqrt{2})^2)$. The results are shown in Fig. 4.19a. In the normal state, the lineshape is a narrow gaussian whose width is determined by the distribution of magnetic fields due to the randomly oriented nuclear dipoles (^{13}C,^{23}Na,^{39,40,41}K,^{85,87}Rb,^{133}Cs, see Tables A.1 and 2.3). This normal state width σ_N is temperature independent in the range between T_c and room temperature (except for Na_2CsC_{60} discussed below) and adds in quadrature to the σ_S due to the disordered FLL to determine the overall σ below T_c. We use this correction to produce σ_S shown in in Fig. 4.19b. The temperature dependences are fit to the phenomenological form $\sigma_S(0)[1 - (T/T_c)^\varpi]$, and the resulting parameters are given in Table 4.5. In spite of the lack of the signature of the FLL in the lineshape, we expect that the overall linewidth is controlled by λ (and much more weakly by ξ) and that

$(\Delta B)^{-1/2}$ will approximately scale with λ. We have calculated the values λ reported in Table 4.5 using the linewidths $\sigma_S(0)$ and Eq. (4.7). Because of the increase of ΔB from disorder of the FLL, this conversion will *underestimate* the actual λ, so this, or perhaps more conservatively the value from the field dependent theory (which we have not included because of uncertainty in the value of B_{c2}), should be considered a *lower bound* for λ. These results can be compared directly with those of references.[184, 185] Note that, at low temperature, $\sigma_S(T)$ is quite flat in contrast to the d–wave linear T dependence seen in clean single crystals of $YBa_2Cu_3O_{6.95}$[199]. In this respect A_3C_{60} superconductors are consistent with s–wave pairing. Such behaviour is not conclusive, however, because in d–wave systems, for example, impurity scattering can lead to[110] a weaker low T dependence of λ. This may be the reason that the $\mu\mathcal{SR}$ linewidth in early measurements on $YBa_2Cu_3O_{6.95}$ powders did not exhibit the linear low temperature behaviour (e.g. [188]).

In Rb_3C_{60}, there is no apparent field dependence to $\sigma_S(T)$ between 0.5T and 1.5T, so the applicability of Eq. (4.8) is questionable. Furthermore, there is large sample dependence of σ_S in Rb_3C_{60} suggesting a strong effect of disorder on λ. In the dirty limit $\xi \approx l$, where l is the electron mean free path. The penetration depth varies strongly with l via

$$\lambda^{-2} \propto \frac{n_s}{m^*} \left[\frac{1}{1 + \xi/l} \right], \tag{4.9}$$

where n_s is the superelectron density and m^* is the effective mass. Thus if $l \leq \xi$, any sample dependent disorder that contributes to l could alter λ strongly, as in the observed sample dependence in Rb_3C_{60}. The low T dependence of σ_S has been fit to the BCS activated form[112] for the clean–limit[186]; however, the dirty–limit form is probably appropriate to Rb_3C_{60} and K_3C_{60} (but possibly not to Na_2CsC_{60}). In this case[111], for

$T < 0.5 T_c$,

$$\sigma_S \approx \sigma_{S0}[1 + e^{-\Delta_0/kT}]^{-2}, \tag{4.10}$$

where Δ_0 is the low temperature BCS gap parameter. The results of these fits are also given in Table 4.5. We note that some caution must be taken regarding the interpretation of the TF results for Na_2CsC_{60} because: i) the applied field was very low (not far from H_{c1}) and ii) σ_N was rather large and temperature dependent above 50K (Fig. 4.21). The behaviour of $\sigma_N(T)$ may be associated with molecular dynamics but may also be due to muons stopping in unmasked areas of the Al sample cell. However, the consistency of the observed σ_S with another published measurement[185] at higher field suggests that neither of these effects was appreciable. Furthermore, the Al signal will have no contribution to the signal in high LF discussed in the following section.

	Rb_3C_{60}-1	Rb_3C_{60}-2	K_3C_{60}	Na_2CsC_{60}
B_{TF} [T]	1.0	0.27	1.0	0.01
$\sigma_N/\sqrt{2}[\mu s^{-1}]$	0.076(1)	0.093(1)	0.087(1)	0.133(1)
$\sigma_S(0)/\sqrt{2}[\mu s^{-1}]$	0.4315(10)	0.2068(10)	0.2570(20)	0.0769(10)
T_c [K]	29.3(8)	28.9(2)	18.6(2)	11.3(3)
ϖ	2.93(4)	3.36(8)	2.83(9)	7.5(1.0)
ΔB[mT]	0.717	0.343	0.427	0.128
λ[Å]	4200	6100	5400	9900
Δ_0/kT_c	1.37(5)	1.56(5)	1.39(6)	–

Table 4.5: Parameters of the TF linewidth fits described in the text and shown in Fig. 4.19. ΔB is the RMS width of the field distribution. Δ_0/kT_c is obtained from fits to Eq. (4.10) and the T_c values in the Table.

The historic evolution of μSR measurements of λ in $YBa_2Cu_3O_{6.95}$ may provide a guide for the robustness of estimates of λ from the second moment of the μSR lineshape. Despite the more serious consequences of powder averaging in these highly anisotropic

systems, the extracted penetration depth from μSR data (even from symmetric line-shapes, like Fig. 4.18a) has exhibited a variation of only $\sim$30% (including model as well as sample variation). Thus the most serious uncertainty with our determination of λ may be the strong sample dependence. The observation of the asymmetric lineshape characteristic of a triangular FLL would certainly make our conclusions much stronger, and such lineshapes are expected in single crystals which can now be made in sufficient size[94] for such an experiment.

We turn now to the temperature dependence of the LF (T_1) relaxation of Mu@C$_{60}$, noting that the interstitial diamagnetic muons will not contribute to this signal (except near ZF, where nuclear dipolar fields can cause depolarization of the diamagnetic muons).
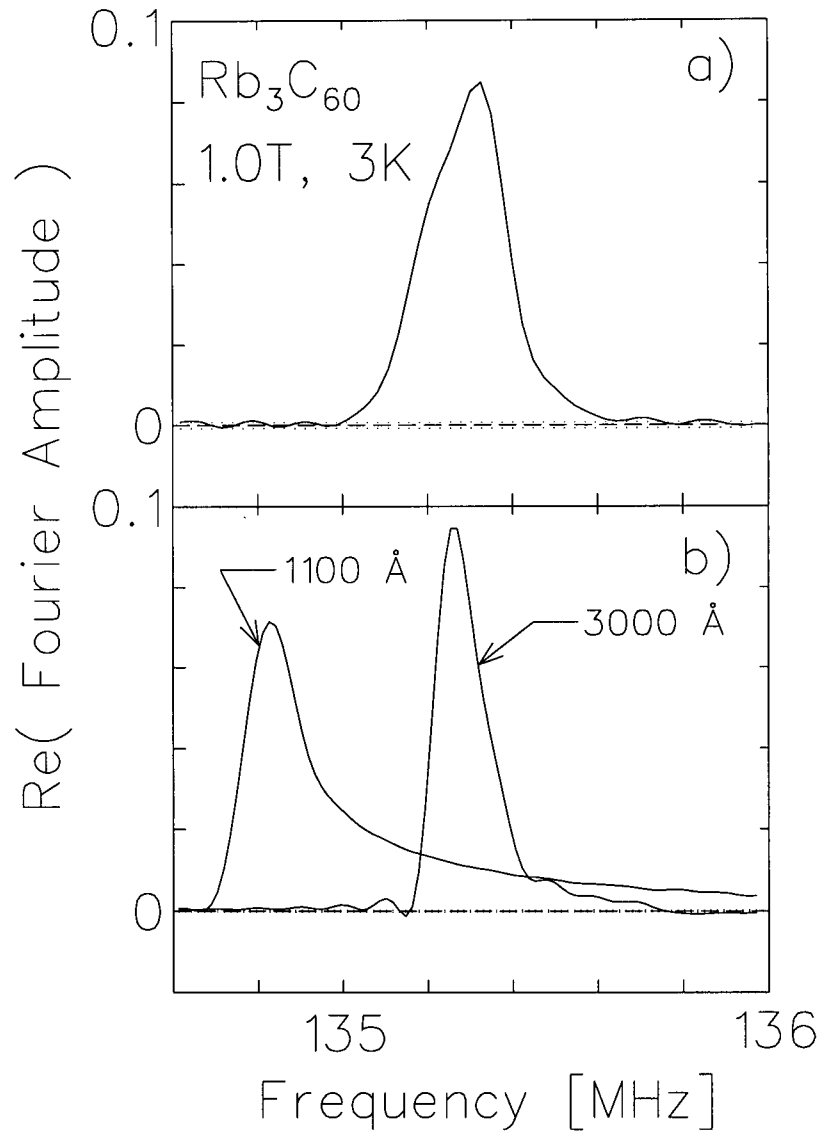
Figure 4.18: *a)* A high statistics μSR lineshape (FFT of TF asymmetry spectrum) in
Rb_3C_{60} field–cooled to 3K at 1.0T applied transverse field. *b)* Simulated lineshapes
for a perfectly ordered triangular flux–lattice using the Ginzburg–Landau theory.[191,
192, 193] The simulation parameters (λ, ξ) are (3000Å,30Å) and (1100Å,30Å). The field
distributions are convoluted with a Gaussian corresponding to the normal state linewidth.
The 3000Å simulation also includes a small non–relaxing background signal known to
exist in the data.
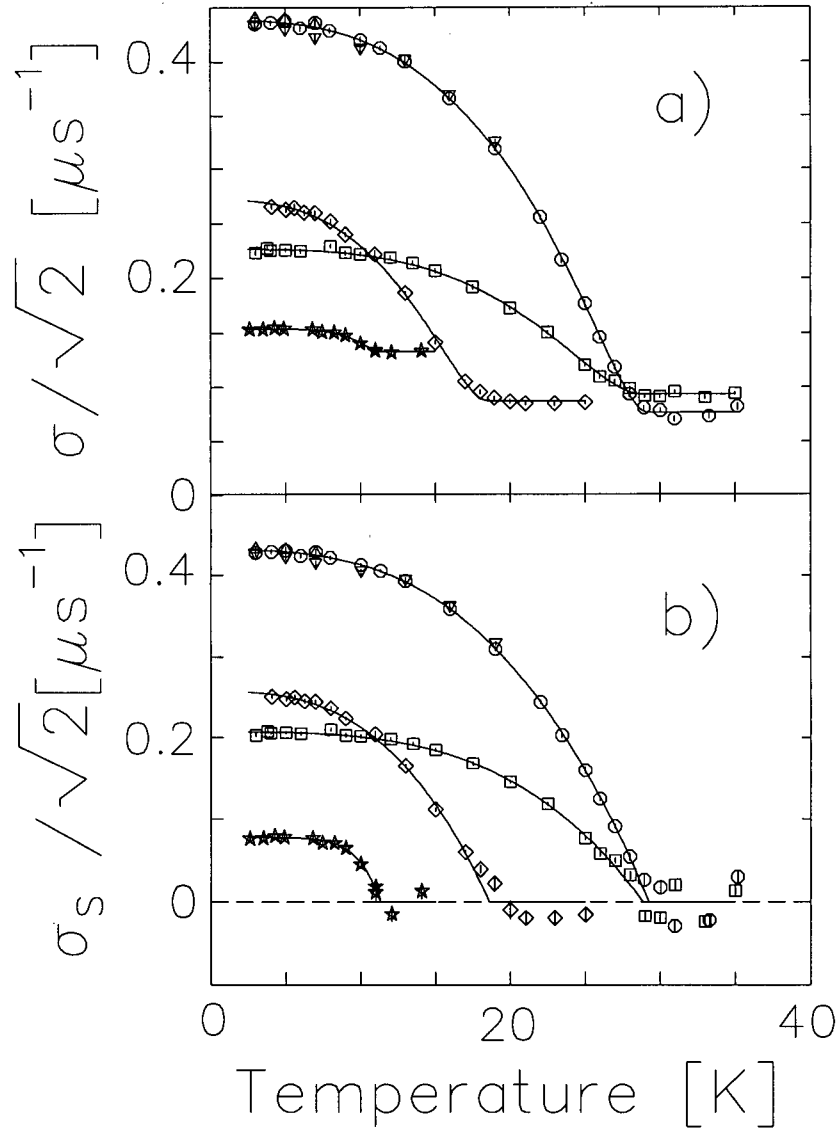
Figure 4.19: *a)* Second moments of the μSR lineshape as a function of temperature in *stars* Na_2CsC_{60} (0.01T), *diamonds* K_3C_{60} (1.0T), Rb_3C_{60} (*circles* 1.0T, *triangles* 0.5T, *nablas* 1.5T), and *squares* a second sample of Rb_3C_{60} (0.27T). *b)* Second moments corrected for the normal state values, see Table 4.5
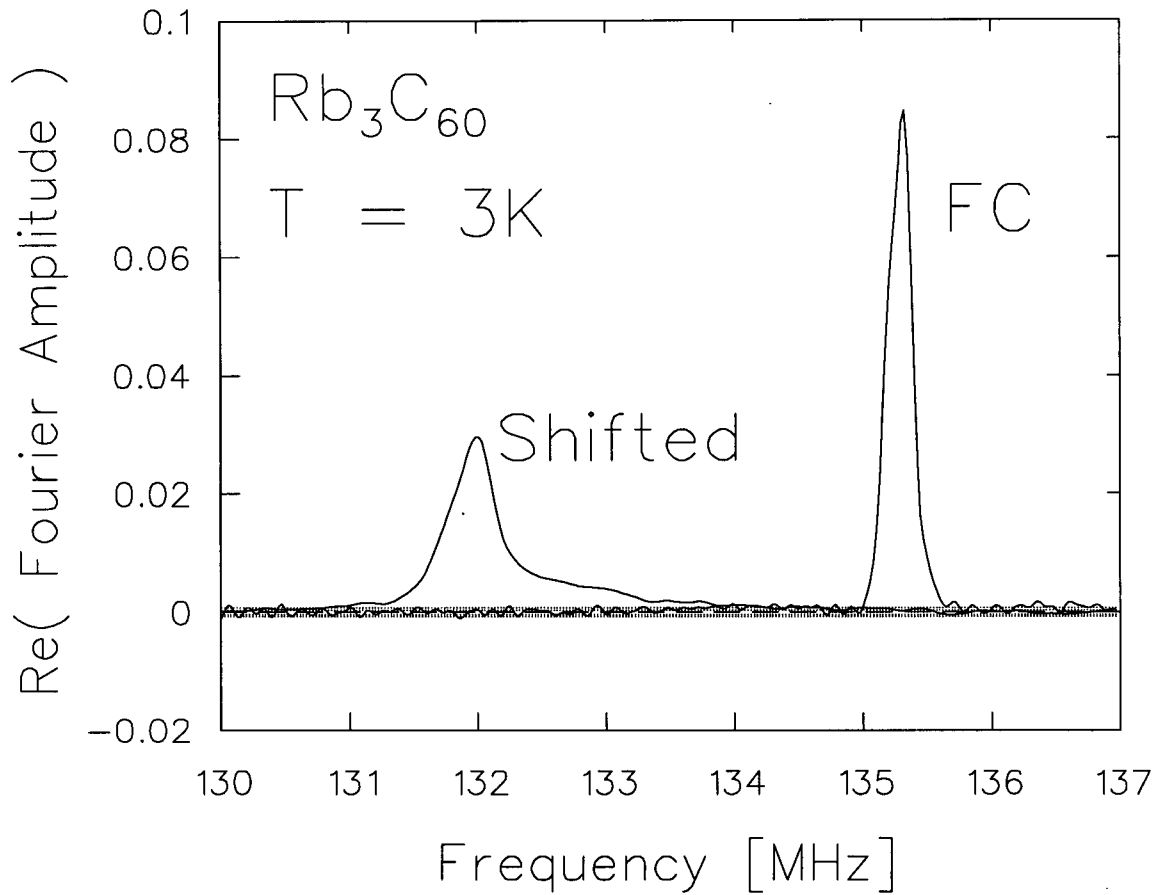
Figure 4.20: Comparison of the field–cooled (FC) lineshape with the shifted lineshape. The FC shape is the same as that shown in Fig. 4.18a. Immediately after the FC data was taken. The field was shifted down from 1T by about 0.025T at 3K in order to obtain the shifted data. The effect of shifting the field at low temperature indicates that the flux at this field is pinned (since the line broadens, unlike a vortex liquid) but not very strongly (since it shifts, unlike the case of single crystal YBCO [194]). The resemblance of the shifted lineshape to a lower λ vortex lattice lineshape (e.g. Fig. 4.18b) is purely coincidental. The shifted lineshape is dominated by disorder effects from the non–equilibrium field distribution.
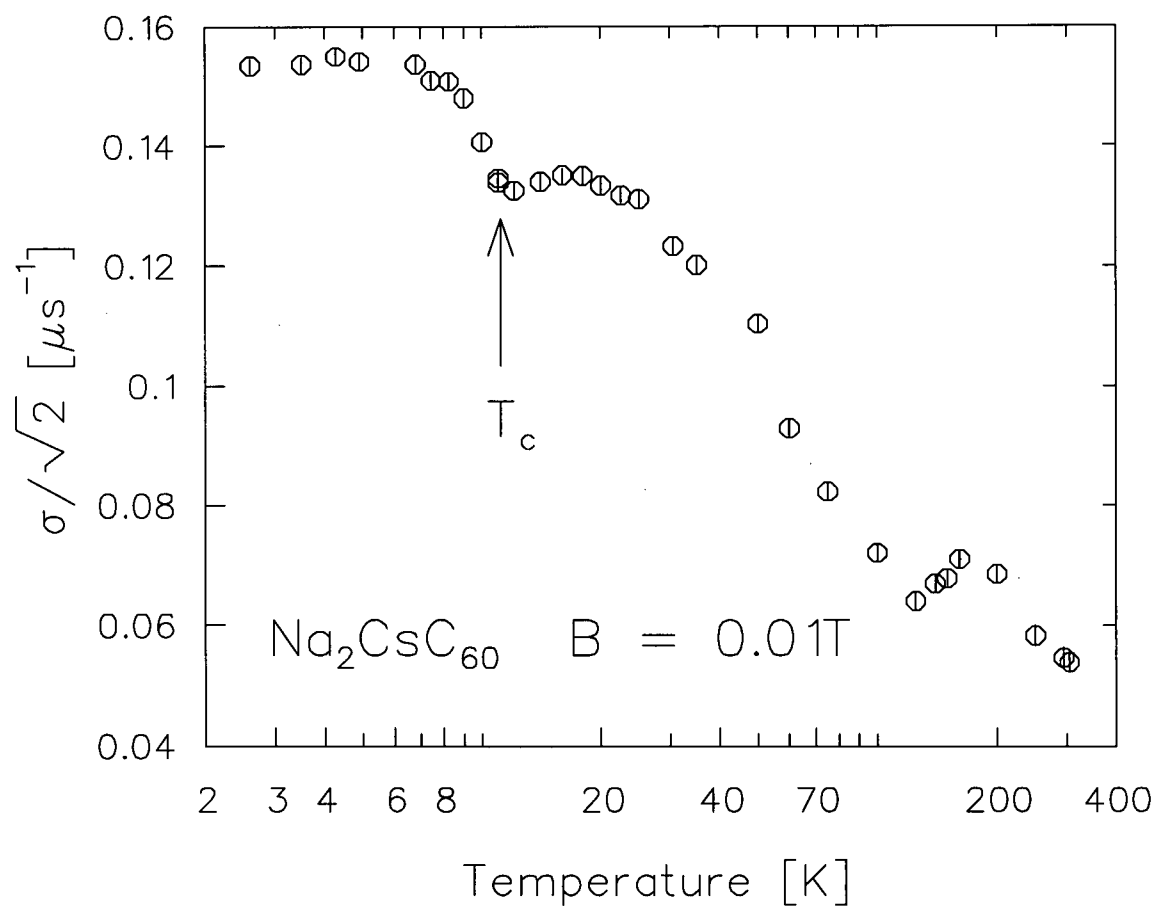
Figure 4.21: The temperature dependence of the TF $\mu S R$ linewidth in a field of 10mT. The superconducting transition can be seen at about 11K. The temperature dependence above T_c may be the result of molecular dynamics or partial polymerization.

4.3 Longitudinal Field: T_1 Relaxation of Mu@C_{60}
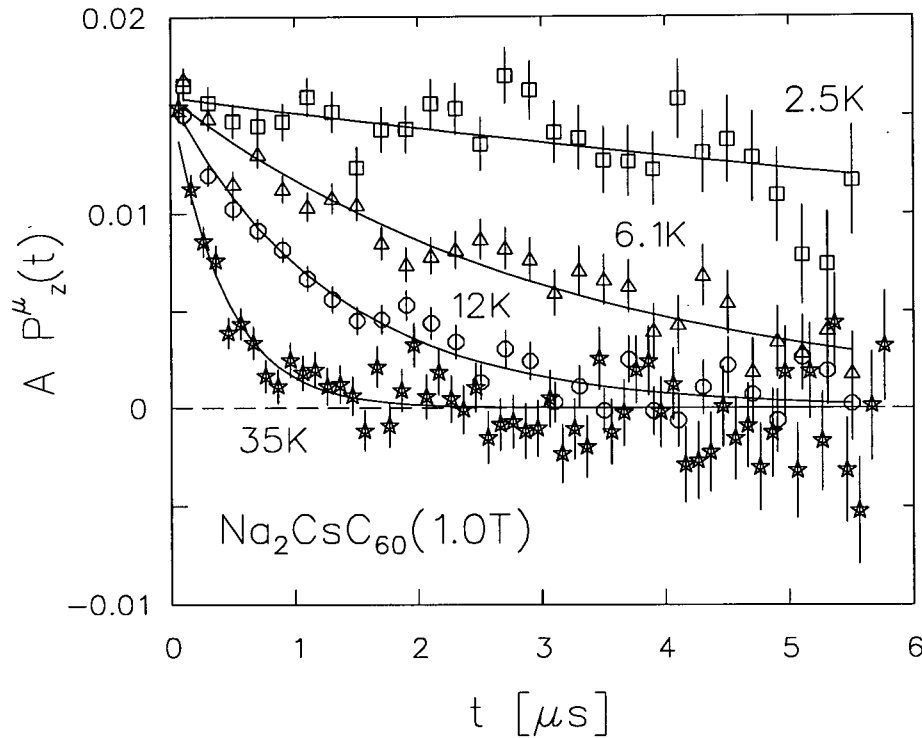
Figure 4.22: Single exponential relaxation of Mu@C_{60} in a longitudinal applied field of 1.0 T. The fits shown are to a common amplitude exponential relaxation.

The relaxation of Mu@C_{60} in high LF ($B \geq 0.75T$) is found to be single exponential, e.g. Fig. 4.22. The relaxation rates exhibit essentially temperature independent $(T_1 T)^{-1}$ behaviour between about 50K and T_c for each of the systems, Rb$_3$C$_{60}$, K$_3$C$_{60}$, and Na$_2$CsC$_{60}$. In Rb$_3$C$_{60}$ we find no sample dependence, but in Na$_2$CsC$_{60}$ we find a significant difference between two runs on the same sample which we infer to be a quench–rate dependence. We thus postpone discussion of the temperature dependence in Na$_2$CsC$_{60}$ to §4.3.2.

4.3.1 $T_1(T)$ in Rb_3C_{60} and K_3C_{60}

The average normal state values of $(T_1T)^{-1}$ are shown in Fig. 4.14b. At higher temperature there are deviations (Fig. 4.16), but at low temperature, we have no significant evidence for previously reported[85] weakly non–Korringa behaviour. Just below T_c, for $B \approx 1 - 2T$, we find a slightly enhanced $(T_1T)^{-1}$ followed by an strong fall–off below about $0.75T_c$, e.g. Fig. 4.23.
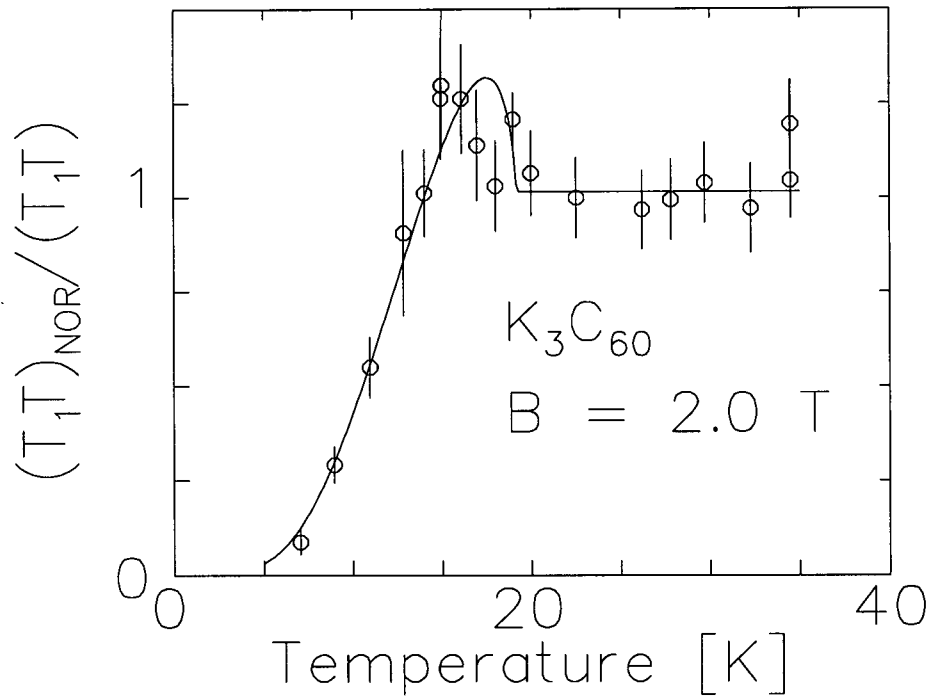
Figure 4.23: Temperature dependence of the spin relaxation rate of $Mu@C_{60}$ in K_3C_{60} at a field of 2.0 T. The fit is to the Hebel–Slichter integral Eq. (3.9) with a broadened DOS of the form Eq. (3.12).

We find that increasing the disorder in the FLL in Rb_3C_{60} does not affect the height of the $(T_1T)^{-1}$ enhancement (coherence peak) by comparing field–cooled and zero field–cooled $(T_1T)^{-1}$ at the peak temperature, T_P, at 1.5 T. However, we find, in Rb_3C_{60}, that the peak is strongly field–dependent (similar behaviour was independently discovered in

NMR T_1 measurements in Rb_2CsC_{60} by Stenger[180]). It is strongly supressed as the field is increased above about 2T, and is entirely gone by 4.2T (Fig. 4.24). The observed heights of the peaks from fits to a parabola near T_P are shown in Fig. 4.25.

In order to discuss analysis of the peaks in terms of the theory outlined in §3.2, we include some brief remarks about the DOS functions used. First we note g_D and g_{SC} (Eq. (3.12) and Eq. (3.13)) do not depend on the sign of the broadening parameter (Γ or Δ_2), which we take to be positive. The property of conservation of the total number of electron states, which simply results from the construction of the eigenstates of the superconductor from those of the normal state, can be succinctly written,

$$\int_0^\infty [g_S - g_N]dE = 0. \tag{4.11}$$

The BCS g_S follows this, as does the heuristic form g_D; however, the strong coupling form g_{SC} (Eq. (3.13)) does not; in fact,

$$\int_0^\infty [g_{SC} - g_N]dE = -|\Delta_2|, \tag{4.12}$$

i.e. there are effectively fewer states in g_{SC} than in the normal state. Of course, in the full strong–coupling theory, $\Delta = \Delta(E,T)$, g_{SC} will have structure above the gap, and Eq. (4.11) will be obeyed. One consequence of this property of g_{SC}, is that the integral for $(T_1T)^{-1}$ Eq. (3.9) will approach a value less than 1 as T approaches T_c from below. The resulting discontinuity scales with Δ_2, and is negligible for small Δ_2. However, if g_{SC} is used to model the small coherence peaks reported here, Δ_2 is relatively large, and the discontinuity is significant, so that the approximation first introduced by Fibich[128], that the energy dependence of Δ_2 can be neglected in calculating the coherence peak seems untenable in the current context, and in order to use strong–coupling results, one would have to resort to more detailed calculations.[131, 123] There is also a significant difference between g_D and g_{SC} in the $E \to 0$ behaviour which is important in determining

the low temperature behaviour of $(T_1T)^{-1}$: $g_D(0) = [1 + (\Delta/\Gamma)^2]^{-1/2}$, while $g_{SC}(E)$ goes to zero with slope $\approx |\Delta_2|/\Delta_1$ as $E \to 0$.

The low field peaks have been fit to Eq. (3.9) using both the DOS functions g_D and g_{SC} (avoiding the discontinuity mentioned above by only considering the data below T_c) with $\Re\{\Delta\} \propto \Delta_{BCS}(T)$, which is still quite a good assumption in the strong–coupling case.[124] We find that, in order to explain such a small height of the coherence peak, the broadening parameters near T_c must be $\Gamma/\Delta_0 \approx \Delta_2/\Delta_0 \approx 10\%$. If the broadening is due to strong electron–phonon scattering, then it should be significantly temperature dependent. For a Debye phonon spectrum, at low temperature, $\Delta_2 \propto T^{7/2}$. The contribution of the low energy libron peak[201] may modify this somewhat; although, the weak electron coupling to this mode[201] will limit its effect. The results of tunneling experiments could, in principle, provide confirmation of the sharpening of g_S at low temperature, but the published spectra are rather equivocal: low temperature break–junction tunneling spectra show rather broad peaks[202] while point–contact spectra are quite sharp[203] and other STM measurements are fairly broad but show a strong dependence on crystallinity.[204] Recent planar junction tunneling measurements[205] confirm the former behaviour, suggesting an intrinsic nearly temperature–independent broadening mechanism for g_S. The width of the coherence peak is controlled by the balance between the peak contribution to the integral Eq. (3.9) and the exponential behaviour due to the opening of the gap; thus, there is significant correlation between the value of Δ_0 and the temperature dependence of the broadening parameter. Generally, a broadening that falls off strongly as the temperature decreases causes the peaks of g_S to sharpen, and the coherence peak to widen; consequently, the value of Δ_0 required to explain the observed peak width will be larger than for a broadening which does not depend as strongly on T.

In high field T_1^{-1} becomes too slow to observe at low reduced temperature, so we use the strong field–dependence (Eq. (3.4) and Fig. 4.14) and study lower temperatures in

a reduced applied field. In this case, over the temperature range $0.5T_c$–$0.25T_c$, $(T_1T)^{-1}$ exhibits activated behaviour as shown in Fig. 4.26. Again the values of Δ_0 required to fit this data depend on what broadening is assumed at low temperature. Because of the Fermi–factor in the integral Eq. (3.9), the low temperature behaviour of $(T_1T)^{-1}$ is determined mainly by the gap and contains no information about the shape of the broadened DOS peaks. However, if there are states within the gap, the temperature dependence may deviate strongly from the activated temperature dependence. We have fit the low temperature data to the same set of models as the peak data at higher field. We have assumed two cases for the temperature dependence of the broadening: strong ($\approx T^{7/2}$) and temperature independent broadening, noting that the real dependence will likely lie somewhere in this range. The results are given in Table 4.6.

In Rb$_3$C$_{60}$ at 0.3T we find at lower temperatures a sample dependent residual relaxation that is much more weakly temperature dependent (Fig.4.27). The source of this residual relaxation could be related to crystalline disorder (in alkali site occupation or degree of orientational disorder) and the finite low T zero–bias conductance observed in tunneling (zero applied magnetic field). There is also evidence that the C$_{60}$ in Fm$\bar{3}$m phases undergo orientational dynamics which freeze out near or below room temperature.[95] Thus, it is possible that the degree of orientational disorder varies with cooling procedure. We have attempted no systematic quench–rate dependences, but there is some evidence that the low T residual relaxation *and* the large sample dependence of λ may be partially due to different cooling procedures. We note that there is no evidence in the Fm$\bar{3}$m materials for a low T polymerized phase, which occurs only for intercalated C$_{60}$ materials with smaller cubic lattice parameters such as Na$_2$AC$_{60}$. The superconducting transition in K$_3$C$_{60}$ is extremely sensitive to radiation damage induced disorder[206]. Such behaviour may[206] be a consequence of the narrowness conduction

band. If this is the case, then variation of quenched disorder may also have an unusu-
ally large effect. At finite field another source of relaxation could be the vortex cores
(§3.2.4). The relaxation rate of the small fast relaxing component is roughly that of the
(extrapolated) normal material, but the amplitude is too large for the small ($\xi = 30\text{Å}$)
cores. Moreover, it does not appear to change linearly in amplitude with field near 0.3T
(see §3.2.4). On the other hand, the linear field dependence would be rather difficult to
observe because of the intrinsic field dependence of the relaxation rate and the extremely
small amplitude. The persistence of some relaxation at low temperature in zero applied
field (inset, Fig.4.28) suggests that at least some of this residual relaxation is not due to
vortices. The relaxation in zero field, however, can have contributions from both static
and dynamic fields.

Data Set(B_{app} [T])	I	II	III	IV
Rb_3C_{60}-1(1.5)	–	–	3.8	4.6–4.8
Rb_3C_{60}-2(1.5)	–	–	3.2	4.0–4.2
K_3C_{60}(2.0)	–	–	3.6	4.4
Na_2CsC_{60}(1.0)	–	–	3.8*	4.0*
Rb_3C_{60}-1(0.3)	2.7	3.1	3.2–3.8	3.6–3.8
Rb_3C_{60}-2(0.3)	2.4	2.7	2.8–3.2	3.0–3.2
K_3C_{60}(0.3)	2.7	3.0	3.2–4.0	3.2–3.6
Na_2CsC_{60}(0.3)	1.1	1.5	–	3.0–3.2*

Table 4.6: The energy gap parameter $2\Delta_0/kT_c$ determined from fitting the temperature
dependence of the Mu@C_{60} to the models: I) $\exp(-\Delta_0/kT)$, II) $T^{-1/2}\exp(-\Delta_0/kT)$, III)
Eq. (3.9) with temperature independent broadening, and IV) Eq. (3.9) with strongly
temperature dependent broadening. * refers to fits in Na_2CsC_{60} where a free temperature
independent $(T_1T)^{-1}$ was included in the fit.

We now move on to discuss of the origin of the observed features of the coherence
peak in A_3C_{60}. The suppression of the peak, relative to its size in e.g. aluminum, can be
due to any of the mechanisms discussed in §3.2.3 or a combination of these mechanisms.[4]

---

[4]The small size of the coherence peak is not the result of the perturbing influence of the paramagnetic

Recent tunneling measurements suggest that we should expect some broadening from strong–coupling effects. There should be at most a *small* amount of anisotropy (large anisotropy is not appropriate to explain either the low temperature behaviour of the TF linewidth σ or $(T_1T)^{-1}$). Also, because the Fm3m materials are likely in the extreme dirty limit ($l < \xi$), any anisotropy would be eliminated by electron scattering.[109] However, the strong field dependence of the coherence peak is not accounted for explicitly by either of these mechanisms, so the effect of magnetic field (see §3.2.4) must be considered. The observed suppression of the peak by magnetic field occurs in a very different part of the phase diagram than regions (i) and (ii) of Fig. 3.12, where it is certainly expected, so that the gaplessness due to proximity to H_{c2} does not account for the observed damping. However, note that some H_{c2} measurements by magnetization exhibit unusual temperature dependence[36] near $T_c(0)$ (Fig. 4.29). Our measurements of $T_c(H)$ via TF μSR (Table 4.5), though, are consistent with a strongly T dependent H_{c2} near $T_c(0)$, see points in Fig. 4.29. The strong linear T dependence of curve A was used to estimate $T_c(4.2T) \approx 28.4K$ shown in Fig. 4.24b. The effects of Pauli pair–breaking on the coherence peak will also be small because, as the Yosida function behaviour of the NMR Knight shift[102] shows, spin–orbit scattering is very weak in these materials. The crude model used to explain the field dependence of the NMR coherence peak[102] (i.e. Eq. (3.17)) does not satisfactorily explain the damping observed in μSR or NMR. For example, in Fig. 4.24a at 20K, the value of $(T_1T)^{-1}$ is near its value in the normal state, so no weighted average of $(T_1T)^{-1}$ with its normal state value will give the observed value at roughly the same reduced temperature at 4.2T of $\sim 0.6 \ (T_1T)_N^{-1}$. Furthermore, this model (which treats the vortices as normal cylinders) is expected to apply[149] only

---

Mu atom. While it has recently been shown[207] that single paramagnetic atoms locally perturb the surrounding superconductor, the Mu (as shown in §4.1) is only very weakly coupled to the conduction electrons. The strong evidence that the Mu perturbation is small is the agreement of the temperature dependence of $(T_1T)^{-1}$ with subsequent NMR experiments[102].

when $B \ll B_{c2}$. The observed strong suppression of the coherence peak occurs in the non–linear region of the phase diagram and may be explained by the theories.[150, 153] The detailed mechanism for this suppression could be elucidated by STM measurements which can resolve both the spatial and energy dependences of the superconducting DOS.
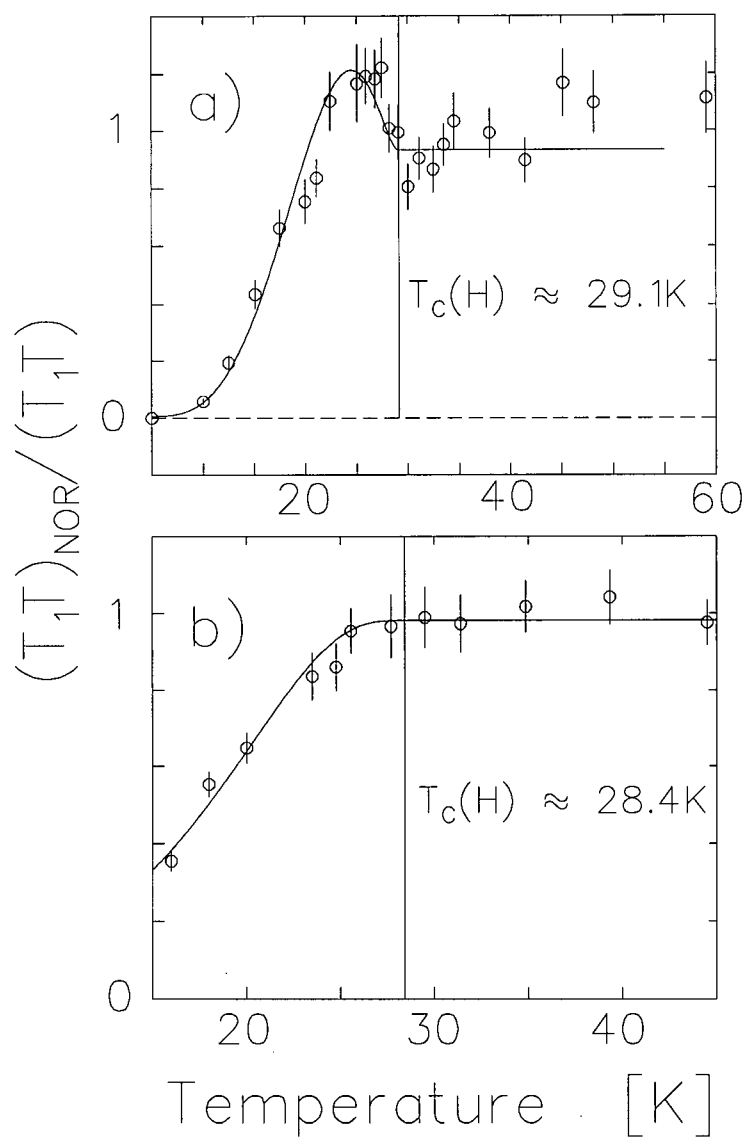
Figure 4.24: Magnetic field damping of the Hebel–Slichter peak in Rb_3C_{60}, note the different temperature scales. The longitudinal fields are *a)* 1.5 T and *b)* 4.2 T.
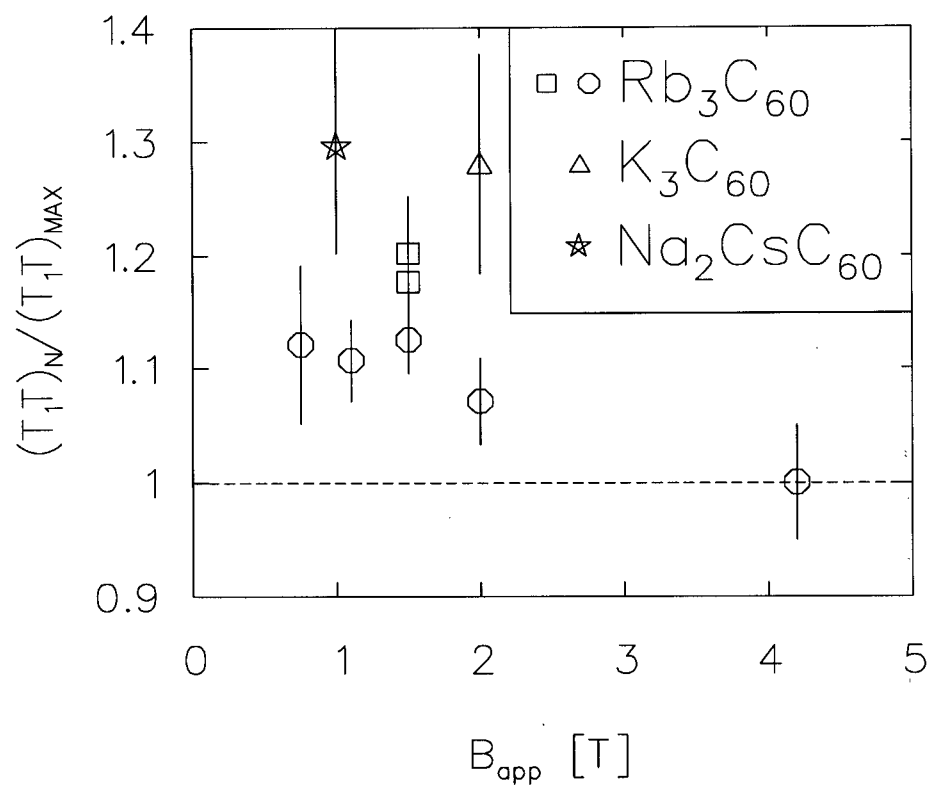
Figure 4.25: Heights of the coherence peak above the normal state as a function of field. These values were obtained from fits to a parabola near the maximum.
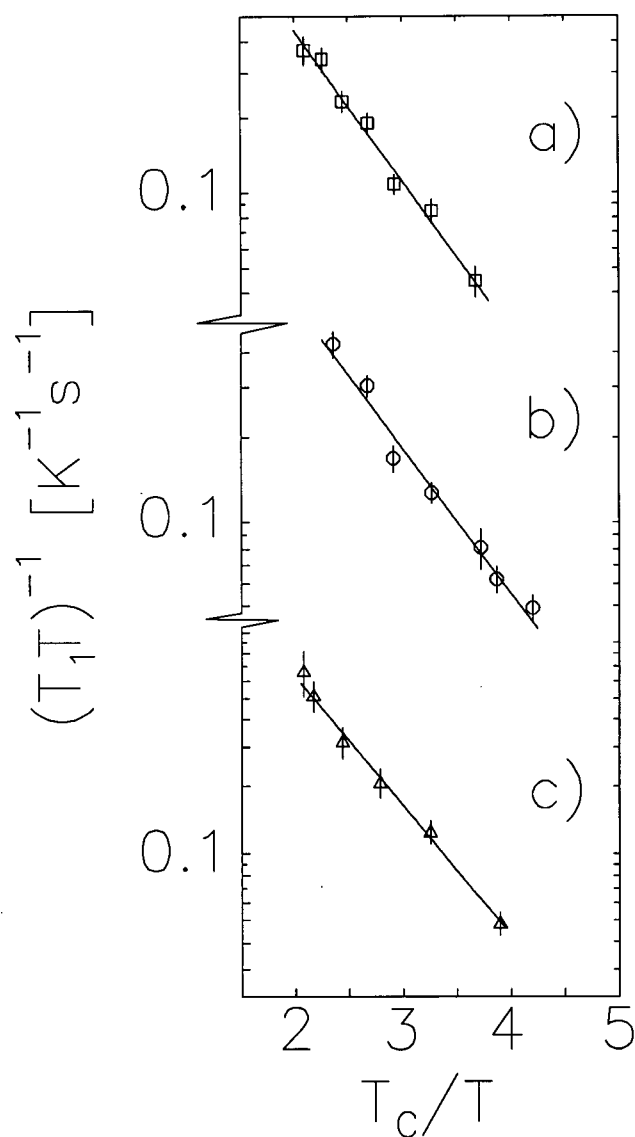
Figure 4.26: The temperature dependence of $(T_1T)^{-1}$ at 0.3T at low reduced temperature. *a)* and *b)* two samples of Rb_3C_{60}, and *c)* K_3C_{60}. This behaviour corresponds to the region labelled "Arr" in Fig. 3.12.
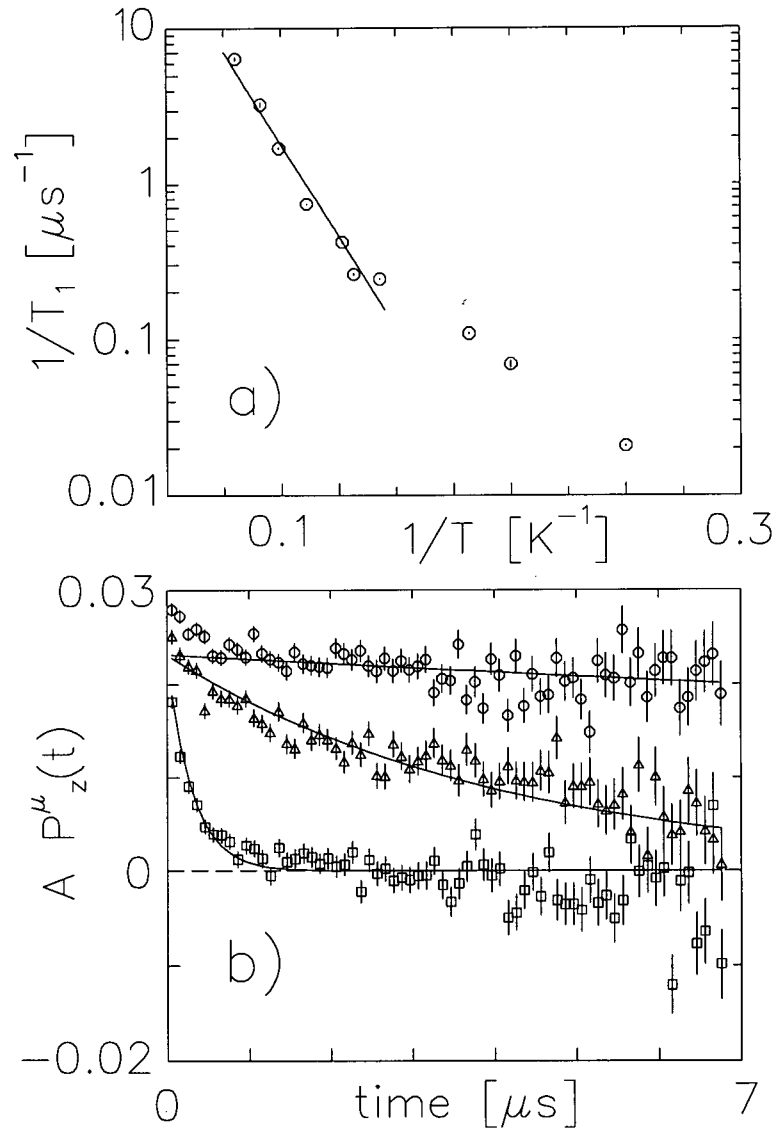
Figure 4.27: Residual relaxation at low temperature in Rb_3C_{60}. At low temperature, the relaxation deviates from the Arrhenius dependence. This behaviour is connected with either region "O" or "2C" of Fig. 3.12. The lack of field dependence and other evidence suggests that this residual relaxation may originate in crystalline disorder (rather than the vortex cores), i.e. region "O" and not "2C".
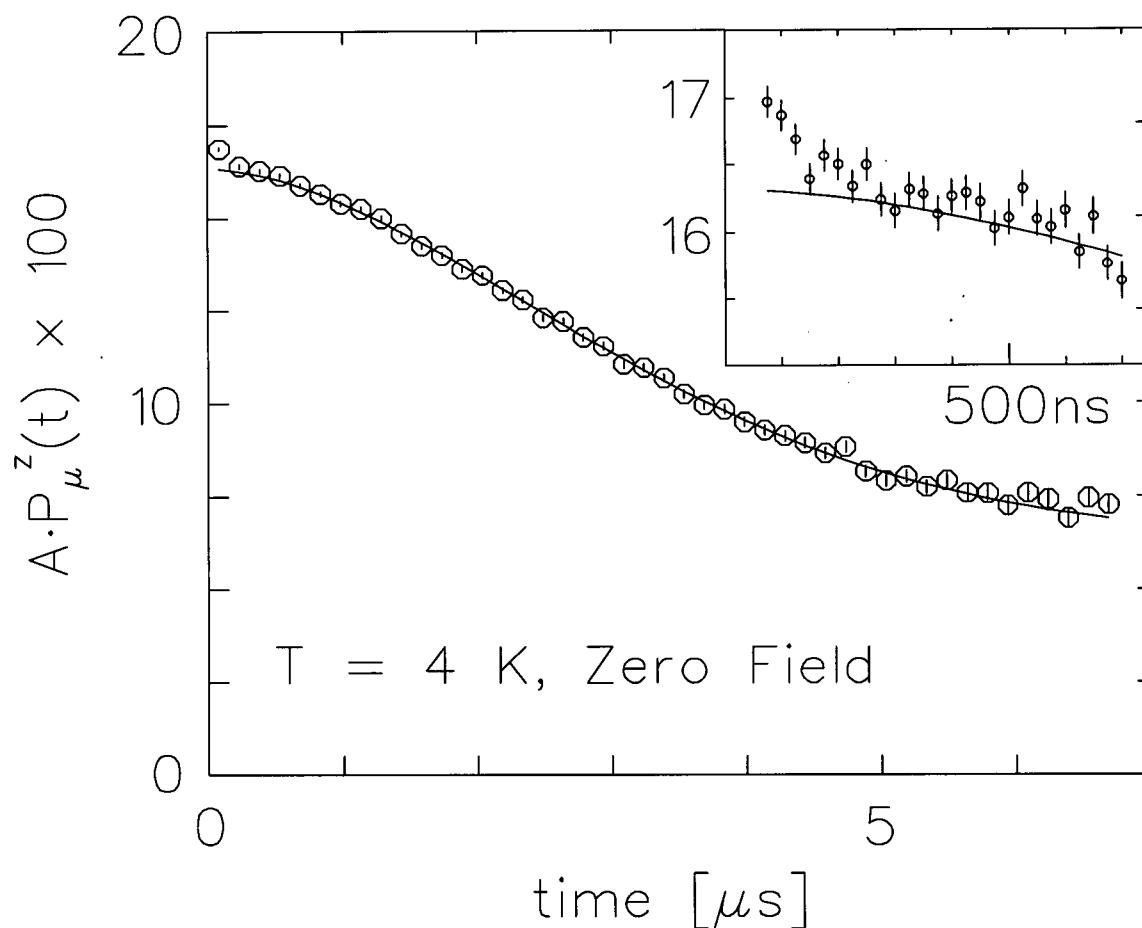
Figure 4.28: A high statistics zero applied field time spectrum in the Meissner state of Rb_3C_{60} at 4K. The slow gaussian relaxation is attributed to the diamagnetic intersti-tial muons relaxing in the distribution of magnetic fields of the randomly oriented static nuclear dipoles, while the small fast relaxing component (inset) is probably due to re-laxation of the endohedral $Mu@C_{60}$. Both dynamic and static random magnetic fields can contribute to this relaxation. Dynamic fields could be due to remnant states within the gap as seen in finite low temperature zero bias conductance in several tunneling experiments. Static fields could be due to nearby nuclear dipoles.
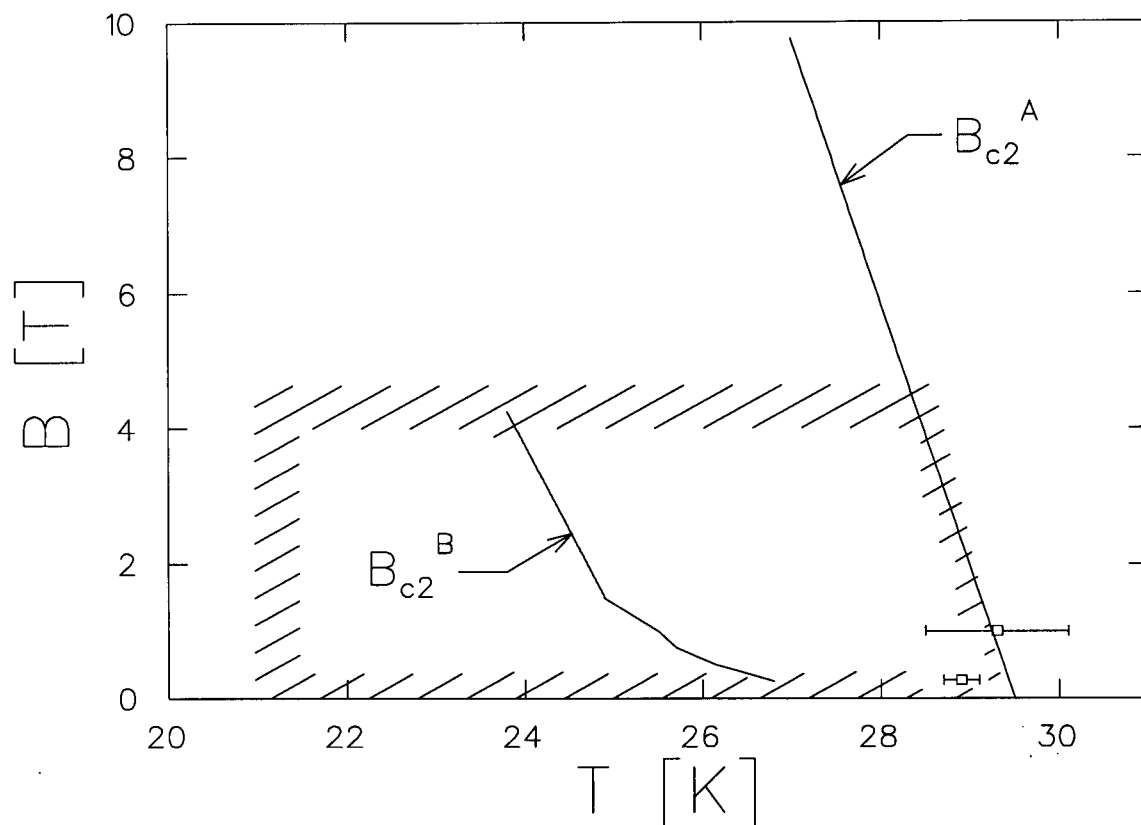
Figure 4.29: The H–T phase diagram of Rb_3C_{60} near $T_c(0) \approx 29.5K$. The curves are two different measurements of the upper critical field. The curve labelled A is from [31] and the curve labelled B is from [36]. The curvature of B is reminiscent of the "irreversibility line", which separates the vortex liquid and solid phases. The hatched region is the region of the coherence peak measured by $\mu S\mathcal{R}$. The error bars are the measurements of $T_c(H)$ from the TF $\mu S\mathcal{R}$ (see Table 4.5) which are near curve A. Notice that the entire region of this diagram is contained in the extreme lower right corner of the generic phase diagram shown in Figure 3.12, so that the absence of the coherence peak expected in region (i) of Fig. 3.12 does not explain the observed damping which occurs at $H/H_{c2}(0) \approx 0.1$.

4.3.2 $T_1(T)$ and Quench Rate Dependence in Na_2CsC_{60}

In two separate measurements on the *same sample* of Na_2CsC_{60}, we observed very different behaviour. In the initial run, we found no broadening of the TF precession signal associated with T_c. We did, however, observe the expected $Mu@C_{60}$ T_1 relaxation. The temperature dependence of this relaxation rate remained Korringa like (Fig. 4.30a) down to about 8K, below which it began to increase. To ensure that the sample hadn't deteriorated, it was recharacterized by x-ray diffraction after this run. In the subsequent run, we observed T_c in TF (Fig. 4.19) and in LF (Fig. 4.31a). Because of the low temperature of the structural phase transition in this material[200] (299 K), we suspected a quench–rate dependence, possibly due to frozen orientational disorder. We attempted a fast–quench (sample at 300K for 20 minutes, then quenched to 200K in 5.5 m and to 5K in about 20 minutes), and found that this cooling procedure did not affect the height of the coherence peak, but it did reduce the low temperature T_1 rates at 2.7K in both 1T and 0.3T (stars in Fig.4.31). However, with no evidence at the time for ambient pressure polymerization, we did not attempt a slow quench or anneal, and, only for the last three points, did we record the cooling procedure in sufficient detail. It now seems likely that, as in the case of Na_2RbC_{60}, there exists another stable ambient pressure low temperature phase of Na_2CsC_{60}, which may involve C_{60} polymerization. According to our measurements (Fig.4.30) this phase is metallic, non–superconductig and appears to exhibit a low temperature (possibly magnetic) phase transition. We note that attempts by another group have not produced a polymerized phase in Na_2CsC_{60}.[139] The unusually small value of $(T_1T)^{-1}$ in Na_2CsC_{60} (discussed in §4.1) *cannot* be explained by the coexistence of the superconducting (s–Na_2CsC_{60}) and non–superconducting (ns–Na_2CsC_{60}) phases, as the values of $(T_1T)^{-1}$ are indistinguishable except below $\sim$8K. However, as the fast–quench procedure suggests, a small fraction of the non-superconducting phase could

explain the finite low temperature rate in Fig. 4.31. The field dependence of T_1^{-1} in the ns–Na_2CsC_{60} was also indistinguishable from the superconductor at 35K (Fig. 4.14a), but at 3K, appeared to fall more sharply with field. In addition there was a small peak in the linewidth of the diamagnetic precession at $\sim 7.5K$ in ns–Na_2CsC_{60}. The absence of a strong T dependence below 10K in the diamagnetic signal is consistent with the enhanced sensitivity of Mu due to the bound electron moment. One possible explanation for the feature in TF, is that ns–Na_2CsC_{60} is superconducting over a narrow range in temperature, and is re-entrant at about 7K to a low temperature non-superconducting phase.

Despite the complications due to the presence of some fraction of ns–Na_2CsC_{60} in the superconducting run, we can compare the temperature dependence of T_1 with the cubic $Fm\bar{3}m$ materials discussed above. In order to account for an ns–Na_2CsC_{60} fraction, we model $(T_1T)^{-1}$ as the sum of the Hebel–Slichter integral Eq. (3.9) with an additional T independent term. Such fits are shown in Fig. 4.31.

The fast quench points indicate that for s–Na_2CsC_{60}, the values of Δ (Table 4.6) are not reliable. The size of the coherence peak, relative to the normal state, though, is not dramatically different than in the $Fm\bar{3}m$ materials. This implies that orientational disorder is not likely to be the cause of the broadening of the coherence peak (or g_S).

These results clearly indicate the need for further experiments on Na_2CsC_{60} with careful attention paid to the cooling procedure. The rapid quench points suggest that one should be able to make a much more reliable estimate of the paramaters of s–Na_2CsC_{60}. It also seems likely that in order to study ns–Na_2CsC_{60}, it will probably be necessary to investigate temperatures lower than those accessible by pumped liquid Helium cryostats.
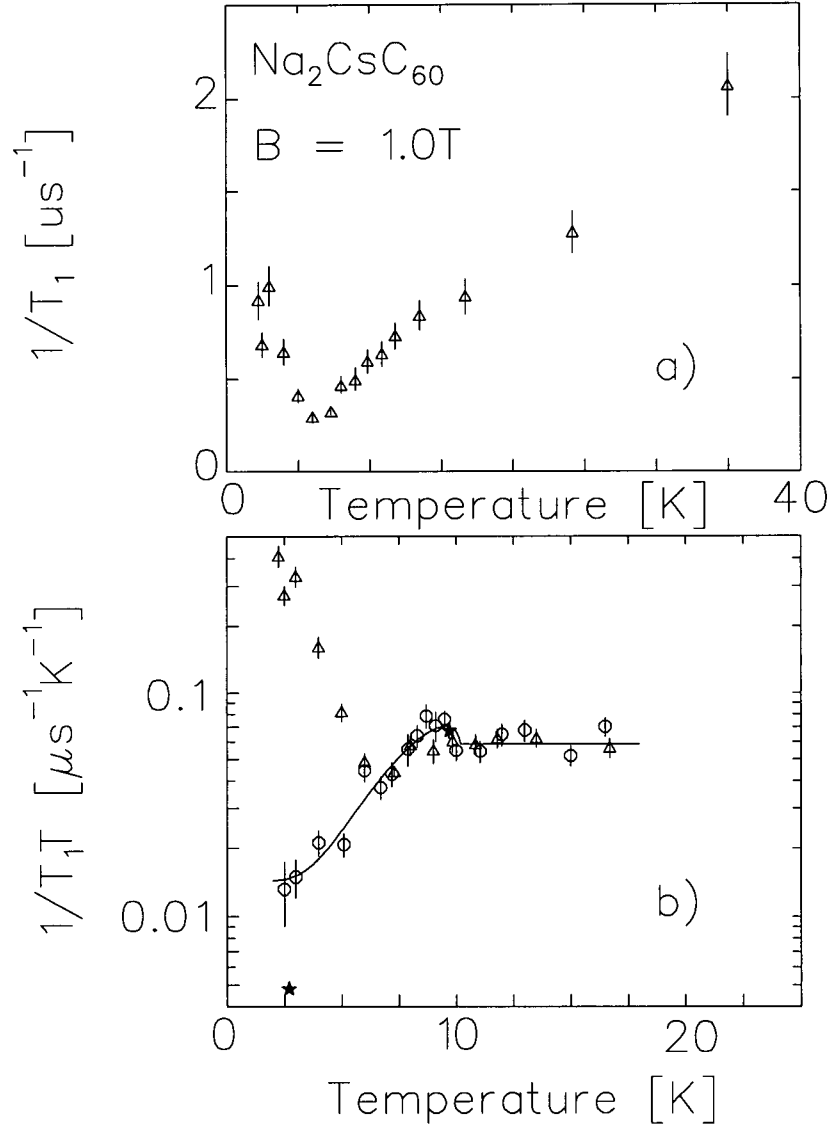
Figure 4.30: Quench rate dependence of the Mu@C_{60} T_1 relaxation rate in Na$_2$CsC$_{60}$. All data are from the same sample. *triangles*: non–superconducting run, *circles*: superconducting run, *stars*: fast quench. Note that above about 10K, the values of T_1T in both runs are about the same. The line is the same fit as in Fig. 4.31a.
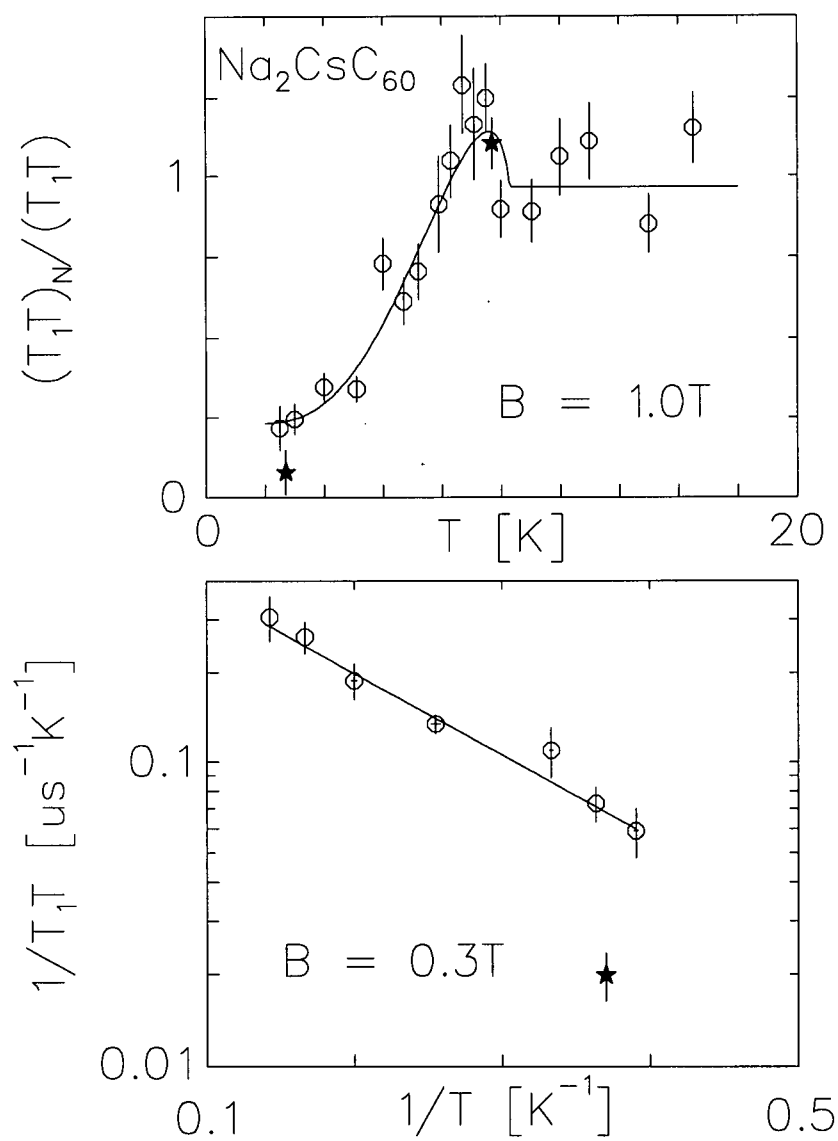
Figure 4.31: The coherence peak and low temperature fall off in superconducting Na_2Cs. The solid stars indicate fast quench runs (described in the text).

Chapter 5

The Time Dependent Spin Polarization in Zero Field

In this chapter we describe the time dependence of the spin polarization of the muon in a solid in zero applied field. Even in the absence of an applied field, there are typically local internal magnetic fields. The origin of these fields can be nuclear dipoles, electron orbital or spin moments, and generally the fields may be dynamic (either because of dynamics of the magnetic system or, in certain circumstances, because of muon motion).

First, consider the situation of completely static fields, i.e. the correlation time for the field experienced by a muon τ is much greater than the muon lifetime τ_μ. To make the following discussion general, we allow for multiple muon sites in the material and index the site by i. There are generally of the order N sites of type i, and they are all crystallographically equivalent (N is the number of crystalline unit cells in the sample). The magnetic field distribution function (for site i) $\Phi^i(\mathbf{B})$. is defined as the probability that the magnetic field at site i is $\mathbf{B}$. For a perfectly ordered magnetic structure in which the all the sites of type i are *magnetically* equivalent[1], i.e. the field at each site is the same $\mathbf{B_0}$, $\Phi^i(\mathbf{B}) = \delta(\mathbf{B} - \mathbf{B_0})$. In practice, this situation is approximately realized in crystallographically dense magnetic systems at temperatures much less than the magnetic ordering temperature. A single muon experiencing a local field $\mathbf{B}$, simply precesses in that field, so the ensemble average time evolution of the muon spin polarization is

$$P_z(t) = \sum_i f_i \int d^3 \mathbf{B} \Phi^i(\mathbf{B})[(\hat{B} \cdot \hat{z})^2 + (1 - (\hat{B} \cdot \hat{z})^2)) \cos{(\gamma_\mu B t)}], \qquad (5.1)$$

---

[1] For this to occur, the magnetic structure must be commensurate with the lattice

103

where the initial muon spin polarization is in the $\hat{z}$ direction, $\hat{B}$ is the direction of the field **B**, and the probability of any given muon ending in a site of type i is f_i. For the delta function field distribution, then $P_z(t)$ will then be simply the sum of a constant term and an oscillating term.[2] At the opposite extreme (from the ordered field distribution) is the situation of complete disorder. The field distribution in this situation can be modelled in several ways. If the local field is disordered in *orientation*, its components will be uncorrelated, and the field distribution will factor:

$$\Phi^i(\mathbf{B}) = \Phi^i_x(B_x)\Phi^i_y(B_y)\Phi^i_z(B_z), \tag{5.2}$$

where the probability that **B** in site type i will have a component B_j is $\Phi^i_j(B_j)$. Following this assumption, one can now postulate a form for the random field distribution, which will depend on the particular situation under consideration. A common situation is that of randomly oriented nuclear dipoles. In the situation where these moments are relatively dense, it is found that a Gaussian field distribution (centred at zero) is appropriate, i.e.

$$\Phi^i_j(B_j) = \frac{1}{\sqrt{2\pi}\sigma}\exp\left(-\frac{B^2}{2\sigma^2}\right), \tag{5.3}$$

where σ, the width of the field distribution, is correlated with the size of the nuclear dipole moment and the average distance between the muon site and the nuclei. If the nuclear moments are more dilute, there will be a wide variety of distances between the average muon and the nearest moment. Because of the strong spatial dependence of the magnetic field due to a point dipole, muons that stop far from any moment will experience a much lower field than muons that stop near a moment. In this situation, the field distribution is broader than a Gaussian, and is better modelled by a Lorentzian

---

[2]Note that in some cases of local moment antiferromagnets the muon site accidentally lies in a position where the fields of the magnetically ordered moments cancel exactly. In this situation no oscillation is observed.

(centred at zero), i.e.

$$\Phi_j^i(B_j) = \frac{1}{\pi}\frac{w}{w^2 + B_j^2},\tag{5.4}$$

where w is a parameter which characterizes the width of the Φ^i and is correlated with the size of the dilute moments and their volume density.

The integral Eq. (5.1) can be done analytically for both of the above field distributions. The results, known as the Gaussian and Lorentzian Kubo–Toyabe functions (respectively), are:

$$P_z^i(t) = \frac{1}{3} + \frac{2}{3}(1 - \gamma_\mu^2\sigma^2t^2)\exp\left(-\frac{\gamma_\mu^2\sigma^2t}{2}\right)\tag{5.5}$$

$$P_z^i(t) = \frac{1}{3} + \frac{2}{3}(1 - \gamma_\mu wt)\exp\left(-\gamma_\mu wt\right)\tag{5.6}$$

These functions with their associated field distributions are plotted in Fig. 5.32. Note that if one assumes that an observed $P_z(t)$ is due to a static random field distribution, then one can find the distribution by using an approximate inversion of Eq. (5.1), e.g.

$$\Phi(B) = \frac{3\gamma_\mu}{8\pi^2}\int_{-\infty}^{+\infty} dt\Theta(t)(P_z(t) - 1/3),\tag{5.7}$$

where Θ is the unit step function which is zero for negative argument.

For any field distribution, there will, on physical grounds, generally be a maximum value of the field at site i, B_{max}^i. This fact together with the form of Eq. (5.1) implies that, at $t = 0$, $\frac{d}{dt}P_z(t) = 0$. This is clearly not the case for the Lorentzian Kubo–Toyabe, Eq. (5.6). This is because the Lorentzian field distribution is unphysically broad, and is merely an approximate model. All real field distributions will have a high field cutoff that is sharper than the Lorentzian, and $P_z(t)$ will be flat at early times. However, the turnover to zero slope at early times may occur on a timescale which is experimentally inaccessible. The time t_{min} before which $P_z(t)$ is not observed depends on the details

of the experiment, but t_{min} is typically in the range 1ns–100ns. The lorenztian Kubo–Toyabe may be a reasonable model for $P_z(t)$, but only for $t > t_{min}$.

The general features of $P_z(t)$ which are characteristic of random field distributions centred at zero are: i) the early time fall off, whose rate is proportional to the width parameter of the distribution, ii) the dip, whose depth depends on the width of the distribution and whose position is inversely proportional to the width parameter, and iii) the late time recovery to 1/3 of the full polarization. The source of the 1/3 "tail" is simply that on average 1/3 of the muons polarization will lie parallel to the local field and consequently not precess (time independent term in Eq. (5.1)). Note that the 1/3 tail is robust to the average over multiple sites, but that the dip is not. If the variation of the width parameter of the field distributions between different sites varies the position of the dip by an amount on the order of the breadth of the dip, the dip will be obscured by site averaging.

Between the extremes of the delta function and random field distributions, there is a broad range of behaviour. For a magnetic system, if the ordering wavevector is away from the extremes of the Brillouin zone (centre or corners) or if there are multiple ordering wavevectors, all sites of type i will not be magnetically equivalent, and some broadening of the field distribution from the ideal delta function will occur. Similarly, broadening will occur because of the coexistence of any disorder, for example, random nuclear diploes + some ordered magnetic state, or simply imperfect order of the magnetic structure. Generally, oscillations due to sharp peaks in field distribution will occur in magnetically ordered systems, but they will be damped by the effects mentioned above. The work of Kalvius [208] provides a general review of $\mu S R$ in metallic magnets.

It is interesting to consider the effect of application of a longitudinal field (in the $\hat{z}$ direction) which is on the order of the internal fields. In this case the same model

(Eq. (5.1)) for the time dependent average polarization can be used, but the field distribution is *shifted* because the *net* local field is the vector sum of the applied field ($\mathbf{B_{app}}$) and the internal field. As the applied field is increased, it is clear that the net field at all sites will approach the direction of the applied field $\hat{z}$, and hence the time–independent part of the integral Eq. (5.1) will dominate, and the time–dependence will be "quenched". For the delta function field distribution, the amplitude of the oscillating part of $P_z(t)$ will simply decrease continuously to zero as B_{app} increases. For random distributions, the "relaxation" quenches when B_{app} is of the order of the width of the random field distribution, for example see Fig. 5.33. There are thus two ways to measure the breadth of a static random field distribution: i) the magnitude of a zero field relaxation rate (converted with the appropriate factor $2\pi\gamma_\mu$), and ii) the LF at which the zero field depolarization is quenched. Note that, if the internal fields are dynamic, these two measures do not agree (see discussion below).

So far, we have discussed the magnetic field distribution as if it were simply a *classical* field, which the muon samples randomly in space. However, the sources of these fields are electronic currents and electronic and nuclear spins, and should be treated quantum–mechanically. Instead of simply treating the muon spin quantum mechanically in the local field, one should correctly consider the full hamiltonian of the solid + muon + interactions. Practically, the only entities that need to be treated quantum mechanically are those that interact strongly with the muon, i.e. the nuclei and electrons in the immediate vicinity. For most situations, even the local environment of the muon can be treated in an effective classical picture. One exception is, however, muonium. In zero field the time dependent muon spin polarization in muonium is determined by the *hyperfine spectrum*, i.e. it contains oscillating components at well defined frequencies: the zero field splittings of the hyperfine levels. The spectrum of frequencies can be complicated further by the indirect nuclear hyperfine coupling of Mu to neigbouring nuclear dipoles

or by anisotropy of the hyperfine interaction. An example of this occurs in pure fullerite at low temperature, where because of the anisotropy of the hyperfine interaction, the spectrum of the exohedral $C_{60}Mu$ radical contains several frequencies in zero field which are low enough to observe,[3] see Fig. 5.34. Note that, in the presence of magnetism, the large electronic moment in Mu will cause the time–dependence of any Mu signal to be of unobservably high frequency. Quantum mechanical treatment of the full dipolar interaction can be found in [98, 209]. Note that for muons, relaxation by nuclear or electronic moments is always of the "unlike spins" category (see §IV.III of [209]).

The time–dependent polarization $P_z(t)$ observed in zero field is related to the polarization function in high ($B_{app} \gg$ the internal fields) transverse field $P_x(t)$. In this case the envelope of the oscillations at the Larmor frequency of the muon measures nearly the same thing as $P_z(t)$, since the muon is simply precessing in the net field. However, in TF, the two directions perpendicular to the muon spin are inequivalent (since one is along the applied field), whereas in ZF they are equivalent. Thus the relaxation rate is reduced geometrically by a factor of $\sqrt{2}$. In addition for the case of relaxation from the full dipolar interaction (including non–secular terms), the relaxation rate in TF may, in some cases, be reduced by another factor of $\sqrt{(5/2)}$ [210]. This extra enhancement in zero field, from terms in the interaction which in ZF cause the muon and nuclear moments to flip–flop, *does not occur* in the case of magnetically ordered moments, because the energy required to flip the ordered moment is non–zero (it is given by an exchange energy, which is generally quite large). Because of this enhancement (and also because of the large frequency shifts in TF experiments in magnetic materials), zero field $\mu S \mathcal{R}$ is the preferred $\mu S \mathcal{R}$ technique for the study of magnetism.

---

[3]This is not the case for isotropic vacuum–like Mu, where the singlet–triplet hyperfine frequency is too high to observe easily.

Dynamics in the magnetic field introduces a further complication in $P_z(t)$. The spectral density $J(\omega)$ of the local field is simply defined as the Fourier transform $J^i(\omega) = \mathcal{F}[\mathbf{B^i(t)}]$. Time variation of the local field can induce muon spin flip transitions. These flips occur randomly at a constant rate, leading to a characteristic exponential relaxation in $P_z(t)$. The rate of this relaxation is determined, for example in time dependent perturbation theory, by the value of J at the Larmor frequency of the muon (in the time averaged local field). We note that if the fluctuations in the field are either too slow or too fast, they will be ineffective in causing relaxation. Dynamics can be included in a number of ways, which will not be discussed here. The following qualitative features arise from dynamic features. Quenching of the dynamic relaxation by application of a longitudinal field (e.g. Fig. 5.33) is much less effective. In the dynamic case, quenching occurs only for fields such that $\gamma_\mu B$ exceeds the highest frequency ν_{max} with appreciable spectral density J of the fluctuations. The quenching field thus depends sensitively on the particular dynamics involved, but is generally much larger than the field estimated from the zero field relaxation function (assuming it is of static origin). In the case of slow dynamics, relaxation of dynamic origin may only be apparent as a slow exponential decay of the 1/3 tail of $P_z(t)$, and may be modelled as an exponential relaxation $(\exp{(-\lambda t)})$ times a static Kubo–Toyabe function. There are also some exotic systems in which the ZF relaxation appears to be static in origin (i.e. Gaussian) but is, in fact, dynamic [211].
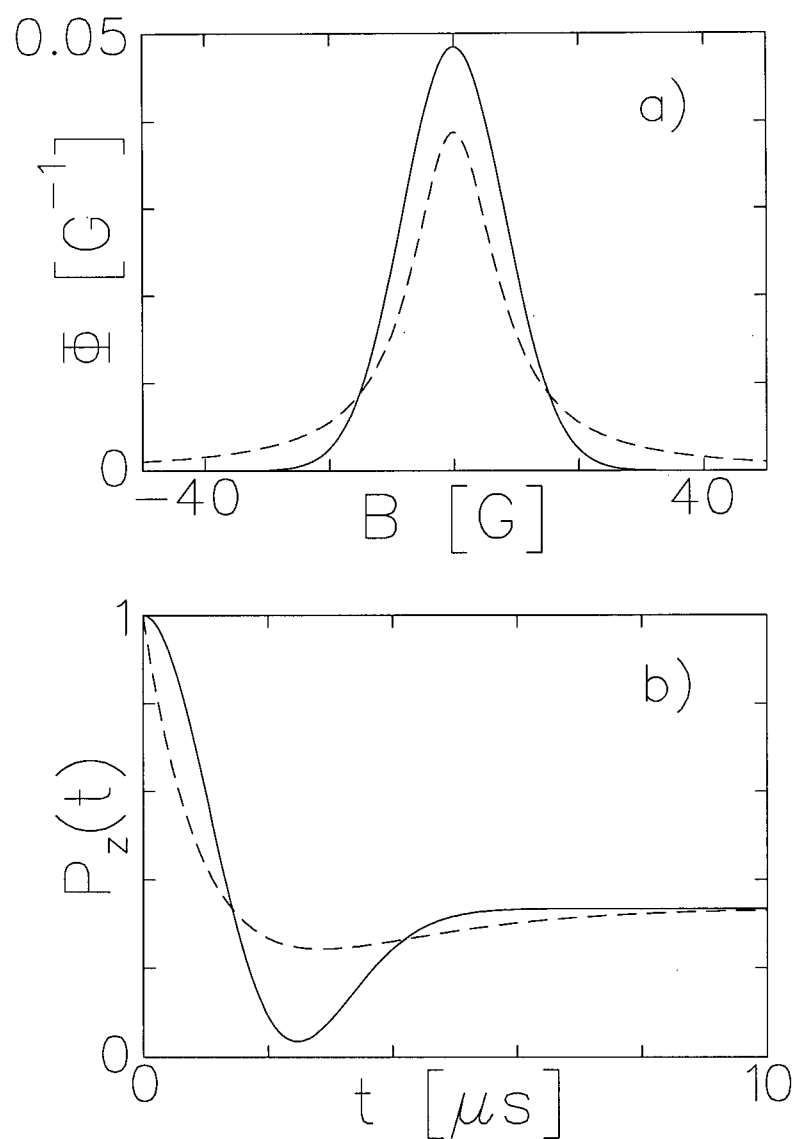
Figure 5.32: *a)* Gaussian (solid) and Lorentzian (dashed) field distributions and *b)* the corresponding Gaussian and Lorentzian Kubo–Toyabe functions for $\sigma = w = 0.7\mu s/2\pi\gamma_\mu$.
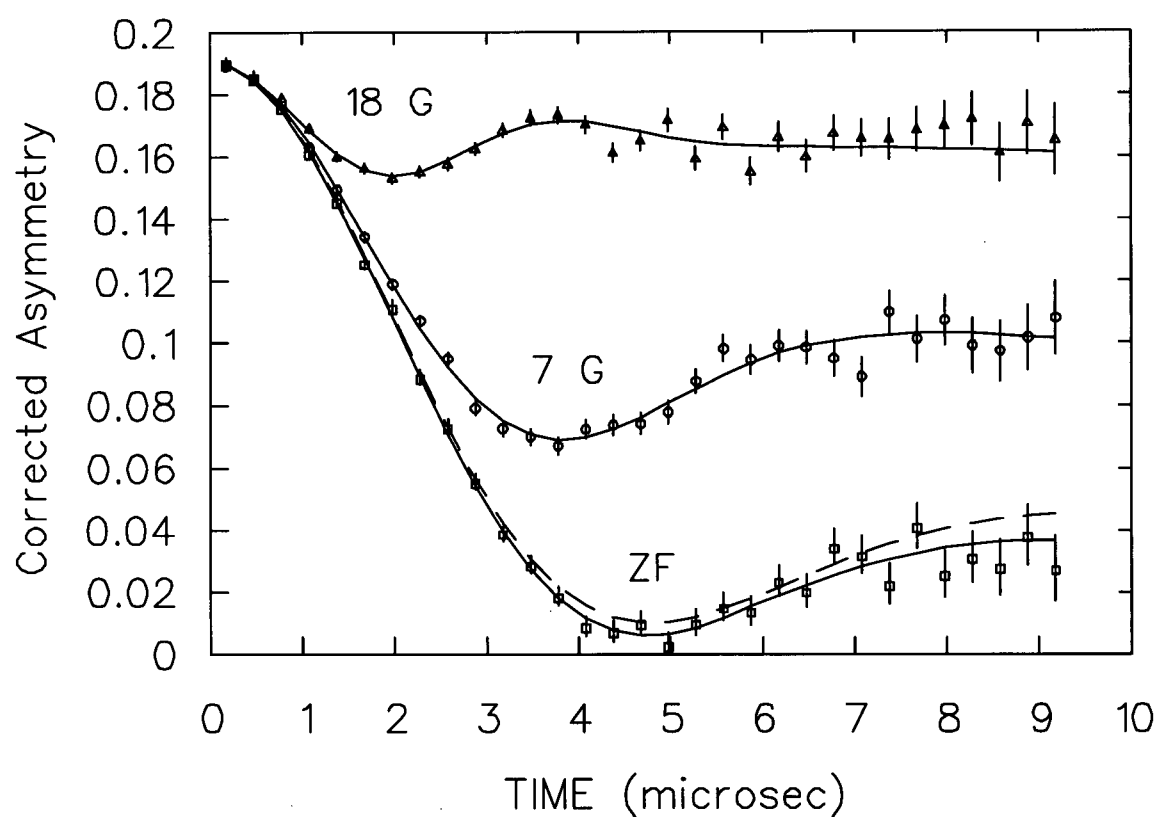
Figure 5.33: Quenching of the zero field depolarization (which is approximately a static Gaussian Kubo–Toyabe) by application of a longitudinal field (from [81]).
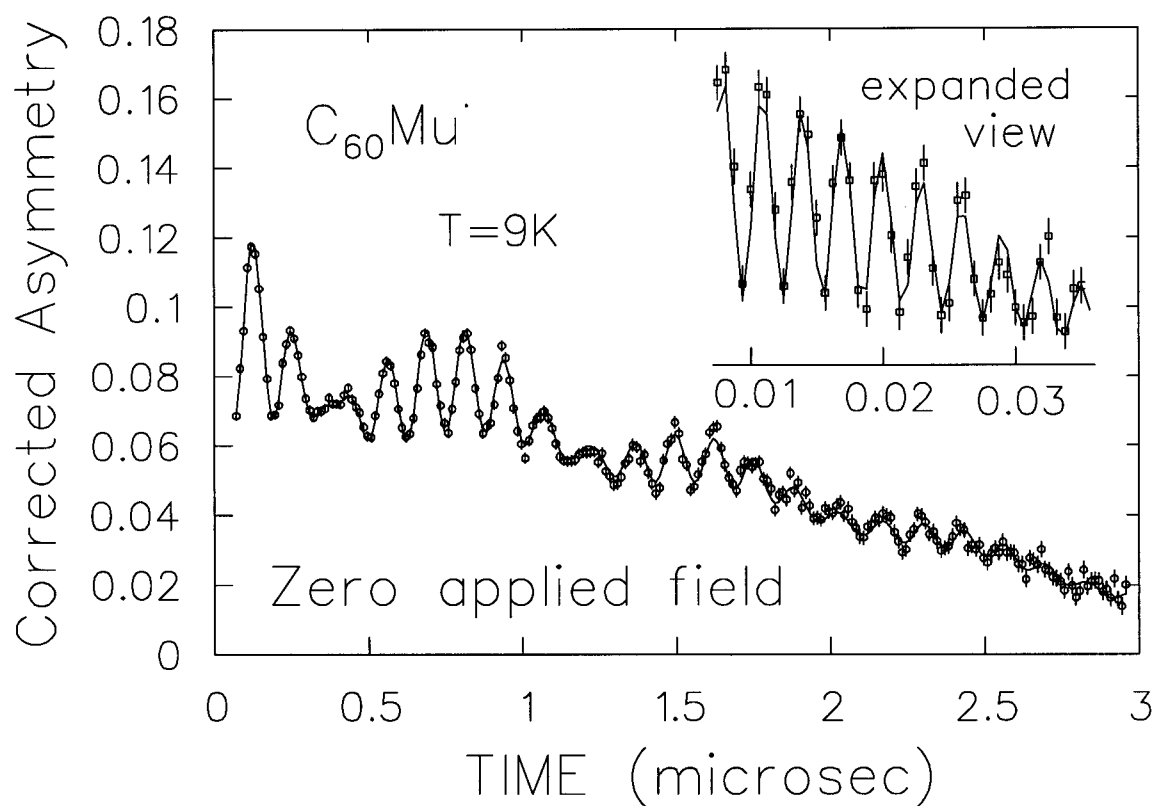
Figure 5.34: Oscillations in zero field due to anisotropy of the hyperfine interaction of the molecular radical $C_{60}Mu$ (from [172]).

Chapter 6

$\mu\mathcal{SR}$ in A_1C_{60}

In this chapter, experimental results on the three A_1C_{60} systems (A = K, Rb, Cs) are presented and discussed. The main results are from ZF (see chapter 5), but some LF and TF measurements are also presented.

Some $\mu\mathcal{SR}$ results on each of these systems have been published previously by our group and others, see [174, 212, 213, 214]. Additional ZF data by the authors of [214] has been reported in very brief form in [215]. These experiments have concentrated on the low temperature magnetic phase (A = Rb, Cs), and use mainly the ZF technique.

The main purpose of these experiments was to test a SDW conjecture offered to explain the low temperature drop in spin–susceptibility measured by ESR[66]. All the $\mu\mathcal{SR}$ measurements confirm the existence of a low temperature magnetic state which is characterized by a broad distribution of *quasi–static* fields. However, there is considerable debate over what magnetic structure gives rise to the observed distribution. Recently, low temperature measurements for (A = Rb, Cs) have been reported[215]. No qualitative change of the relaxation was observed between 2K and 100mK. The only reported measurements of $\mu\mathcal{SR}$ for A = K are those of [213]. The conclusion of these measurements is simply that unlike the other materials, there is no magnetic ordering in K_1C_{60} down to 2.5K.

6.1 $\mu\mathcal{SR}$ in the Magnetic State of A_1C_{60}

In this section, results of measurements on the low temperature magnetic phase of A_1C_{60} for A = Rb and Cs are presented. The observed depolarization is discussed, and a phenomenological form is used to parametrize the relaxation, so that its temperature (and field) dependence can be conveniently summarized. All discussion of the results, however, is deferred to the following section. Note that because of the large size of the bound electron moment, the contribution of muonium (discussed in the §6.3) to the ZF or TF spectra *in the magnetic state* will be an exceedingly fast relaxing signal, which may only be apparent as a missing fraction.

6.1.1 Zero Field $\mu\mathcal{SR}$ in Rb_1C_{60} & Cs_1C_{60}

The ZF muon spin relaxation at low temperature for A = Rb and Cs is shown in Figure 6.35 (together, for comparison, with similar spectra for A = K). The quenching by LF of the ZF relaxation is also shown. The low field required to completely quench the relaxation indicates that in each case the relaxation is due to small static magnetic fields on the order of 10mT. Although the fields are small compared to the internal fields in many magnetic materials, they are still considerably larger than the expected nuclear dipolar fields, implying that they must be of electronic origin. The characteristic features of the relaxation in the magnetic state (Fig. 6.35a and 6.35b) are that there appear to be two well defined components, one fast–relaxing and one slow–relaxing. We note that this qualitative behaviour has been confirmed by ZF $\mu\mathcal{SR}$ measurements in these systems by other groups; furthermore, it is not very different from the form of the relaxation in other fulleride magnets [138, 216].

A closer look at the fast relaxing component for A = Rb (see Fig. 6.36) reveals that the relaxation is quite exponential (and otherwise featureless) back to the earliest

times accessible in the data.[1] At the top of Fig. 6.36, the relaxation at 50K (above the magnetic transition) is shown for comparison, and at the bottom the analogous TF relaxation at 1.5T is shown in the rotating reference frame, rotating at the average precession frequency. The spectrum at 2K (stars) is from a different sample than the rest of the data, and indicates sample independence of the qualitative features of the ZF relaxation at early time.

It has recently been found that the sample corresponding to the stars in Fig. 6.36 likely contains an impurity phase of Rb_3C_{60} (perhaps as large as 20% [217]). It is not known whether the previous sample contains a similar impurity phase, but it is possible. For comparison, the low temperature ZF spectrum in Rb_3C_{60} is shown in Fig. 4.28. It is clear that the small Mu component from a small fraction of Rb_3C_{60} would be too small in amplitude to make a significant contribution to the relaxation shown in Fig. 6.36. Thus the observed relaxation is attributed predominantly to Rb_1C_{60}

In contrast to A = Rb, for A = Cs at the lowest temperature, there appears to be a rapidly damped oscillation (Fig. 6.37). A subsequent measurement on the same sample in the dilution refridgerator (DR) at 1.0K is shown for comparison. The overall asymmetry in the DR is lower, but the data at 1.0K and 1.9K are consistent.[2] The oscillation, though, is of relatively small amplitude and cannot be resolved at temperatures higher than 2K. The oscillation frequency at 1.9K and 1.0K is approximately 6 MHz.

The presence of such an oscillation indicates that there is some small degree of magnetic order. The amplitude of the oscillating signal suggests that the fraction of the

---

[1]Note that the data (for A = Rb) contains an oscillating signal at $\approx$ 320MHz which is due to the TDC (described in §2.1.3). This oscillation is binned over in the figure, but its existence effectively limits the timing resolution to a few periods of the clock cycle (3ns). More recent data (stars in Fig. 6.36) does not suffer from this problem.

[2]Note that, except for the data in the DR, all the data for A = Cs was taken in a separate spectra apparatus, and because of the absence of the "t_0" straight–through peaks in the sample spectra in such an apparatus, earlier times are accessible. This is the reason that the DR data begins at 50ns instead of closer to zero time. Moreover, no clock signal is present in any of the A = Cs data.

sample which possesses this order is relatively small (less than $\sim 10\%$). From this data, it is not possible to determine what form the magnetic ordering takes (SDW, local moment AFM etc.). The frequency of an oscillation in the ZF spectrum (due to magnetic ordering) is determined by the size of the field (averaged over all the muon sites). This field is in turn determined by the size of the ordered moment, the distance to the muon site, and the form of the effective coupling. Without knowledge of the muon site, it is not possible to estimate the size of the ordered moment from the oscillation frequency, however, the oscillation frequency in the TMTSF SDW systems[23] is much smaller (< 0.6MHz). Thus if the ordering is of a SDW type, the magnitude of the SDW and/or the coupling between the μ^+ and the SDW must be considerably larger in Cs_1C_{60}. The presence of any sort of oscillation implies that at least a fraction of the muons is stopping in a set of one or a few magnetically equivalent sites. The field at the μ^+, given by the oscillation frequency 6MHz/γ_μ is about 450G. The magnitude of the internal fields is thus consistent (in order of magnitude) with the observed NMR broadening of ~ 2000ppm at 7T [64].

With the exception of the low temperature data in Cs_1C_{60}, no oscillatory behaviour is observed. As discussed in Chapter 5, this indicates that the muons are sampling a distribution of magnetic fields which, for the most part, is highly disordered. In particular, the distribution function $\Phi(\mathbf{B})$ is peaked at or very near $\mathbf{B} = 0$. The absence of the dip and recovery Kubo–Toyabe behaviour (see Fig. 5.32) indicates that the field distribution is broader than a Gaussian. This is also consistent with the fast relaxing early time behaviour, which indicates the presence of some weight in Φ at relatively high fields. The oscillation, for A = Cs, indicates that, in this case, Φ also posseses a small broad peak centred at $B \approx 450$G. In order to summarize the temperature dependence of the ZF spectra, we introduce a convenient relaxation model. However, unlike the frequency of ZF oscillations observed in more ordered magnetic systems, the relation of the relaxation

rate in such a model to a magnetic order parameter is not clear. However, as discussed in Chapter 5, the relaxation rate is directly related to the magnitude of the internal fields (i.e. the width of the field distribution), thus it is an important characteristic of the magnetic state.

A reasonable description of the low temperature data is obtained assuming it is the sum of three terms:

$$AP_z(t) = A_F P_F(t) + A_S P_S(t) + A_{NR}, \tag{6.1}$$

where the subscripts F and S refer to fast and slow, and A_{NR} is a non–relaxing component which accounts for muons stopping in the silver mask around the sample. For the ZF fits, we assume A_{NR} is about 20% of the full asymmetry[3]. One could fit the data using stretched exponentials ($P(t) = \exp[-(\lambda t)^\beta]$) which interpolate between an exponential and a Gaussian, but such a model overparametrizes the data. Fitting the *entire* relaxation to a stretched exponential yields an unreasonably low power $\beta < 0.5$, indicating that the relaxation is highly two component, as opposed to a smooth distribution of relaxation rates.

It is found that the relaxation for A = Rb can be well described with exponential relaxations ($Ae^{-\lambda t}$) for both the fast and slow components; whereas, for A = Cs, a better choice is Gaussian relaxation for both components ($Ae^{-\sigma^2 t^2}$). Once an appropriate form for the relaxation is selected, there are still *two* possible assumptions regarding the behaviour of the two components.

1. If the two components come from two inequivalent muon sites, then we may assume that the relative amplitudes of the two sites remains constant with temperature,

---

[3]As discussed in Chapter 5, if the internal field is random in orientation and completely static, 1/3 of the muon polarization does not relax. This fact has not been incorporated explicitly in Eq. (6.1), since there is no indication that $P_z(t)$ reaches its $t \to \infty$ value in the experimental time–window. This may be due to the breadth of the field distribution and/or slow dynamics in the field. The 1/3 component is thus contained in the slow term of Eq. (6.1).

neglecting any muon site–changing dynamics (which would seem to be inconsistent with the static nature of the relaxation).

2. On the other hand, if the two components are due to some kind of inhomogeneity in the magnetic state, then we may assume the relative amplitudes can vary. An example of this kind of behaviour is found in spin–glasses, where frozen and dynamic regions co–exist, and their relative fractions change with temperature.

It is found that, if the assumption of the first case is pursued, that the relaxation rate of the fast component increases to unrealistically large values as the temperature increases, indicating that the constant fraction assumption is inappropriate. This is also apparent in the data: the fast component appears to change with temperature in *amplitude* more strongly than in relaxation rate.

Thus under the second assumption, we find the following behaviour for the temperature dependence of the ZF relaxation (see Fig. 6.38 for A = Cs and Fig. 6.39 for A = Rb). The fast component seems to decrease continuously in amplitude, with roughly constant relaxation rate as the temperature is increased from 2K. Above about 6K (Rb) and 10K (Cs), the two components become difficult to distinguish. In the case of Rb, the amplitude of the fast component was constrained to approach zero roughly continuously, while for Cs, the two components were allowed to mix. Above 15K (Rb) and 35K (Cs) the relaxations were fit to a single relaxing component. The transition temperature appears to be about 20K for both systems, but there is a broad range of temperatures above this where some sort of onset behaviour is apparent. Even below the transition, the relaxation varies rather gradually with temperature compared with other magnetic systems. [4]

---

[4]Note that the difference in total amplitude in the DR is the result of differences in the counter geometry, thus the two low temperature points for Cs (triangles and nablas in Fig. 6.38b) should not be taken as continuations of the higher temperature data. However, the relative magnitudes of the two components (i.e. they are nearly equal) is consistent with the higher temperature data.
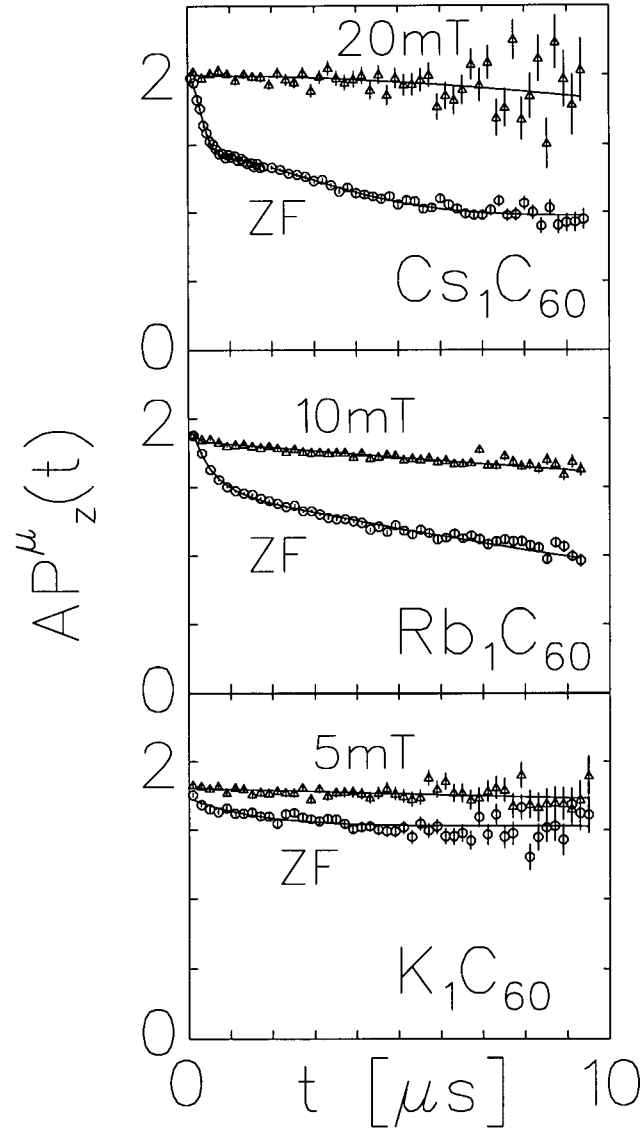
Figure 6.35: The ZF relaxation at low T in all three A_1C_{60} systems, and the quenching of that relaxation by small LF. The quenching indicates that the relaxation is due to a static magnetic field distribution in all three cases. However, the origin of the relaxation is different: for A = Rb, Cs the relaxation is due to diamagnetic muons experiencing the static fields of the low temperature magnetic phase. For A = K, the relaxation is similar, but it is nearly independent of temperature.
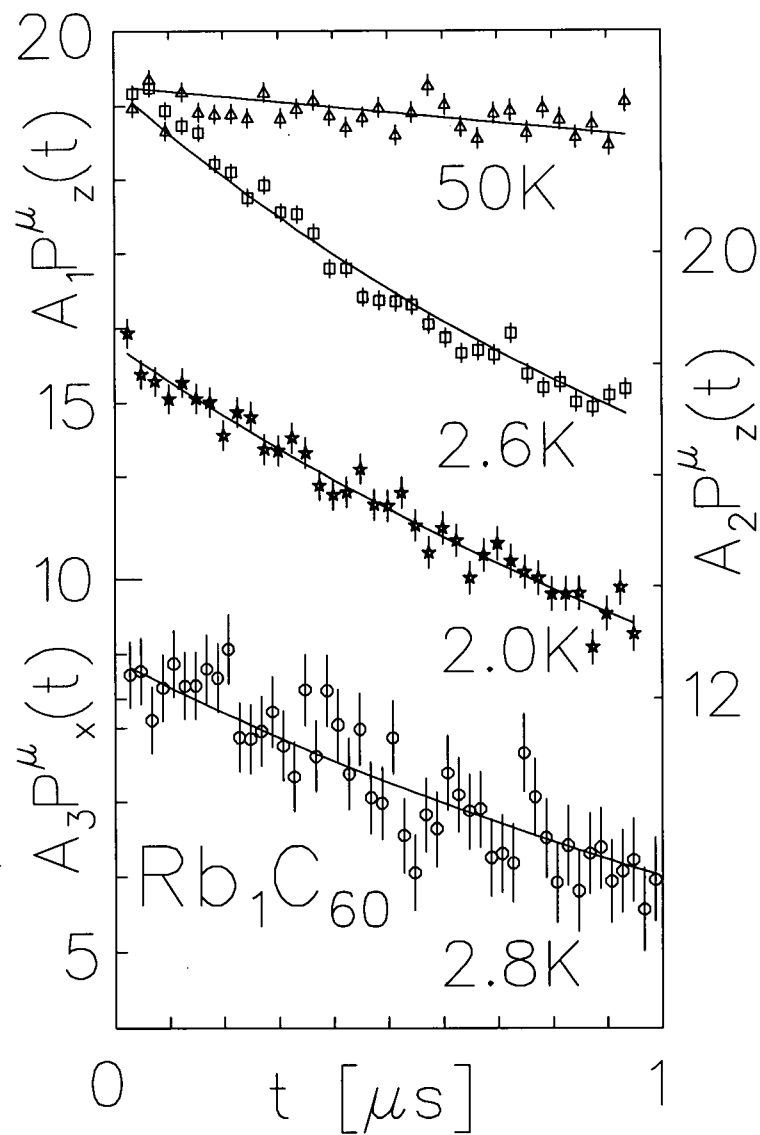
Figure 6.36: The fast component of the low temperature ZF spectrum in Rb_1C_{60}. The relaxation is well described by an exponential to the earliest accessible times. The stars correspond to data taken on a different sample. The lower data is the relaxation envelope of the decay of the TF precession at 1.5T.
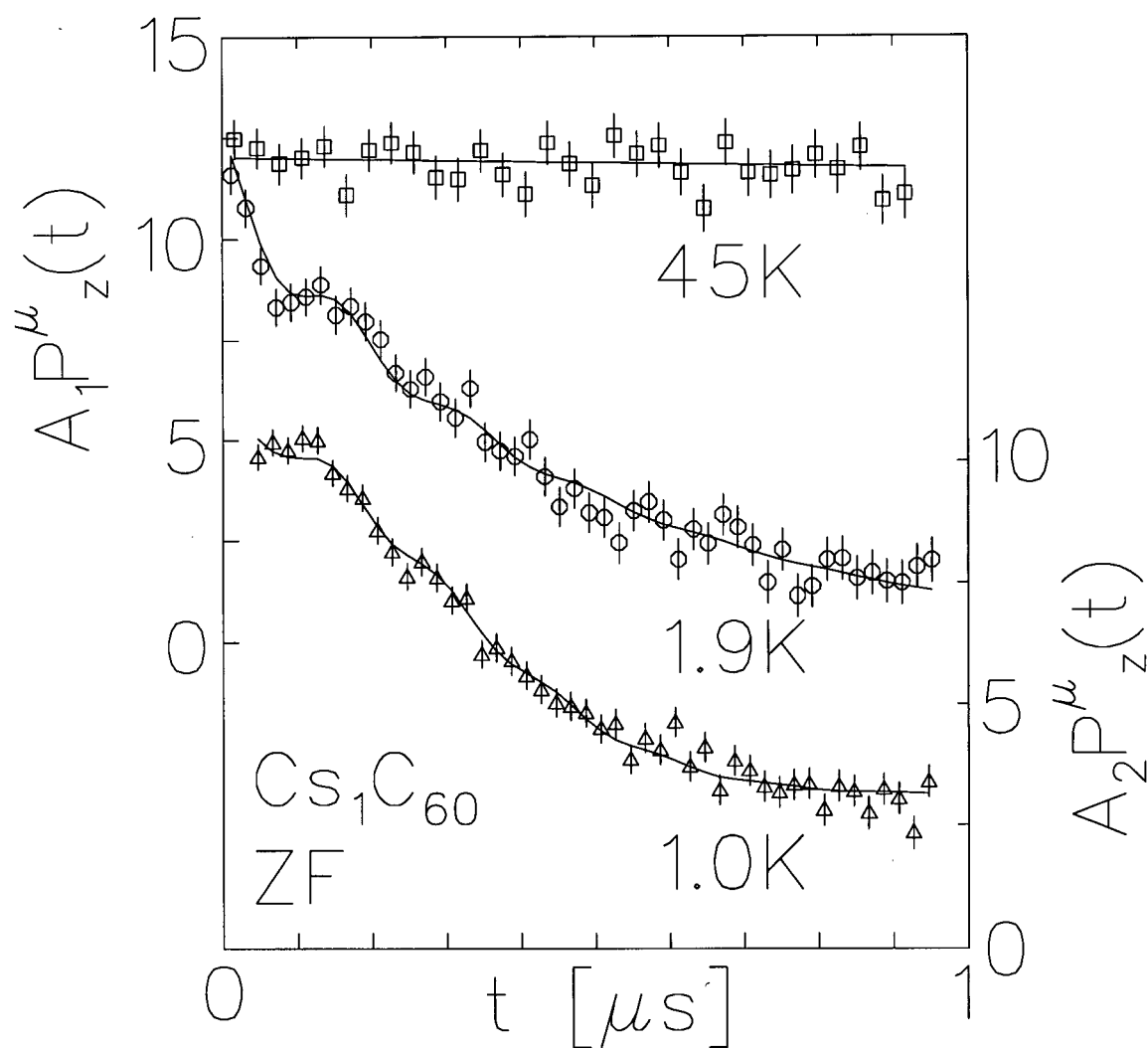
Figure 6.37: The fast component of the ZF relaxation in Cs_1C_{60} at the lowest temperature. There is a fast relaxing oscillation with a frequency of about 6MHz. The 45K data above the magnetic transition indicates that the fast component is *not* due to contamination from the early time straight through peak which *does not occur* in the sample spectra of the separate spectra apparatus.
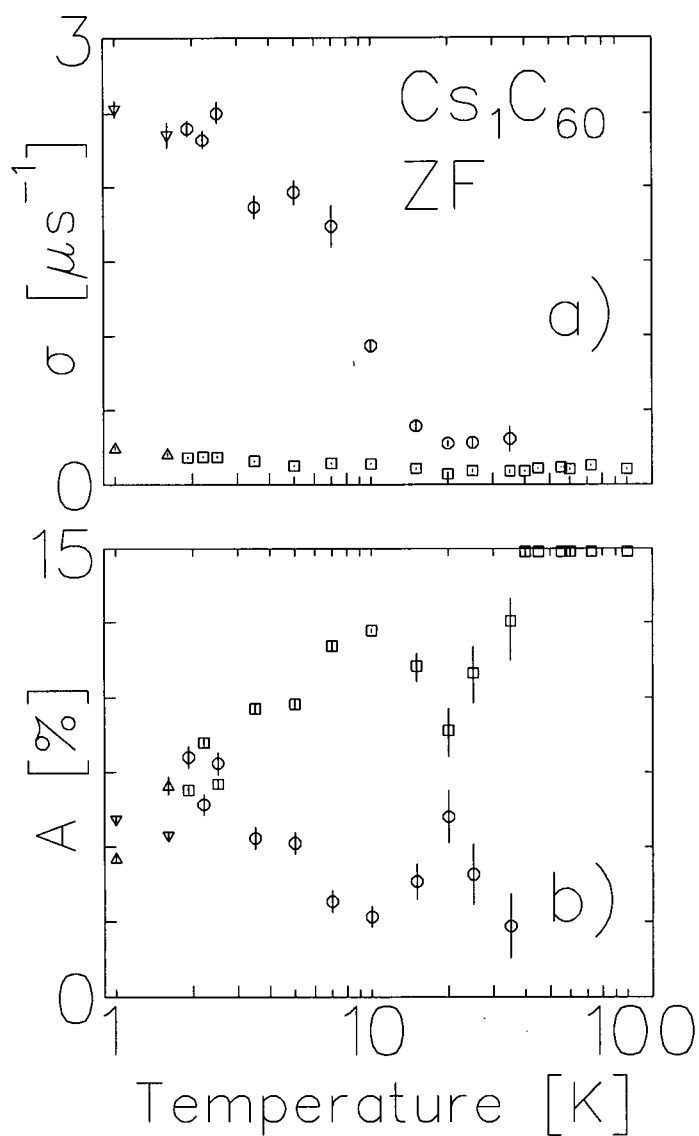
Figure 6.38: Temperature dependence of the zero field relaxation in Cs_1C_{60}. The fit function is the sum of 2 Gaussian relaxations. a) The fast and slow Gaussian relaxation rates and b) The amplitudes of the fast and slow signals. The triangles and nablas are from data taken at a different time on the same sample in a different spectrometer.
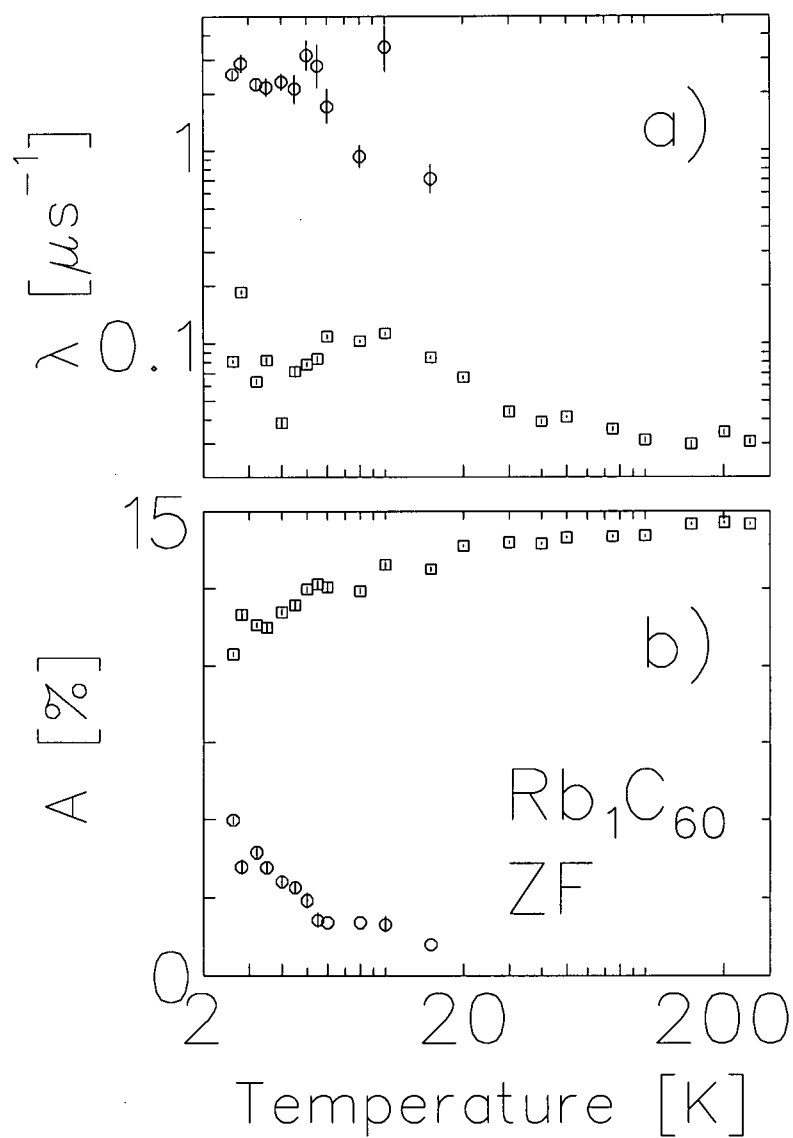
Figure 6.39: Temperature dependence of the zero field relaxation in Rb₁C₆₀. The fit function is the sum of 2 exponential relaxations. *a)* The fast and slow exponential relaxation rates and *b)* The amplitudes of the fast and slow signals.

6.1.2 High Transverse Field in Rb_1C_{60}

In this section TF measurements on Rb_1C_{60} at low temperature (complementary to the ZF results of the previous section) are presented.

The temperature dependence of the transverse field damped precession has been analyzed using the same model for the relaxation as in ZF (i.e. Eq. (6.1)). In addition, to avoid overparametrizing, the phases and frequencies of the three signals were constrained to be equal for the three components.

Fig. 6.40a shows the two component nature of the relaxation in *frequency space*. The lineshape is approximately the superposition of two lines one narrow and one broad. This lineshape is quite similar to the observed ^{13}C NMR lineshape in Cs_1C_{60} shown in [64]. In Fig. 6.40b, the mean frequency shift relative to a calibration run on high purity Ag is plotted. The calibration run was accomplished by affixing a 99.9985% Ag disk (0.25mm thick) to the front of the sample cell window with Apiezon N grease, and remounting the sample cell, thus reproducing the experimental conditions as closely as possible. The frequency shift is corrected for the known muon Knight shift in Ag (+94 ppm [75]) by the following formula,

$$S_c = 10^6 \cdot \frac{f - [f_{Ag}/(1 + 94\text{ppm})]}{[f_{Ag}/(1 + 94\text{ppm})]} \tag{6.2}$$

where f_{Ag} is the observed temperature independent Ag frequency. We note that the frequency shift reported in [214] has the opposite sign, but these authors do not state how the reference frequency was measured. From this plot, the frequency exhibits a positive shift which increases gradually and continuously below 60K. The parameters describing the three component relaxation in 1.5T TF are shown in Fig. 6.41. The qualitative agreement with the ZF results (Fig. 6.39) is clear. Quantitatively, one expects any high TF relaxation rate to be less than the corresponding ZF rate, at least by the geometric factor $1/\sqrt{2}$, and by more in the case where "non–secular" relaxation is appreciable in

the ZF.

Finally, in Fig. 6.42, the results of fitting the three component model to the TF relaxation at 2.8K for various fields are presented. These results may bear on the proposed spin–flop transition which AFMR experiments indicate occurs below 2.7T [70]. Only two points (triangles and nablas in Fig. 6.42a) were taken under field cooled (FC) conditions. The rest were zero field cooled (ZFC). No significant difference was found between the FC and ZFC results, so the points are not distinguished in Fig. 6.42b.[5] There is no strong systematic field dependence in the relaxation rates for either component. However, there is a strong field dependence at low field in the *relative amplitudes*. The analysis of the field dependent amplitude is somewhat complicated by the known effect of muon beam focusing in the HELIOS solenoid [189]. The strong field in the beam direction causes the beamspot to contract continuously up to about 2T (above which the beamspot expands). The effect of this is to change the relative magnitude of the non–relaxing signal (background) A_{NR} relative to the sample signal. This has been approximately accounted for by fixing $A_{NR}(B)$ (stars in Fig. 6.42b). From the plot, it can be seen that the magnitude of the slow component A_S decreases rapidly with field (from the ZF value of about $2A_F$) to become equal to A_F by 1T. At higher fields, $A_S \approx A_F$.

---

[5]The TF data for A = Rb also contains the clock signal mentioned previously. However, the clock signal is well separated from the muon precession frequency, and it can be binned over.
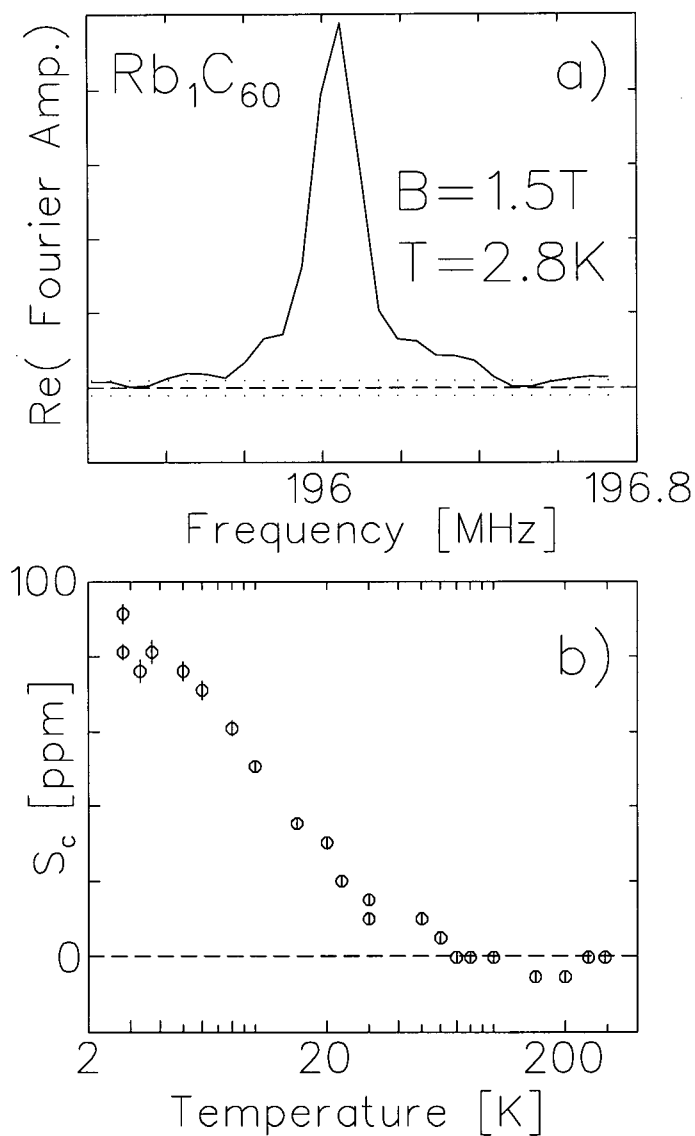
Figure 6.40: *a)* The field–cooled lineshape in the magnetic state of Rb_1C_{60} at 1.5T. The line appears to be the superposition of two lines, one broad and one narrow, in correspondence with the ZF relaxation. *b)* The temperature dependence of the frequency of the line relative to Ag, and corrected for the known muon Knight shift in Ag.
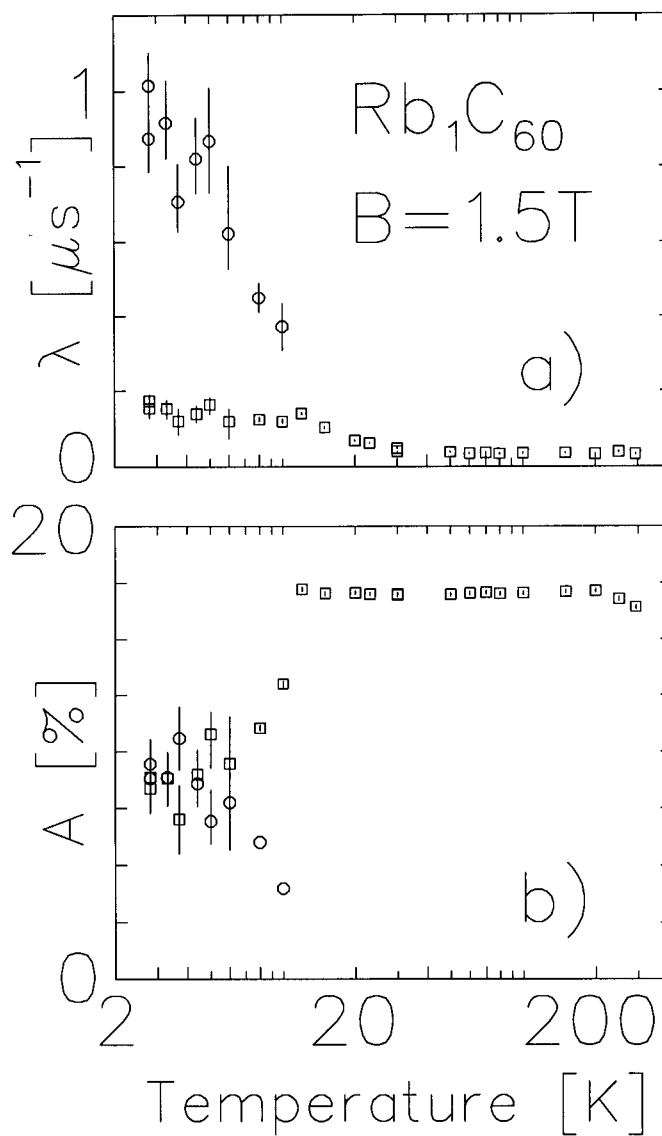
Figure 6.41: The *a)* exponential relaxation rates and *b)* corresponding amplitudes of the two relaxing signals from fits to the 1.5T TF relaxation. The third (non–relaxing) component was held fixed with temperature. Note the saturation to equal amplitudes of the two components.
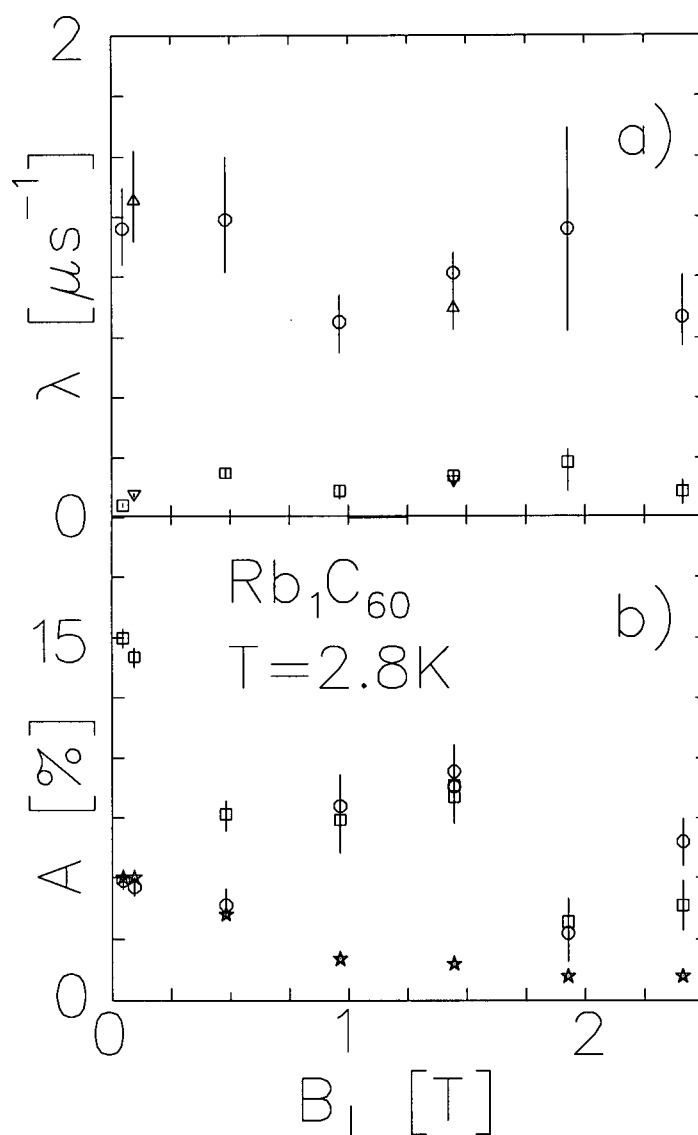
Figure 6.42: The *a)* exponential relaxation rates and *b)* corresponding amplitudes of the two relaxing signals from fits to the TF relaxation at 2.8K as a function of field. The triangles and nablas correspond to field cooled conditions, while the circles and squares are zero–field cooled. Because there was no significant effect of zero field cooling, these two cases have not been distinguished in panel *b)*. The third (non–relaxing) component was assumed to have the field dependence indicated by the stars in *b)*, in order to account for focussing of the muon beam.

6.2 Inferences about the Magnetic Structure in A_1C_{60}

The results presented in the previous section are not as easily interpreted as, for example, the ZF oscillation frequencies observed in long–range ordered magnets. However, they still provide important information regarding the nature of the magnetic state. Because the fields experienced by the muon are static, the relaxation rates are directly related to the (site averaged) magnitude of the local field. The order of magnitude of the RMS field at the muon site can be estimated by dividing the relaxation rate by $2\pi\gamma_\mu$, yielding the estimates of Table 6.7. If a particular muon site is assumed (or determined by measurement), these values of B_{RMS} could be used to estimate the magnitude of the moments for any proposed magnetic structure.

	Rate $[\mu s^{-1}]$	$B_{RMS}[G]$
Rb_1C_{60} (Fast)	2.6	30
Rb_1C_{60} (Slow)	0.08	1
Cs_1C_{60} (Fast)	2.5	29
Cs_1C_{60} (Slow)	0.2	2

Table 6.7: Estimates of the RMS field experienced by the muon at low temperature in the magnetic state of Rb_1C_{60} and Cs_1C_{60}.

In addition to the magnitude of the internal field, the form of the relaxation is qualitative information which, in combination with results from other techniques, may yield important clues to the magnetic structure. The most prominent characteristic feature of the observed ZF $\mu\mathcal{SR}$ relaxation in the all samples of the two magnetic phases (A = Cs and Rb) is its *two component nature*. The second most apparent feature is that the relaxation seems to develop quite gradually with temperature, and both the amplitudes and relaxation rates of the two components are temperature dependent.

In the NMR of Cs_1C_{60}, the ^{13}C lineshape is also distinctly two component, whereas

the ^{133}Cs line is not. The close analogy between the ^{13}C and the $\mu\mathcal{SR}$ suggests that the muon is sampling the static field distribution in the same way as the ^{13}C. While the sites of the μ^+ in these materials are currently a matter of speculation, the positions of the carbon atoms are not. It is possible, perhaps even likely, that the interstitial μ^+ is closely associated with the outer surface of the (distorted) C_{60}^-, lending support to the idea that the muon and carbon nuclei sample the same spatial distribution of magnetic fields. In addition both the AFMR and the NMR suggest some sort of antiferromagnetically (AF) ordered state, but whatever, the structure, it must be consistent with the lack of detectable magnetic neutron scattering[67]. Furthermore, if the two component nature is characteristic of the magnetic structure, and if the conclusion (found in NMR and AFMR) that the AF state is *spin–flopped* in fields exceeding ≈ 2.7T is correct, then the occurrence of two components must be independent of the direction of the moment, since the $\mu\mathcal{SR}$ is done in zero field.

The existence of two components indicates inhomogeneity of the sample. However, macroscopic inhomogeneity is ruled out by the one component nature of the magnetic broadening of the ^{133}Cs NMR line, so the inhomogeneity must be microscopic. One possible model of such inhomogeneity is that a fraction of the chains are magnetic, while the remainder are not, and the two kinds of chains are "intimately mixed" [218]. Variation with temperature of the amplitudes in this model could be due to a distribution of transition temperatures in the magnetic chains. For example, alkali occupancy and imperfect polymerization will lead to chains with a distribution of lengths (N), and perhaps T_c depends sensitively on N. If this is the case, then one would expect that all chains would possess a finite T_c, and at low temperature, if saturation of the fraction of magnetic chains to a value less than 1 occurs, that the saturation fraction would be sample dependent. The amplitudes, for A = Rb in high TF, appear to saturate at low temperature with $A_F \approx A_S$. In ZF, though, the saturation may not be complete by

the lowest temperature measured (2.5K). For A = Cs, the amplitudes appear to have saturated by 3K (with $A_F \approx A_S$). The similar temperature dependence of the amplitudes in a study by another group (on A = Cs) with saturation to equal amplitudes at low temperature[214] suggests that this is an intrinsic property of the magnetic state. It is perhaps possible that the magnetic structure is inhomogeneous in such a way that, for example, alternating chains are magnetically ordered and completely non–magnetic, but perhaps there exists another explanation that could be related to the well–established crystal structure of these materials.

If we assume all chains are equivalent, we must find the inhomogeneity of the field within a chain. There are two inequivalent *regions* of the distorted C_{60} molecule in the polymer, call them the *pole* and *equator* by analogy with the earth. The axis is just the chain direction, and the poles are where the isolated C_{60} molecular structure is most strongly modified (recall the carbons at the poles are sp^3). The Magic Angle Spinning NMR[60] indicates that there are as many as seven inequivalent carbons, but they can be grouped into the two categories above. Because the lattice constants are so *large*, the magnetic field in the magnetic state at any position in the unit cell will be dominated by the nearest few moments (because of the r^{-3} fall off of the dipolar field). In an antiferromagnet, cancellation of the internal fields between neighbouring oppositely aligned moments, leads naturally to a region of low field. Perhaps this region of low field can explain the presence of the slowly relaxing component. Initial modelling suggests that moments localized at the poles of the C_{60} would not lead easily to a region of low field at the surface of the molecule, but assuming a partially localized moment at the equator of the C_{60}, yields low fields in the polar region (see e.g. Fig. 6.43). Such a model may provide a fruitful avenue for further investigation. However, the gradual temperature dependence of the relative amplitudes of the two components is difficult to explain unless there is a distribution of transition temperatures.
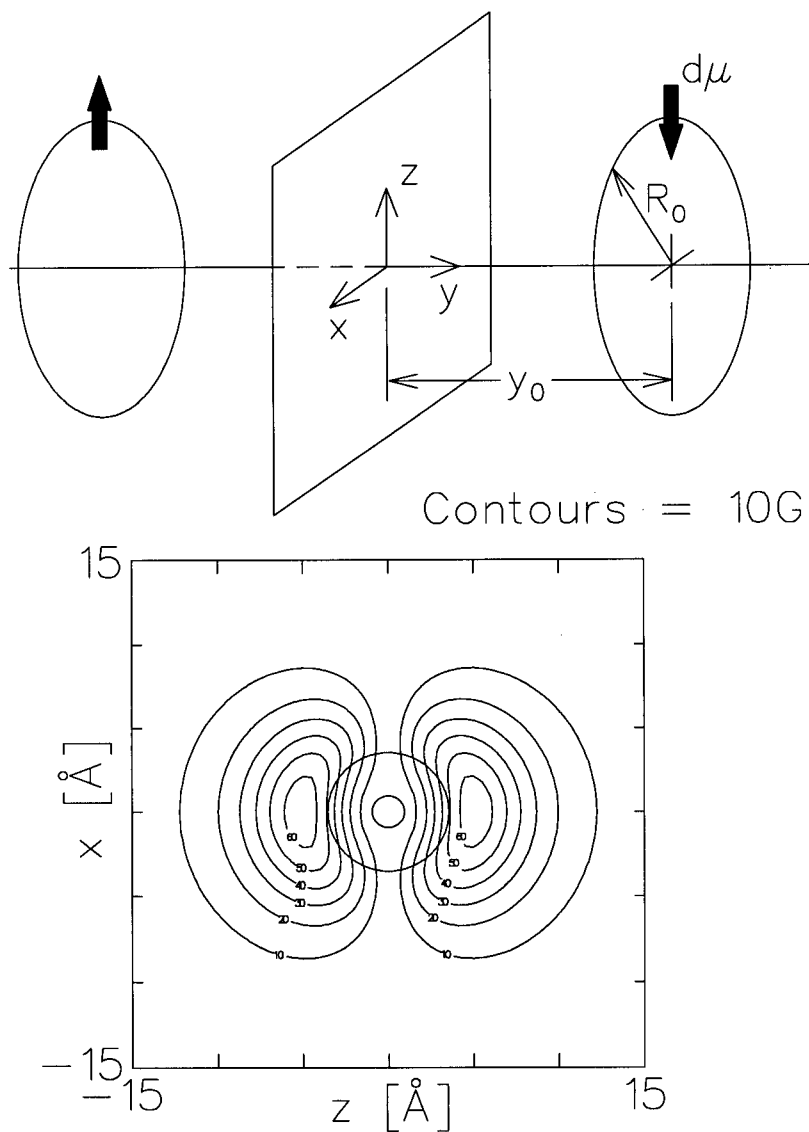
Figure 6.43: The field on a plane halfway between two (transverse) antiferromagnetically aligned moments delocalized on a ring of radius R_0 = 3.55Å(the C_{60} radius), pictured at the top. The moments are separated by $2y_0$ = 9.1Å(the chain lattice constant). The lower panel shows the contours of the magnitude of the net field. The outermost contour is 10G, and the contour spacing is 10G. Superimposed on the contour plot are two circles representing the cross section of the equator and pole regions of the distorted C_{60} molecule (to scale). Note that there is a pronounced "hole" in the field at the y axis, and this hole is on the order of the size of the polar region of the distorted C_{60} molecule.

6.3 Muonium in A_1C_{60}

Because of our experience in using endohedral muonium to probe the electronic prop-
erties of A_3C_{60} (Chapter 4), attempts were made [174] to find a similar signal in the
metallic polymer phases of A_1C_{60}. The presence of Mu is suggested by the missing frac-
tion $f_m \approx 15\%$ observed in transverse field in Rb_1C_{60} and K_1C_{60}, for $T < 250$K. No such
measurement has yet been attempted in Cs_1C_{60}.

A naive initial guess for the spin exchange rate of $Mu@C_{60}$ in A_1C_{60} is that it would
simply be scaled down by $g_N^2(0)$ (see Eq. (3.7)) for the lower conduction electron density
from the equivalent sized A_3C_{60} system at the same temperature. For free electrons,
$g_N \propto n^{1/3}$, so the spin–exchange rate would be scaled down by about $(1/3)^{1/6} \approx 0.8$
compared to the corresponding A_3C_{60} system. However, modifications to the electronic
structure due to polymerization and possibly electron–electron interactions will likely
alter this. Initial attempts to identify Mu by its spin exchange relaxation in LF (see
§3.1), using this guess as a rough guide, were unsuccessful[174]. In this section, further
investigation of Mu in the only non–magnetic A_1C_{60} system, K_1C_{60}, is reported. Before
discussing Mu, however, some remarks about the ZF $\mu\mathcal{SR}$ in K_1C_{60} are made.

In zero field, the relaxation in K_1C_{60} is nearly temperature independent, and con-
tains a small approximately exponential relaxation superimposed on a larger, very slowly
relaxing signal (see squares in Fig. 6.44). This relaxation has been fit with the sum of
an exponential and a slow Gaussian. The resulting relaxation rates are approximately
temperature independent and are shown shown in Fig. 6.45. The quenching (see Chap-
ter 5) of this relaxation at low temperature (Fig. 6.44) by very low longitudinal fields,
though, indicates that it is due to static fields. Taking the quenching of the relaxation as
a measure of the width of the random field distribution, ~ 5G, we estimate an early time
zero field exponential relaxation rate λ for diamagnetic muons sampling a Lorentzian

field distribution with $w = 5G$ (Eq. (5.4)) of $\lambda \approx \frac{4}{3} 2\pi\gamma_\mu w \approx 0.6\mu s^{-1}$ (see [174]). The

rough consistency of this estimate with the observed ZF relaxation rate (see circles in

Fig. 6.45) suggests that this signal is due to diamagnetic muons, and not to Mu [6]. The

origin of this signal is not clear. The magnitude of the internal fields is too large to be

due to nuclear dipoles. The exponential character of the relaxation suggests that it may

be due to a dilute spatial distribution of static moments, perhaps associated with chain

ends or other crystalline defects. Another possibility is the coexistence of some impurity

phase, but the presence of this small signal in the data of an experiment by another group

on a sample from a different source (described in [213]) suggests this is not the case.
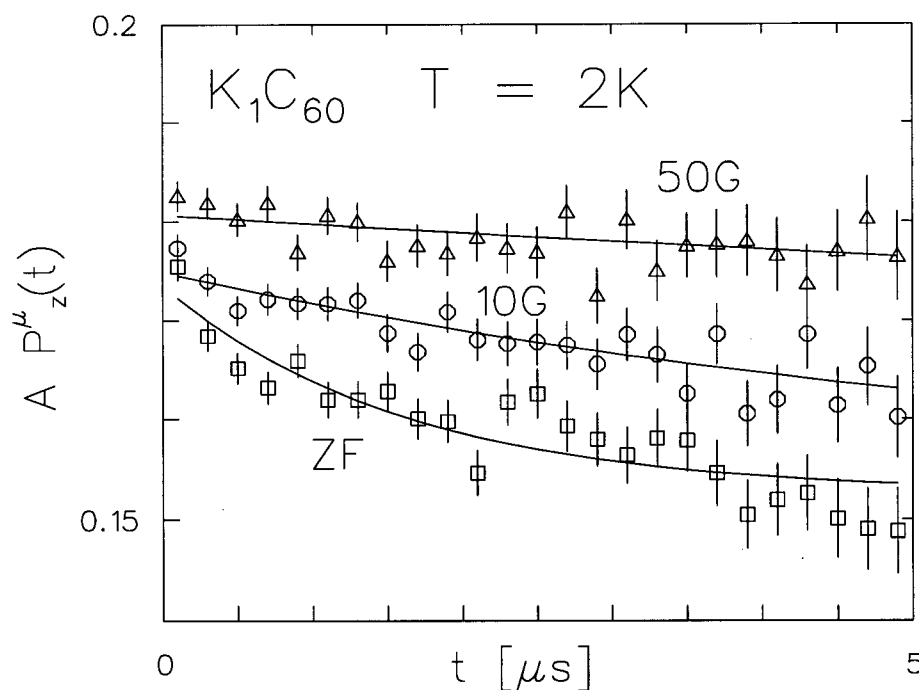
Figure 6.44: The ZF and low LF Relaxation in K_1C_{60}. The small amplitude fast exponential relaxation is attributed to μ^+. The quenching by low LF shows that the internal fields are static and very small, i.e. the distribution is narrower than 10G.

---

[6]The low field effective gyromagnetic ratio for Mu is about 100 times larger than γ_μ because of the bound electron moment.
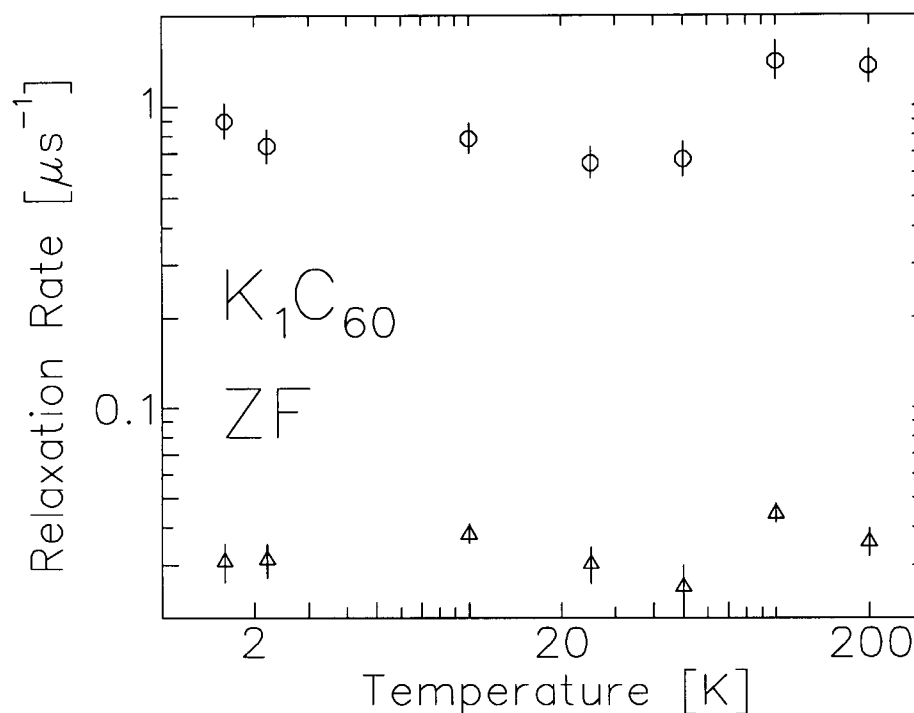
Figure 6.45: Temperature dependence of the relaxation rates in ZF in K_1C_{60}. The circles correspond to the fast exponential relaxation, while the triangles are Gaussian relaxation rates, and they are near the lower limit of measureable rates.

In an attempt to confirm that the origin of the missing fraction observed in low TF is muonium, decoupling curve measurements (of the Mu asymmetry as a function of applied LF, see Eq. (4.4)) were made. The LF asymmetry was found to increase from zero field, see Fig. 6.46. However, the behaviour is different from that of $Mu@C_{60}$ in Rb_3C_{60} (Fig. 4.15), with the inflection occuring at much lower fields. The two data sets are fit to the isotropic expression Eq. (4.4), which yields hyperfine parameters (A_μ) of 500(100)MHz at 2K and 1070(100)MHz at 250K. This indicates that the local environment of the Mu is not the same as in Rb_3C_{60}, and, furthermore, it is temperature dependent. The reduced hyperfine parameter (relative to A_μ in A_3C_{60}) is likely related to

the distortion of the C_{60} molecule associated with polymerization. Furthermore, the temperature dependence may be due to thermal motion of Mu within the cage. The decrease in A_μ below 50K for Mu in silicon has been explained in a similar manner (e.g. [96]).
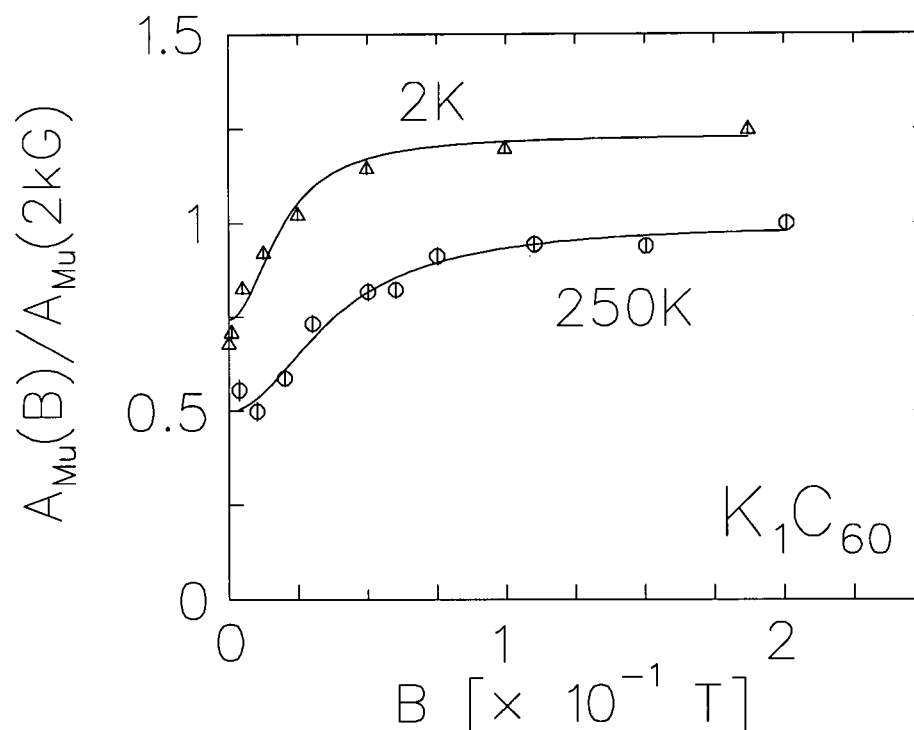
Figure 6.46: Decoupling curves of Mu in K_1C_{60} at 2K and 250K. The fits are to Eq. (4.4), and they yield isotropic hyperfine parameters of 500(100)MHz and 1070(100)MHz respectively. This behaviour is in contrast to that in Rb_3C_{60} (Fig. 4.15). The 2K curve is shifted up by 0.25 for clarity.

At 1kG LF, on the plateau of the decoupling curve where the asymmetry is high, a temperature scan of the very slow T_1 relaxation of Mu was made. The temperature dependence of the relaxation rate for an exponential relaxation with amplitude fixed from the low temperature decoupling curve is shown in Figure 6.47. The size of A_μ depends on the square of the Mu electron wavefunction at the muon, and thus is correlated with the spin exchange interaction J (or the spin exchange cross-section) which is determined

by the overlap of the Mu electron wavefunction with the neighbouring conduction band orbitals. In particular, though the detailed relationship between A_μ and σ is complicated, an increase in A_μ is associated with a decrease in σ. The relatively small A_μ together with the very slow T_1 relaxation suggest that, contrary to the case of A_3C_{60}, Mu in K_1C_{60} is in the *fast* spin exchange limit (see e.g. [80]). [7] Another characteristic of the fast spin exchange limit is field independence of the relaxation rate (in contrast to the slow limit Eq. (3.4)), which is observed in K_1C_{60} at both 250K and 2K for the LF range 0.01–0.2T. The spin exchange rate can remain in the fast limit over a wide range in temperature because the reduction of A_μ compensates for the reduction in the availability of free electrons at low temperature. Thus the temperature dependence of the relaxation rate at 0.1T (Fig. 6.47) is not simply the Korringa linear dependence due to free electrons but is the result of several competing factors: as T is reduced, i) the reduction of A_μ indicates that the spin–exchange cross–section is increasing; ii) the hyperfine period, which defines the timescale separating the fast and slow regimes is increasing; and iii) the number of conduction electrons within kT of the Fermi energy is decreasing. However, we note that the presence of the missing fraction (and the LF decoupling measurements, Fig. 6.46) are not readily explained in this picture, because in the fast spin–exchange limit, the hyperfine oscillations do not exist long enough to be averaged to zero (the origin of the missing fraction). One possible explanation for the persistence of a missing fraction in the fast spin–exchange regime is that the spin–exchange is delayed for a short period of time after the muon is implanted (on the order of the hyperfine period) before spin–exchange rate is established.

---

[7]Note that the observed relaxation is too slow to be explained easily by slow spin–exchange. The slope of $T_1(T)$ in the approximately linear region (Fig. 6.47) above 50K ($1.0(2) \times 10^{-3}\mu s^{-1}K^{-1}$) is much smaller than that observed in A_3C_{60}. For example, the value of the slope in K_3C_{60}, which is obtained from Fig. 4.14 by extrapolating down in field from 2T to 0.1T using Eq. (3.4), is about 7.0 $\mu s^{-1}K^{-1}$. Thus the spin exchange rate in K_1C_{60} would have to be $\sim 10^4$ times slower than in K_3C_{60}, which seems unreasonable.
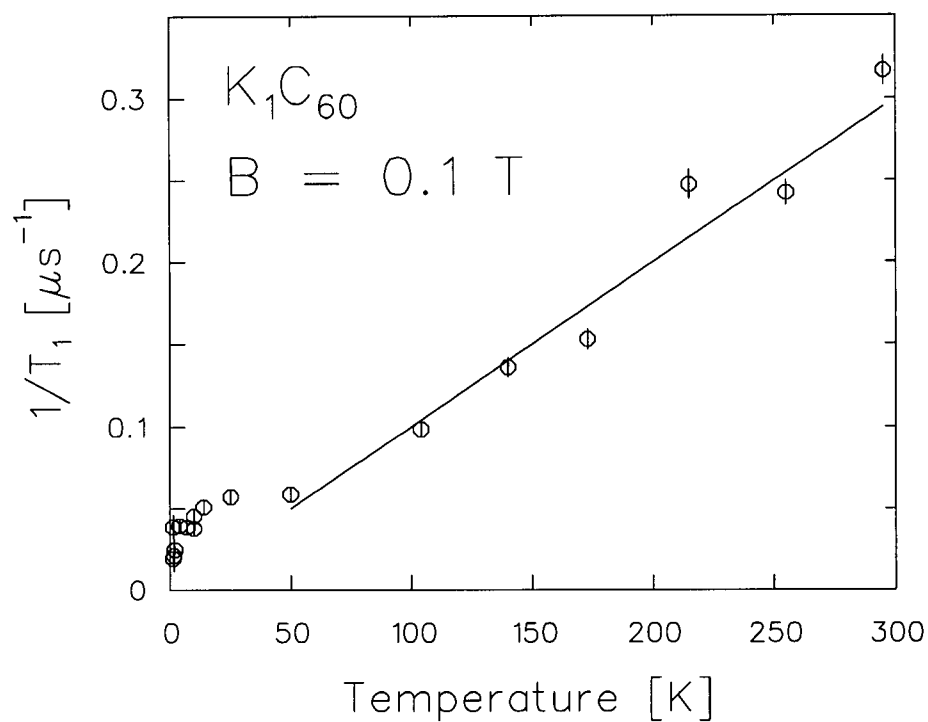
Figure 6.47: LF relaxation rate attributed to Mu@C_{60} undergoing *fast* spin–exchange with the conduction electrons in K_1C_{60}. The temperature dependence is *not* simply due to the Korringa mechanism as in A_3C_{60}, see text.

Chapter 7

Conclusions

7.1 A_3C_{60}

In conclusion we have observed the LF relaxation of $Mu@C_{60}$ in the A_3 superconductors. The temperature dependence of the relaxation rates exhibit Korringa behaviour above T_c and a small strongly field dependent coherence peak and strong activated behaviour in the superconducting state. The superconducting energy gap can be extracted from the low temperature behaviour, and the large uncertainty in its value is mainly due to uncertainty in the appropriate form of the temperature dependent superconducting DOS. For Rb_3 and K_3 and the range of models considered, the reduced gap $2\Delta/kT_c$ lies in the range 3–5. However, for consistency between the high and low field temperature dependences, a weakly temperature dependent broad DOS is favoured, and the reduced gap values lie between 3.2 and 4.0. The upper end of this range as well as the broad low temperature DOS peaks are consistent with the tunneling and optical results of Koller.[202] The small size of the peak can be due to one or several factors, such as the moderately strong electron–phonon coupling suggested, for example, by tunneling.[202, 205] Following Pennington and Stenger[102] we conclude that, provided the results of Akis[131] carry over directly to the case of A_3C_{60}, which possesses a very broad and complicated phonon spectrum, the small size of the 1.5 T coherence peak implies $T_c/E_{log} \approx 0.2$. A ratio as large as this is incompatible with the near weak–coupling value of the energy gap which gives[202] $T_c/E_{log} < 0.1$. Thus strong–coupling alone will not consistently account for

the both the small coherence peak and the gap. Together with the strong field dependence of the coherence peak, this suggests that an additional coherence peak suppression mechanism connected with the inhomogeneous vortex state must be present. A full explanation of such an effect would require extension of the theories discussed in section IV.D[150, 153] to the regime of strong–coupling.

In transverse field we find broadening of the μSR precession line due to the inhomogeneous fields of the vortex state. There is no clear flux lattice lineshape, so we can only estimate the magnitude of λ, which for example in Rb$_3$ lies in the range 3000 – 7000 Å . This range is definitely inconsistent with the values of Chu and McHenry[94], and this discrepancy is likely due, not to sample dependence of λ, but rather to the systematic differences between the two techniques.

The weaker activated dependence in s–Na$_2$Cs is likely due to coexistence of the ns–Na$_2$Cs phase. Quench–rate dependent experiments may be able to clarify this and allow measurement of the properties of both phases. By comparing the coherence peak in Fm$\bar{3}$m materials with s–Na$_2$Cs, we find no evidence for an effect on the coherence peak due to the degree of molecular order. In the Fm$\bar{3}$m materials, quench rate dependence would also help to clarify the role of frozen orientational disorder in the value of λ and in the residual low temperature T_1 relaxation.

Finally we note that there are interesting aspects of Mu@C$_{60}$ in A$_3$ such as its stability and very weak interaction with the conduction band that suggest further theoretical invesitagtion of the detailed properties of endohedral fullerene species.

7.2   A$_1$C$_{60}$

The first observation of Mu in a metallic system (K$_1$C$_{60}$) other than the A$_3$C$_{60}$ materials is reported here for the first time. The structure of the Mu centre is different than

the endohedral centre in A_3C_{60}, with a smaller temperature independent hyperfine parameter. To clarify the details of the structure of Mu in this system, more measurements are required. A better understanding of the hyperfine structure may aid in explanation of the T_1 relaxation of Mu in this system, which is remarkably slow compared to the A_3C_{60} systems.

In the magnetic state of A_1C_{60} (A = Rb, Cs), the static nature of the internal fields has been confirmed. A rapidly damped oscillation in the ZF spectra at the lowest temperatures in Cs_1C_{60} is the first evidence from $\mu S \mathcal{R}$ that there is magnetic order in the low temperature state. It is, however, not possible from this data to make any conclusion as to the form of the magnetic structure. A phenomenological form was used to parametrize the magnetic relaxation. The features apparent in the data are:

1. The two component nature of the relaxation at low temperature;

2. The amplitudes *and* relaxation rates of the two components change with temperature;

3. In Rb_1C_{60}, the amplitudes haven't saturated by 2.5K in ZF, but they seem to have in high TF as well as in ZF in Cs_1C_{60};

4. The saturation of the low temperature amplitudes is to roughly equal amplitudes for the fast and slow components;

5. The transition is quite broad and the temperature dependence is quite gradual.

This list of features of the relaxation in the magnetic state may be due to microscopic inhomogeneity in the magnetic state. An alternative interpretation has been suggested to explain this behaviour: the inhomogeneity may be a characteristic of a homogeneous magnetic state in conjunction with the manner in which the muons sample the internal

fields. The similarity of the $\mu\mathcal{SR}$ relaxation and the ^{13}C NMR spectrum in the magnetic state may be due to a similar sampling of the field distribution. The presence of a spin–flop transition in Rb_1C_{60}, may be related to the change in the relative magnitudes of the fast and slow components which occurs at fields less than 1T.

Bibliography

[1] H.W. Kroto *et al*, Nature **318**, 162 (1985).

[2] R.F. Curl, RMP **69**, 691 (1997);
H.W. Kroto, RMP **69**, 703 (1997);
R.E. Smalley, RMP **69**, 723 (1997).

[3] W. Krätchmer *et al*, Nature **347**, 354 (1990).

[4] M.S. Dresselhaus, G. Dresselhaus & P.C. Ecklund, *Science of Fullerenes and Carbon Nanotubes*, (Academic, San Diego, 1996).

[5] R.C. Haddon, Acc. Chem. Res. **25**, 127 (1992).

[6] M.P. Gelfand, Superconductivity Review **1**, 103 (1994).

[7] O. Gunnarsson, RMP **69**, 575 (1997).

[8] D.S. Bethune *et al*, Nature **366**, 123 (1993).

[9] M. Saunders *et al*, J. Am. Chem. Soc. **116**, 2193 (1994).

[10] T. Almeida Murphy *et al*, PRL **77**, 1075 (1996).

[11] E.J. Ansaldo *et al*, Nature **353**, 121 (1991).

[12] A. Oshiyama *et al* in *The Fullerenes*, Kroto, Fischer & Cox eds. (Pergamon, Oxford, 1993).

[13] J.H. Weaver in *The Fullerenes*, Kroto, Fischer & Cox eds. (Pergamon, Oxford, 1993).

[14] R.F. Kiefl *et al*, PRL **69**, 2005 (1992).

[15] M.J. Rosseinsky in *Physics and Chemistry of the Fullerenes*, K. Prassides ed. (Kluwer, Amsterdam?, 1994).

[16] D.C. Mattis, *The Theory of Magnetism*, (Springer, Berlin, 1981).

[17] M. Knupfer & J. Fink, PRL, forthcoming (1997).

[18] S. Kagoshima *et al*, *One–Dimensional Conductors* (Springer, Berlin, 1988);

[19] A.W. Overhauser, PRL **4**, 462 (1960).

[20] N.W. Ashcroft & N.D. Mermin, *Solid State Physics* (Saunders College, Philadelphia, 1976).

[21] E. Fawcett, RMP **60**, 209 (1988).

[22] E. Fawcett, RMP **66**, 25 (1994).

[23] L.P. Le *et al*, PRB **48**, 7284 (1993).

[24] C. Kittel, *Introduction to Solid State Physics, 6th Edition* (Wiley, New York, 1986).

[25] P. Breusch, *Phonons: Theory and Experiments I*, (Springer, Berlin, 1982).

[26] P.A. Heiney in *The Fullerenes*, Kroto, Fischer & Cox eds. (Pergamon, Oxford, 1993).

[27] A.M. Rao *et al*, Science **259**, 955 (1993).

[28] C. Goze *et al*, PRB **54**, R3676 (1996).

[29] R.C. Haddon, *et al*, Nature **350**, 320 (1991).

[30] A.F. Hebard, *et al*, Nature **350**, 600 (1991).

[31] A.P. Ramirez, Superconductivity Review **1**, 1 (1994).

[32] K. Holczer & R.L. Whetten in *The Fullerenes*, Kroto, Fischer & Cox eds. (Pergamon, Oxford, 1993).

[33] K. Tanigaki & O. Zhou, J. Phys. I (France) **6**, 2159 (1996).

[34] C.H. Pennington & V.A. Stenger, RMP, **68**, 855 (1996).

[35] G. Zimmer, *et al*, Appl. Magn. Reson. **11**, 263 (1996).

[36] V. Buntar & H.W. Weber, Supercond Sci. Technol. **9**, 599 (1996).

[37] M. Schlüter *et al* in *The Fullerenes*, Kroto, Fischer & Cox eds. (Pergamon, Oxford, 1993).

[38] R.E. Walstedt *et al*, Nature **362**, 611 (1993).

[39] O. Zhou *et al*, PRB **52**, 483 (1995).

[40] J.E. Fischer, private communication (1995).

[41] T.T.M. Palstra *et al*, Solid State Comm. **93**, 327 (1995).

[42] J. Bardeen, L.N. Cooper & J.R. Schrieffer, Phys. Rev. **108**, 1175 (1957).

[43] K. Prassides *et al*, Science **263**, 950 (1994).

[44] K. Tanigaki *et al*, PRB **49**, 12307 (1994).

[45] K. Prassides *et al*, J. Am. Chem. Soc. **119**, 834 (1997);
L. Christofolini *et al*, Chem. Commun., 375 (1997).

[46] Q. Zhu, PRB **52**, R723 (1995).

[47] J.E. Schirber, Physica C **260**, 173 (1996).

[48] E.J. Mele & S.C. Erwin, PRB **50**, 2150 (1994).

[49] D.J. Scalapino in *Superconductivity, Vol. 1*, ed. R.D. Parks (Dekker, New York, 1969).

[50] G.M. Eliashberg, Sov. Phys. JETP **11**, 696 (1960).

[51] W.L. McMillan & J.M. Rowell in *Superconductivity, Vol. 1*, ed. R.D. Parks (Dekker, New York, 1969).

[52] J.P. Carbotte, RMP **62**, 1027 (1990).

[53] P. Morel & P.W. Anderson, Phys. Rev. **125**, 1263 (1962).

[54] C.F. Richardson & N.W. Ashcroft, PRB **55**, 15310 (1997).

[55] S. Chakravarty & S. Kivelson, Europhys. Lett. **16**, 751 (1991).

[56] W. Victoroff & M. Héritier, J. Phys. I (France) **6**, 2175 (1996).

[57] Q. Zhu *et al*, PRB **47** 13948 (1993).

[58] R. Tycko *et al*, PRB **48**, 9097 (1993).

[59] P.W. Stephens *et al*, Nature **370**, 636 (1994).

[60] K.-F. Thier *et al*, PRB **53**, R496 (1996);
H. Alloul *et al*, PRL **76**, 2922.

[61] P. Petit *et al*, PRB **51**, 11924 (1995);
M. Kosaka *et al*, PRB **51**, 12018 (1995);
G. Oszlányi *et al*, PRB **51**, 12228 (1995).

[62] M.C. Martin *et al*, PRB **49**, 10818 (1994).

[63] F. Bommeli *et al*, PRB **51**, 14791 (1995).

[64] V. Brouet *et al*, PRL **76**, 3638 (1996).

[65] L.S. Smith *et al*, Sol. St. Comm. **19**, 377 (1976).

[66] O. Chauvet *et al*, PRL **72**, 2721 (1994).

[67] J.E. Fischer, private communication (1997).

[68] J. Kanamori in *Magnetism Vol. 1*, Rado & Suhl eds. (Academic, New York, 1963);

[69] R.M. White, *Quantum Theory of Magnetism*, (Springer, Berlin, 1983).

[70] A. Jánossy *et al*, PRL, forthcoming (1997).

[71] S.C. Erwin *et al*, PRB **51**, 7345 (1995).

[72] P.R. Surján *et al*, Solid State Comm. **92**, 407 (1993);
K. Tanaka *et al*,Solid State Comm. **93**, 163 (1995);
S. Stafström *et al*, Europhys. Lett. **30**, 295 (1995).

[73] P. Auban–Senzier *et al*, J. Phys. I (France) **6**, 2181 (1996).

[74] E.J. Mele *et al*, PRB **52**, 12493 (1995).

[75] A. Schenck, *Muon Spin Rotation Spectroscopy*, (Hilger, Bristol, 1985).

[76] S.F.J. Cox, J. Phys. C **20**, 3187 (1987).

[77] J.H. Brewer, Encyclopedia of Applied Physics, **11**, 23 (1994).

[78] G. Schatz & A. Weidinger, *Nuclear Condensed Matter Physics*, (Wiley, New York, 1996).

[79] T.M. Riseman, Ph.D. Thesis, University of British Columbia, 1993, unpublished.

[80] K.H. Chow, Ph.D. Thesis, University of British Columbia, 1994, unpublished.

[81] G.M. Luke, Ph.D. Thesis, University of British Columbia, 1988, unpublished.

[82] D.M. Garner, Ph.D. Thesis, University of British Columbia, 1979, unpublished.

[83] R.L. Garwin, L.M. Ledermann & M. Weinrich, Phys. Rev. **105**, 1415 (1957).

[84] L.M. Ledermann with D. Teresi, *The God Particle: if the universe is the answer, what is the question?*, (Houghton Mifflin, Boston, 1993).

[85] R.F. Kiefl *et al*, PRL **70**, 3987 (1993).

[86] J.W. Schneider *et al*, PRL **71**, 557 (1993).

[87] S. Pekker *et al*, Science **265**, 1077 (1994).

[88] O.V. Lounasmaa, *Experimental Principles and Methods Below 1K*, (Academic, New York, 1974).

[89] R.H. Heffner *et al*, Hyp. Int. **106**, 271 (1997).

[90] N.B. Hannay *et al*, PRL **14**, 225 (1965).

[91] T. Yildirim *et al*, PRL **77**, 167 (1996).

[92] Q. Zhu, PRB **52**, R723 (1995).

[93] C.L. Lin *et al*, PRB **49**, 4285 (1994).

[94] S. Chu & M.E. McHenry, PRB **55**, 11722 (1997).

[95] Y. Yoshinari *et al*, PRB **54**, 6155 (1996).

[96] B.D. Patterson, RMP **60**, 69 (1988).

[97] J. Korringa, Physica **16**, 601 (1950).

[98] C.P. Slichter, *Principles of Magnetic Resonance*, (Springer, Berlin, 1990).

[99] L.C. Hebel & C.P. Slichter PR **113**, 1504 (1959).

[100] J.A. Chakhalian *et al*, Hyp. Int. **106**, 245 (1997).

[101] T.M.S. Johnstone *et al*, Hyp. Int. **106**, 71 (1997).

[102] C.H. Pennington & V.A. Stenger, RMP **68**, 855 (1996).

[103] Y. Maniwa *et al*, J. Phys. Soc. Jpn., **63**, 1139 (1994).

[104] Y.N. Molin *et al*, *Spin Exchange*, (Springer,Berlin,1980).

[105] V.G. Nosov & I.G. Yakovleva, Sov. Phys. JETP **16**, 1236 (1963). M. Senba, J. Phys. B **24**, 3531 (1991).

[106] K.H. Chow *et al*, PRB **50**, 8918 (1994).

[107] R.F. Kiefl *et al*, PRL **68**, 1347 & 2708 (1992).

[108] M. Tinkham, *Introduction to Superconductivity*, (McGraw–Hill, New York, 1996).

[109] D.E. MacLaughlin, Solid State Physics **31**, 1, (1976).

[110] P.J. Hirchfeld & N. Goldenfeld, PRB **48**, 4219 (1993).

[111] J. Halbritter, Z. Phys. **243**, 201 (1971).

[112] B. Muhlschlegel, Z. Phys. **155**, 313 (1959).

[113] G. Preosti *et al*, PRB **50**, 1259 (1994).
      R. Fehrenbacher & M.R. Norman, PRB **50**, 3495 (1994).

[114] H. Monien & D. Pines, PRB **41**, 6297 (1990).

[115] J. Annett, *et al* in *The Physical Properties of High Temperature Superconductors*, *Vol. 2*, D.M. Ginsberg ed. (World Scientific,Singapore,1990), p571.

[116] C.H. Pennington & C.P.Slichter in *The Physical Properties of High Temperature Superconductors, Vol. 2*, D.M. Ginsberg ed. (World Scientific,Singapore,1990), p269.

[117] J.A. Martindale *et al*, PRL **68**, 702 (1992).

[118] K. Asayama *et al*, J. Mag. Mag. Mater. **76–77**, 449 (1988).

[119] D.E. MacLaughlin *et al*, PRL **53**, 1833 (1984).

[120] M. Takigawa *et al*, J. Phys. Soc. Jpn. **56**, 873 (1987).

[121] L.C. Hebel PR **116**, 79 (1959).

[122] R.C. Dynes *et al*, PRL **41**, 1509 (1978).

[123] P.B. Allen & D. Rainer, Nature **349**, 396 (1991).

[124] J.P. Carbotte, RMP **62**, 1027 (1990).

[125] D.J. Scalapino in *Superconductivity, Vol. 1*, ed. R.D. Parks (Dekker, New York, 1969).

[126] J.R. Schrieffer *et al*, PRL **10**, 336 (1963).

[127] S.B. Kaplan *et al*, PRB **14**, 4854 (1976).

[128] M. Fibich, PRL **14**, 561 & 621 (1965).

[129] D.J. Scalapino & T.M. Wu, PRL **17**, 315 (1966).

[130] B. Statt, PRB **42**, 6805 (1990).

[131] R. Akis *et al*, Physica C **176**, 485 (1991).

[132] H.-Y. Choi & E.J. Mele, PRB **52**, 7549 (1995).

[133] A. A. Abrikosov & L.P. Gor'kov, Sov. Phys JETP **12**, 1243 (1961).

[134] A. Griffin & V. Ambegaokar in *Low Temperature Physics, LT9A*, J.G. Daunt *et al* eds., (Plenum, New York, 1965).

[135] Y. Masuda & M. Hashimoto, J. Phys. Soc. Jpn. **31**, 1661 (1971).

[136] K. Kumagai *et al* in *Ternary Superconductors*, Shenoy, Dunlap & Fradin eds., (Elsevier, Amsterdam, 1981), p. 185.

[137] Y. Iwasa *et al*, PRB **53**, R8836 (1996).

[138] C.M. Brown *et al* in *Recent Advances in the Chemistry and Physics of Fullerenes, Vol. 4*, K.M. Kadish & R.S. Ruoff eds., in press (1997).

[139] K. Prassides *et al*, Physica C, in press (1997).

[140] A.L. Fetter and P.C. Hohenberg in *Superconductivity, Vol. 2*, ed. R.D. Parks (Dekker, New York, 1969).

[141] Daniel S. Fisher *et al*, Phys. Rev. B **43**, 130 (1991).

[142] P.G. deGennes, *Superconductivity of Metals and Alloys*, (W.A. Benjamin, New York, 1966).

[143] U. Brandt *et al*, Z. Phys. **201**, 209 (1967).

[144] U. Brandt, Phys. Lett. **27A**, 645 (1968).

[145] K. Maki in *Superconductivity, Vol. 2*, ed. R.D. Parks (Dekker, New York, 1969).

[146] V. Ambegaokar & A. Griffin, Phys. Rev. **137**, A1151 (1965).

[147] A. Wasserman & M. Springford, Adv. Phys. **45**, 471 (1996).
M. Springford & A. Wasserman, J. Low Temp. Phys. **105**, 273 (1996).

[148] V. Ambegaokar in *Superconductivity, Vol. 1*, ed. R.D. Parks (Dekker, New York, 1969).

[149] C. Caroli *et al*, Phys. Lett. **9**, 307 (1964).

[150] M. Cyrot, Phys. Kondens. Mat. **3**, 374 (1965).

[151] F. Gygi & M. Schluter, Phys. Rev. B **43**, 7609 (1991).

[152] D. Rainer *et al*, PRB **54**, 10094 (1996).

[153] R.J. Watts–Tobin *et al*, J. Low Temp. Phys. **17**, 71 (1974).

[154] W. Pesch & L. Kramer, J. Low Temp. Phys. **15**, 367 (1974);
L. Kramer & W. Pesch, Z. Phys. **269**, 59 (1974).

[155] B. Pöttinger & U. Klein, PRL **70**, 2806 (1993).

[156] M. Ichioka *et al*, Phys. Rev. B **55**, 6565 (1997).

[157] B.S. Chandrasekhar, App. Phys. Lett. **1**, 7 (1962).
A.M. Clogston, Phys. Rev. Lett. **9**, 266 (1962).

[158] D. Saint-James, E.J. Thomas, and G. Sarma, *Type II Superconductivity*, (Pergamon, Oxford, 1969).

[159] N.R. Werthamer *et al*, Phys. Rev. **147**, 295 (1966).

[160] M. Cyrot, J. de Phys. (Paris), **27**, 283 (1966).

[161] Y. Masuda & N. Okubo, J. Phys. Soc. Jpn **26**, 309 (1969).

[162] D. Eppel *et al*, Z. Phys. **197**, 46 (1966).
W. Pesch, Phys. Lett. **28A**, 71 (1968).

[163] B.G. Silbernagel *et al*, Phys. Rev. Lett **17**, 384 (1966).

[164] W. Fite II & A.G. Redfield, Phys. Rev. **162**, 358 (1967).

[165] I.B. Goldberg & M. Weger, J. Phys. Soc. Jpn. **24**, 1279 (1968).

[166] L. Xing & Y-C. Chang, Phys. Rev. Lett. **73**, 488 (1994).

[167] E. Ehrenfreund *et al*, Sol. St. Comm. **7**, 1333 (1969).
L.N. Bulaevskii *et al*, Phys. Rev. Lett. **71**, 1891 (1993).
C.H. Recchia *et al*, Phys. Rev. Lett. **78**, 3543, (1997).

[168] A.Z. Genack & A.G. Redfield, Phys. Rev. Lett. **31**, 1204 (1973).

[169] Orsay Group on Superconductivity, Colloque Ampere **XIV**, 320, (1967).

[170] F.Y. Fradin in *Nuclear and Electron Resonance Spectroscopies Applied to Materials Science*, Kaufman and Shenoy eds., (Elsevier, Amsterdam, 1981).

[171] R. Kadono *et al*, PRL **79**, 107 (1997).

[172] T.L. Duty *et al*, Hyp. Int. **86**, 789 (1994).

[173] S.K. Estreicher *et al*, Chem. Phys. Lett. **196**, 311 (1992);
P.W. Percival & S. Wlodek, Chem. Phys. Lett. **196**, 317 (1992).

[174] W.A. MacFarlane, PRB **52**, R6995 (1995).

[175] E.J. Ansaldo *et al*, Nature **353**, 129 (1991).

[176] E. Holzschuh, Helv. Phys. Acta **54**, 552 (1981).

[177] E.J. Mele & S.C Erwin, PRB **50**, 2150 (1994).

[178] J. Mizuki *et al*, PRB **50**, 3466 (1994).

[179] V. Jaccarino in *Proceeding of the International School of Physics "Enrico Fermi"*,
XXXVII, W. Marshall ed., (Academic, New York, 1967), p. 365.

[180] V.A. Stenger *et al*, PRL **74**, 1649 (1995).

[181] Y. Maniwa *et al*, PRB **52**, R7054 (1995).

[182] R. Tycko *et al*, PRL **68**, 1912 (1992).

[183] B.S. Shastry & E. Abrahams, PRL **72**, 1933 (1994).

[184] Y.J. Uemura *et al*, Nature **352**, 605 (1991).

[185] Y.J. Uemura *et al*, Physica C **235–240**, 2501 (1994).

[186] W.A. MacFarlane *et al*, Hyp. Int. **86**, 467 (1994).

[187] E.H. Brandt, PRB **37**, 2349 (1988).

[188] B. Pumpin *et al*, PRB **42**, 8019 (1990).

[189] T.M. Riseman *et al*, PRB **52**, 10569 (1995).

[190] J.E. Sonier, M.Sc. Thesis, University of British Columbia (1994), Unpublished.

[191] J.R. Clem, J. Low Temp. Phys. **18**, 427 (1975).

[192] Z. Hao *et al*, PRB **43**, 2844 (1991).

[193] A. Yaouanc *et al*, PRB **55**, 11107 (1997).

[194] J.E. Sonier *et al*, PRL **72**, 744 (1994).

[195] J.E. Sonier *et al*, PRL, forthcoming; preprint: cond–mat/9708115.

[196] J.E. Sonier *et al*, PRL **79**, 1742 (1997).

[197] G. Zimmer *et al*, PRB **54**, R3768 (1996).

[198] L.Degiorgi *et al*, PRL **69**, 2987 (1992).

[199] J.E. Sonier *et al*, PRB **55**, 11789 (1997).

[200] K. Tanigaki *et al*, PRB **49**, 12307 (1994).

[201] C. Christides *et al*, PRB **46**, 12088 (1992).

[202] D. Koller *et al*, PRL **77**, 4082 (1996).

[203] Z. Zhang *et al*, Science **254**, 1619 (1991).

[204] P. Jess *et al*, Physica C **235–240**, 2499 (1994).

[205] J. Ostrick, to be published.

[206] S.K. Watson *et al*, PRB **55**, 3866 (1997).

[207] A. Yazdani *et al*, Science **275**, (1997).

[208] G.M. Kalvius, "μ^+SR in Metallic Magnets" lecture notes from the $\mu\mathcal{SR}$ Summer School, Maui, USA (1993), unpublished.

[209] A. Abragam, *The Principles of Nuclear Magnetism*, (Oxford,London,1961).

[210] R.S. Hayano *et al*, PRB **20**, 850 (1979).

[211] Y.J. Uemura *et al*, PRL **73**, 3306 (1994).

[212] Y.J. Uemura *et al*, PRB **52**, R6991 (1995).

[213] M. Larkin *et al*, Hyp. Int. **104**, 325 (1997).

[214] L. Christofolini *et al*, J. Phys.: Condens. Matter **7** L567 (1995).

[215] C.M. Brown in *The Annual Report of the Paul Scherrer Institute, Ann. I*, p39 (1996).

[216] A. Lappas *et al*, Science **267** 1799 (1995).

[217] J.E. Fischer & P.W. Stephens, private communication (1997).

[218] V. Brouet, private communication (1997).

Appendix A: Relevant Alkali Nuclear Moments

Isotope	spin [$\hbar$]	μ [μ_N]	Abundance [%]	A-H d [Å]	μ/d^3 [μ_NÅ^{-3}]
^{23}Na	3/2	2.2161	100	1.8873	0.3297
^{39}K	3/2	0.39097	93.10	–	–
^{40}K	4	-1.296	1.18	–	–
^{41}K	3/2	0.21459	6.88	–	–
K$_{avg}$	–	0.394	–	2.24	0.0351
^{85}Rb	5/2	1.3482	72.15	–	–
^{87}Rb	3/2	: 2.7414	27.85	–	–
Rb$_{avg}$	–	1.736	–	2.367	0.3099
^{133}Cs	7/2	2.56422	100	2.494	0.1653

Table A.1: Nuclear moments of the alkali metals, and the alkali hydride bond length. If the μ^+ is closely associated with a single alklai ion, one might expect that the normal state TF linewidth would scale with the average nuclear dipolar field μ/d^3.

Appendix B: Details of Sample Mounting

For the benefit of anyone planning to use $\mu S\mathcal{R}$ on alkali fullerides or similar air–sensitive materials and to make a complete description of sample handling and mounting procedures employed in the experiments on which this thesis is based, a detailed description of the various sample cells is given below.

Initial sample cells employed the low background technique using a cup shaped veto counter behind the sample[86]. This was necessary in order to obtain an acceptable signal to noise ratio from the small quantities of material that were available at the time. In such a cell, the sample, a lightly pressed pellet wrapped in thin Al foil, was stuck to a thin aluminized mylar (0.5 thou. thick) sheet with silicone vacuum grease. The aluminized mylar sheet was held taught (like a drumskin) in the cylindrical cell cavity by a thin Al ring. The cell (shop aluminum) was equipped with Kapton windows in front and behind the sample, so that μ^+ entering the cell and not stopping in the sample would exit throught the back window and trigger the veto cup. The window seals were made by crushing an indium o–ring in a rectangular groove of cross–sectional area slightly smaller than the In wire. The actual seal was made in the area on either side of the groove. Because the sealing area was too large, this groove design lead to loss of integrity of the cell. Subsequent cells did not employ this low background technique because material was available in sufficient quantity that the entire muon beam could be stopped in the sample. In the new cell, the groove design was improved in the following way: a triangular groove (of cross–sectional area appropriate to the In o–ring thickness) was used, and the groove was flanked on either side by a relieved area (10 thou. higher than the surrounding surface) about 1mm wide. The relieved area provided the sealing area, where the In

would be pressed very thin, the crushing force of the screws being concentrated on this area. Excess In would flow beyond the relieved region and not interfere. Note that it is imperative that the edges of such cells that come into contact with the Kapton window(s) be smooth (usually "radiused" at about 1mm). This is because the window flexes against these edges as the pressure gradient across the window varies during the course of an experiment, and any roughness may puncture the Kapton.

Nearly all the cells employed standard #4–40 hex socket head 18-8 stainless steel screws to provide the sealing force. Concerns about magnetism at low temperature in the screws led us to commission the manufacture of Al–bronze non–magnetic socket head screws. The socket head is the preferred type for use in inert atmosphere gloveboxes where thick gloves make handling of other screw types difficult (and dangerous for the glovebox integrity). Furthermore, it is easier to get a large torque on such screws. It should be noted that with such small screws it was found (even for the stainless steel) that it is easy to apply enough torque with a standard Allan key to shear the socket heads off. The screw itself, and not the threads in the Al cell, is the weakest point in this case. Concern over the relative weakness of the bronze screws led us to use stainless screws to crush the o–ring, and subsequently replace the screws one–by–one with the bronze screws. Significant improvements to this process could be made by using a small press to crush the In o–ring. With a jig appropriate to the cell, one could, while maintaining pressure in the press, insert the bronze screws.

To avoid temperature dependent background signals from muons stopping in Al, whenever any of the non–low background cells were used, a 0.25 mm thick high purity silver mask (99.9985% Ag, Goodfellow) was attached to the front of the Al vessel. Furthermore, before the sample was loaded, a similar silver backing was installed in the back of the sample cavity. In all cases the samples were contained in Al foil sufficiently thin to stop very few muons.

We note that nearly all the experiments described in this thesis were conducted in a He gas flow cryostat. The sample thermometry (e.g. Lakeshore calibrated carbon glass resistor or diode thermometers) in some cases was about 2cm from the sample, but in others was placed in blank holes in the back of the sample vessel. Thermal gradients in the gas flow cryostat were not significant as the difference between the sample and He diffuser thermometry indicated. The cells for two exceptional experiments not conducted in such a cryostat are described below.

For the high temperature cell, the considerable expertise of the TRIUMF machine shop was employed in manufacturing a cell from 99.9% (Johnson–Matthey) Ag with a welded 1 thou. Ag foil window. The sample was loaded into the cell cavity via an annealed oxygen–free Cu tube, Ag–soldered into the rear of the cell. After the cell was filled, the tube was sealed by crimping the tube. It was found that the tube (1/8" outer diameter) was inconveniently small for loading and unloading the sample in a glovebox. The cell was also equipped with a blank hole in the rear where a Pt resistor thermometer was placed during the experiment.

Spatial constraints in the Oxford Instruments Model 400 Top Loading Dilution Refridgerator (DR) are such that sealing a window with an In o–ring is impractical. Thus a cell using an epoxied Kapton window was designed (see Fig. B.1). The (99.9% Ag) cell was sealed with an In o–ring seal and a plug held in place with four #2–56 screws (again using stainless first, then replacing them with bronze). A c–clamp and jig was also used to provide crushing force on the thin (typically 20 thou. diameter) In o–ring. The powdered samples were introduced into the cell cavity in thin (0.3 thou.) Al foil packets.

Gluing such a window presented many difficulties. The best method found is as follows: The epoxied surfaces (Ag and Kapton) are sandblasted (the Kapton widow can be masked with scotch tape) and cleaned with methanol. A cryogenic epoxy (e.g. Industial
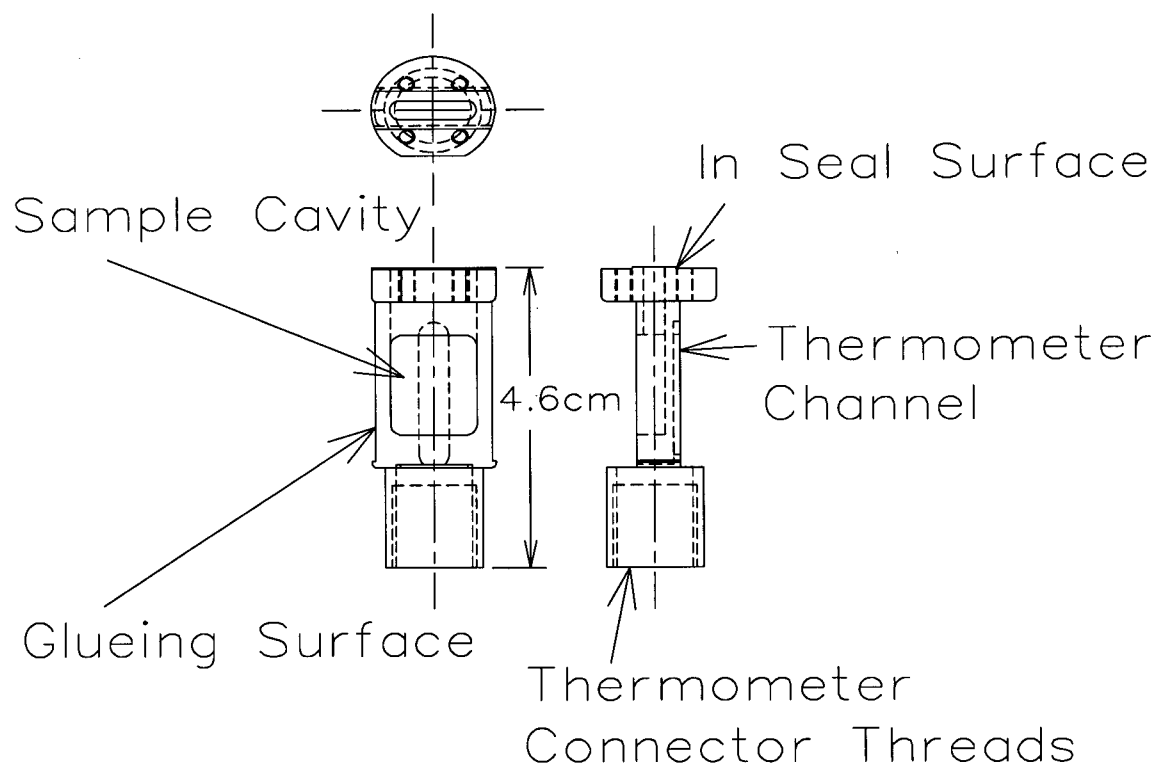
Figure B.1: A scale drawing of the (Ag) powder cell used in the dilution refridgerator. The sample is loaded via the slot in the top of the cell which is surrounded by the 4–hole pattern of threaded holes for the sealing screws. Note the relieved area for the indium seal. The seal is made with a plug (not shown) also made of 99.9% Ag.

Formulators of Canada Ltd. G–R, nominally a woodworking epoxy) is mixed and bubbles removed by pumping on it in a bell jar. Both surfaces are *lightly* epoxied with a fine brush. Excess epoxy may leak into the cavity and harden into a sharp point capable of puncturing the Kapton. Furthermore, excess epoxy may stop muons and contribute a background signal. The window is attached at one end to the back of the cell and is wrapped around, being held taught by hand and tape. The cell is then introduced into a channel shaped Al form lined with a thin sheet of neoprene rubber and clamped with a small c–clamp. The window is then left for the hardening time of the epoxy (12 hours

for G–R). The success of the gluing process can be observed through the transparent Kapton, but other tests are recommended to ensure that the window is vacuum tight. For instance, the cell can be filled with Ar or He gas and sealed using a thin rubber o–ring, and then the leak–rate measured by placing the cell in an evacuable dessicator and using a residual gas analyzer. We note that Kapton is permeable to He but not to Ar, so some calibration of the expected leak–rates is required. An epoxied window of dimensions roughly the same as shown in Fig. B.1 was tested to high (internal) pressure, and was found to burst at about 8 atm, with the Kapton and not the epoxy failing.

The low thermal conductivity of *all* materials below 1K[88] makes both thermal contact and thermometry serious concerns for any experiment at DR temperatures. The use of an exchange gas alleviates the problem of thermal contact, but the only gas with sufficient vapour pressure below 77K is He. The practical low temperature limit for any exchange gas is set by the temperature at which the saturated vapour pressure drops drastically, for ^{4}He this is about 1K and for ^{3}He it is about 0.3K.

For a powder (or even pressed powder), thermal contact via an exchange gas (as opposed to conduction) is clearly preferable. However, one must always be concerned when placing a sealed vessel into a coldfinger DR cryostat, such as this, that the vacuum seal of the sample cell may have been lost during loading or cooling and the exchange gas may have leaked away. There are several ways to test this. One method involves use of a paramagnetic thermometer such as Cerium Magnesium Nitrate (CMN). Such a method has not yet been tried, but one would simply load the CMN in the same way as a sample, and use the temperature dependence of the muon frequency[89] to reliably measure the temperature in the cell. Loss of exchange gas would manifest itself in the "bottoming out" of the CMN temperature above the minimum exchange gas temperature. This method relies on the reproducibility of the sample cell seal, but has the advantage of allowing calibration of the DR resistive thermometers with the actual temperature of an insulating

sample in the exchange gas. Another method is to compare the thermal gradients, as measured by an array of resistive thermometers, (typically RuO_2 film thermometers) along the length of the DR coldfinger between runs with the cell empty, filled both with and without the exchange gas. If the exchange gas has escaped or completely liquefied, the main thermal contact to the sample will have been broken, and the sample will provide a radiative/conductive heatload on the coldfinger. Observation of a difference in the temperature gradient caused by this heatload at some temperature would set a lower limit on the sample temperature that could be obtained reliably.